JUSTUS-LIEBIG-
UNIVERSITÄT
GIESSEN

Experimental Studies of Proton-Unbound Nuclei

via In-Flight Decay Spectroscopy

Inauguraldissertation zur Erlangung des Doktorgrades der
Naturwissenschaftlichen Fakultät der Justus-Liebig-Universität Gießen

vorgelegt von

Daria Kostyleva
geboren in Uglitsch, Russland

Fachbereich 07 - Mathematik und Informatik, Physik, Geographie

II. Physikalisches Institut Justus-Liebig-Universität Gießen

December, 2020

Erstgutachter: Prof. Dr. Christoph Scheidenberger
Zweitgutachter: Prof. Dr. Dr. h.c. Hans Geissel

Tag der Disputation: 18.12.2020

Contents

Chapter 1

Introduction

1.1 Isotopes beyond the driplines

The existence of atomic nuclei extends over a large region of proton and neutron numbers, which is displayed in the so-called chart of nuclides, where one finds the stable and radioactive nuclei. The latter are unstable with respect to α-, β- and γ-emission and fission, but they are bound regarding the nucleon emission, i.e., their individual protons and neutrons are confined by the strong nuclear force within a compact volume. This allows these so-called bound nuclei to have typical lifetimes of the order of 1 ms or longer. The border line, which separates the particle-bound isotopes of a chemical element (i.e., nuclides with identical atomic number but different mass number) from the unbound ones, is called dripline. On the neutron-rich side of the chart of nuclides there is the neutron dripline, while the proton dripline is located on the neutron-deficient side. When one adds (or removes) more and more neutrons to the isotopes of a chemical element, the neutron (or proton) separation energy becomes smaller and smaller, and the point where it becomes negative is the point where the neutron (or proton) dripline is reached. In other words, if one adds (or removes) neutrons to (or from) a bound nuclear system, the balance between neutrons and protons in the nucleus becomes more and more disturbed until the nucleon emission threshold is reached. Such an isotope at or beyond the dripline tends to emit one or several nucleons to retrieve stability with respect to nucleon emission and becomes bound again. However, the world of nuclei does not abruptly end at the driplines. The isotopes beyond the dripline exhibit individual states, too, and may have lifetimes exceeding the characteristic time of nucleon orbital motion in a nucleus, which is of the order of 10^{-22} s. These unbound states are called resonances, the term is adapted from scattering theory [1]. Resonances are usually characterized by their width Γ instead of the lifetime τ, while Γ is inverse proportional to τ[1]. Experimentally they can be studied when they have sufficiently long lifetimes of the order of picoseconds and up. Short-lived unbound nuclear systems represent a considerable difficulty with respect to their production, detection and the study of their properties. The further beyond the driplines they are, the less is known about their existence.

Today, the following questions are of key interest: where are the limits of existence of unbound nuclear systems and what comes beyond? Is there another border, maybe in analogy to the driplines, between unbound nuclear systems and the contin-

[1] According to the Heisenberg uncertainty principle, Γ is inverse proportional to τ as $\Gamma \sim \hbar/\tau$, where $\hbar$ is the reduced Planck constant.

uous spectrum, and what is, in analogy to neutron or proton separation energies, the corresponding criterion to identify this border line? It is one of the aims of this thesis to approach some answers to these questions, gain insights on the phenomenon of proton radioactivity and understand properties of some isotopes far beyond the proton dripline[2].

This thesis is devoted to studies of proton-unbound nuclei in the region of argon. Proton-unbound nuclei emit spontaneously one or several protons. They are located far from the β-stability region and in particular beyond the proton dripline. For one- ($1p$) and two-proton ($2p$) emission processes, the respective separation energies S_p and S_{2p} for the nucleus with N neutrons and Z protons are defined by:

$$S_p(N,Z) = B(N,Z) - B(N,Z-1), \tag{1.1}$$

$$S_{2p}(N,Z) = B(N,Z) - B(N,Z-2). \tag{1.2}$$

The $B(N,Z)$ is the binding energy of the nucleus with the mass $M(N,Z)$. It is defined as

$$B(N,Z) = (Zm_{\mathrm{p}} + Nm_n - M(N,Z))c^2, \tag{1.3}$$

where c is the speed of light, m_{p} and m_n are the masses of the proton and neutron, respectively.

While moving along an isotopic chain towards the neutron-deficient side, the value of S_p gradually decreases, and becomes negative at the proton dripline. Here, where proton emission is energetically possible, the proton-unbound nuclei are located. However, near the dripline the protons are still confined by the Coulomb potential and centrifugal barrier inside the nucleus and can leave it only with a certain emission probability, which depends on the energy of the state and the corresponding widths of this potential barrier. This leads in many cases to very large partial half-lives with respect to proton emission, (much) larger than the partial half-lives of alternative decay mechanisms (such as β-decay), so that it can become very difficult, sometimes practically impossible, to observe the proton-emission process experimentally. Therefore, the present studies extend far beyond the dripline. The study of such very neutron-deficient isotopes far from stability is an excellent way to examine basic nuclear properties and test theoretical concepts, e.g., the basic mean-field approach, and gain insights of the strong nuclear force. The applicability of the main nuclear structure principles in unexplored regions of the nuclear *Terra Incognita* may be tested.

The phenomenon of proton radioactivity is also an access path to nuclear binding energies and nuclear masses, as indicated by the equations above. Moreover, the investigation of very neutron-deficient isotopes allows to approach the fundamental question of the limit of existence of nuclear structure as such and the transition to amorphous nucleon matter. The Fig. 1.1 illustrates such a limit. It exhibits the sketch of a representative nuclear potential $U(r)$ in dependence of the distance r from the center of a nucleus. The shape is characteristic for a nuclear potential with Coulomb and centrifugal contributions. A discrete spectrum of bound stationary states is shown inside the potential well. Unbound states with small (positive) decay energies are still below the potential barrier. These states have lifetimes long enough to be treated in many theoretical applications as so-called stationary states (for example, $2p$-radioactive nuclei

[2]Up to now, the neutron dripline has been reached only for very light elements up to fluorine. The phenomenon of neutron radioactivity has not been firmly established yet.

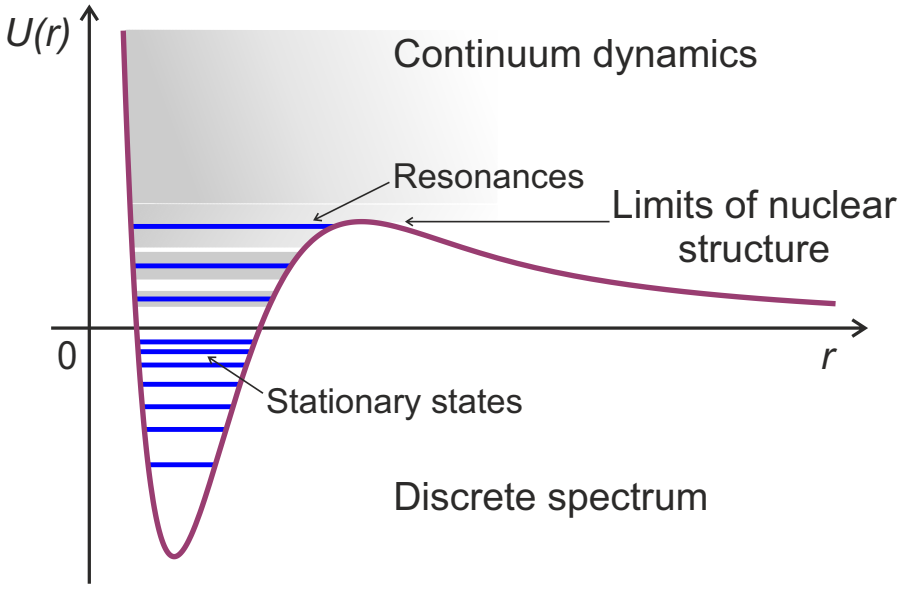

Figure 1.1: Sketch of the radial dependence of the mean nuclear potential $U(r)$. Stationary states, belonging to the discrete spectrum, are shown by solid blue lines inside the potential well. Resonant states, below the Coulomb and centrifugal barrier, are shown by blue lines surrounded by gray-shaded areas, which indicate their widths. The continuous spectrum is shown by the gray-shaded area.

^{45}Fe, ^{48}Ni and ^{54}Zn with half-lives $T_{1/2}$[3] of the order of milliseconds, see Chapter 2 for details). The resonant states, located above the top of the potential barrier, have large widths. At some point, very broad states become indistinguishable from the continuous spectrum, where a well-defined nuclear structure cannot be formed. One may assume that a certain nuclear configuration has an individual structure with at least one distinctive state when the orbiting valence protons of the system are reflected within the corresponding nuclear barrier at least once [2]. Thus, according to theoretical predictions from [2], nuclear systems with widths exceeding 3 – 5 MeV have half-lives shorter than the time needed for the formation of a nuclear state. The latter criterion is considered further on to determine the limit of existence of nuclear structure.

1.2 Experiments with exotic nuclei at FRS and Super-FRS with EXPERT

The experiments devoted to the proton-emission studies described in this thesis have been performed with the FRS fragment separator [3] of the GSI accelerator facility using a prototype detector setup of the EXPERT project [4]. On the long term, the continuation of such studies is planned at the future Super-FRS fragment separator [5], which is under construction at the GSI-FAIR accelerator facility. While the experiments are described in detail later (see Chapter 3), the physics goals of the EXPERT project and its instruments are briefly presented below.

The acronym EXPERT stands for the physics program "EXotic Particle Emission

[3] $T_{1/2} = \ln 2\ \tau$.

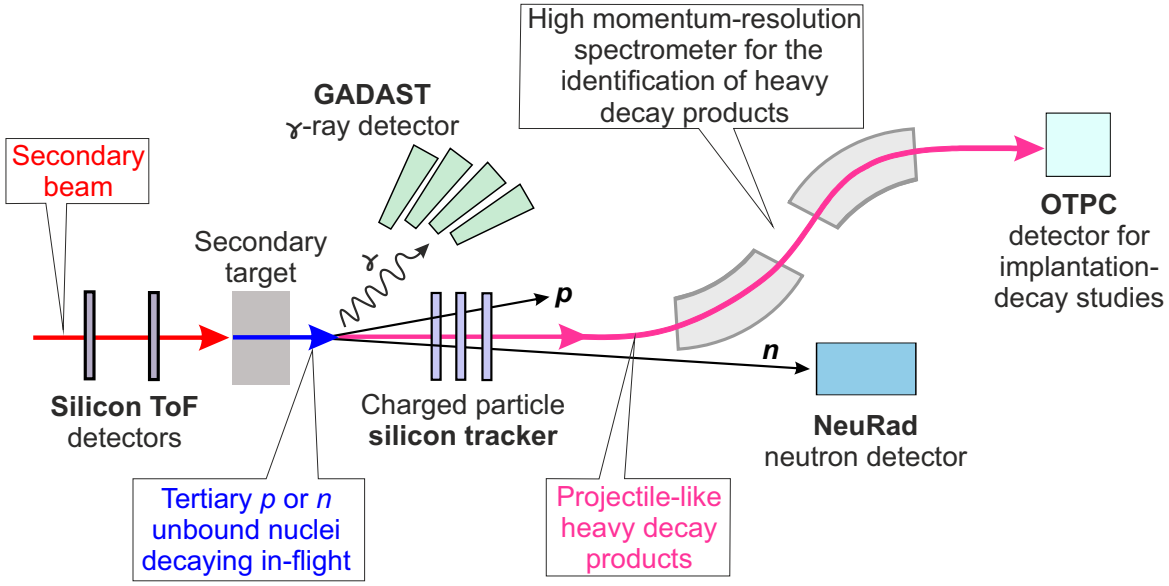

Figure 1.2: Schematic layout of the EXPERT experiment [4] at the Super-FRS superconducting fragment separator [5]. The proton or neutron unbound nuclei of interest will be produced via secondary nucleon knock-out reactions in the secondary target, which is located at the central focal plane of the main separator. The tertiary unbound nuclei will decay in-flight, producing the following final fragments: light particles (one or several p or n) and projectile-like heavy decay products. Charged decay fragments will be detected by the silicon tracker, the trajectories of neutrons will be detected by the NeuRad detector, γ de-excitation will be recorded by GADAST [7]. Projectile-like heavy decay fragments will be traced and identified by the second part of the Super-FRS main separator, which acts as a high momentum-resolution magnetic spectrometer. Implantation decay studies of the heavy decay fragments will be performed using the OTPC detector [8]. Silicon detectors in front of the secondary target will provide Time-of-Flight (ToF) information for the secondary beam identification.

and Radioactivity studied by Tracking", which is one of the physics topics addressed by the Super-FRS Experiment Collaboration [4, 6]. The experiments within the EXPERT project aim at studies of hitherto-unknown exotic nuclear systems in very remote parts of the chart of nuclides, in particular beyond the proton and neutron driplines. The collaboration focuses on processes like multiple proton emission[4] ($2p$, $4p$ etc.) and single or multiple neutron emission[5] ($1n$, $2n$, $4n$ etc.), and first so-called pilot experiments are performed with the FRS.

The EXPERT experiments will use the pre-separator and the first half of the Super-

[4]The $2p$-decay phenomenon and a brief history of $2p$ radioactivity are reviewed in Chapter 2.

[5]First theoretical estimates for the search for the so far undiscovered neutron radioactivity, which is expected for very neutron-rich nuclei, have been proposed in [9]. In the same work, the feasibility of an experimental search for long-lived true $2n$ and $4n$ emitters by using an in-flight decay tracking technique has been discussed. Soon after, an indication of $2n$-radioactivity in ^{26}O has been obtained in [10], reporting a lifetime of this nucleus in the order of ps. The subsequent theoretical interpretation, where ^{26}O is treated as a three-body system [11], has demonstrated that the reported lifetime of ^{26}O corresponds to a very small value of its decay energy of 1 keV. The measurement of such a small energy presently impossible and a challenge for future experiments. As a consequence, the concept of the so-called NeuRad detector has been proposed [12], which is part of the future EXPERT setup.

FRS main separator for the separation and identification of the incoming secondary beam (which is produced from the primary beam from SIS100 synchrotron [13] in the production target at the entrance of the pre-separator) and the second half of the main separator as a high momentum-resolution spectrometer. The schematic drawing of the EXPERT setup and the physics scenarios to be studied with it are shown in Fig. 1.2. The exotic nuclei of interest will be produced in a secondary target (these tertiary nuclei are the mother nuclei, whose (single or multiple) proton or neutron decay will be studied), which is located at the central focal plane of the main separator of the Super-FRS. When these mother nuclei decay in flight, their outgoing fragments (i.e., the projectile like heavy daughter nuclei) will be traced and identified by the magnetic spectrometer. The flight paths of the light decay products (protons or neutrons) will be tracked by corresponding highly-segmented detector arrays (see below for details), and γ-ray detectors will detect energetic radiation. All these setups are located at the central focal plane of the main separator of the Super-FRS and form the central part of the EXPERT setup; more detectors will be placed at subsequent focal planes. The major elements of the setup (in addition to the Super-FRS standard diagnostic detectors for fragment tracking and identification) are described in the following:

- **The charged-particle tracker.** It consists of several layers of silicon microstrip detectors. Its primary task is to determine the trajectories of all decay products of the mother nuclei produced in the secondary target. Details of such a tracking array and its performance during the EXPERT pilot experiment can be found in Chapter 3.
- **The Neutron Radioactivity (NeuRad) detector.** It is constructed of 10^4 scintillating fibers. The detector aims at measurement of angular correlation between nuclear-decay neutrons and the charged-particle decay products measured by the other detectors of the EXPERT setup. Details of NeuRad construction and results on the development can be found in Chapter 8.
- **Silicon Time-of-Flight detectors.** These detectors will provide both Time-of-Flight and energy-deposition information on secondary-beam and outgoing-fragment ions. More details about the developments of the silicon ToF detector can be found in Chapter 8.
- **The Optical Time-Projection Chamber (OTPC) detector.** The OTPC [8] will perform the implantation-decay measurements of ions at the final focal plane of the Super-FRS. A brief description of the implantation technique and the role of the OTPC in studies of the $2p$ radioactivity are presented in Chapter 2.
- **The GAmma-ray Detector Around a Secondary Target (GADAST).** It allows for tagging different states of the radioactive decays when the heavy fragments de-excite by emitting a γ-ray. The first experience with the GADAST detector is presented in [7].

The individual EXPERT detectors will provide correlated information on the decay products, which promises a significant synergy effect in the analysis of the obtained data.

Meanwhile, some EXPERT pilot experiments have been carried out successfully at the fragment separator FRS. The description, analysis, and results of one EXPERT pilot experiment is the primary topic of this thesis. The thesis is devoted to the study of several proton-unbound isotopes of the chemical elements argon, chlorine,

and potassium. It is structured in the following way. The present Chapter includes an introduction to the studies of exotic nuclei beyond the driplines at GSI within the EXPERT project. Chapter 2 reviews the history of spontaneous proton-emission studies, as well as the description of modern experimental approaches, including the in-flight decay technique used in the EXPERT experiments. Chapter 3 is devoted to the description of the EXPERT pilot experiment that aimed at the investigation of the $2p$-emitting ^{29}Ar and ^{31}Ar* isotopes and their decay sub-systems ^{28,30}Cl. The analysis of the data and first spectroscopy of the discovered isotopes are presented in Chapter 4. The discussion of the obtained results is provided in Chapter 5. Chapter 6 is devoted to the data analysis of $3p$ emitter ^{31}K and the corresponding spectroscopy. Possible improvements of the in-flight decay technique are introduced in Chapter 7. The recent developments of the EXPERT detectors performed in the context of the present work and the results of the laboratory work and tests with heavy-ion beams can be found in Chapter 8. Several ideas for forthcoming in-flight decay studies and intended instrumental improvements are summarized in Chapter 9.

Chapter 2

Two-proton radioactivity

2.1 The phenomenon of two-proton emission

Two-proton ($2p$) radioactivity is the process of spontaneous emission of two protons from a nucleus in its ground state. This phenomenon was predicted for light even-Z nuclei half a century ago by Zeldovich [14] and Goldansky [15], but discovered experimentally approximately only two decades ago in the ^{45}Fe isotope [16, 17] in experiments at GSI and GANIL. The $2p$-decaying nuclei are located on the neutron-deficient side of the chart of nuclides, beyond the proton dripline. By definition, $2p$ radioactivity is the simultaneous $2p$-emission mode of a nucleus (N, Z), contrary to the sequential emission of protons via a short-lived state of an intermediate nuclear subsystem $(N, Z-1)$. Such a decay is possible due to the pairing interaction between the outer-shell valence protons, and under the condition that the one-proton emission is energetically forbidden. This phenomenon has a quantum-mechanical nature. It can be seen and treated theoretically in analogy to the alpha-decay process, where the Coulomb barrier penetration leads a quantum-mechanical tunneling effect [18].

In this work, the following notations of one- and two-proton decay energies are used:

$$\begin{aligned} Q_p &= -S_p, \\ Q_{2p} &= -S_{2p}, \end{aligned} \tag{2.1}$$

where Q_p and Q_{2p} denote the energies relative to the $1p$- and $2p$-emission thresholds, respectively. Possible progressions of $2p$ emission are illustrated in Fig. 2.1. Beyond the proton dripline, both $1p$ and $2p$ decays are energetically possible, see Fig. 2.1 (a). Here, the binary decay of the (N, Z) nucleus is more favorable than the three-body decay, because the $2p$-separation threshold of the $(N, Z-2)$ system is higher, namely $Q_p > Q_{2p} > 0$. Such a scenario is typical for excited states that are populated in β-decays. If the intermediate $(N, Z-1)$ system is unbound, the so-called sequential proton emission takes place, see Fig. 2.1 (c). The energy condition here is $Q_{2p} > Q_p > 0$. In this case, the three-body problem of the $2p$ emission is reduced to the two-body one[1]. Finally, the true $2p$ decay is shown in Fig. 2.1 (b). Here, the sequential emission of protons is energetically prohibited (the state $(N, Z-1)$ is energetically higher than the state $(N, Z-2)$), thus both protons can be emitted only simultaneously. Such a scenario has to be addressed by the methods of few-body physics[2]. It should be noted

[1] Mathematical description of sequential two-proton emission is given in Section 2.4 of this Chapter.

[2] For example, the three-body model developed by Grigorenko *et. al* [19].

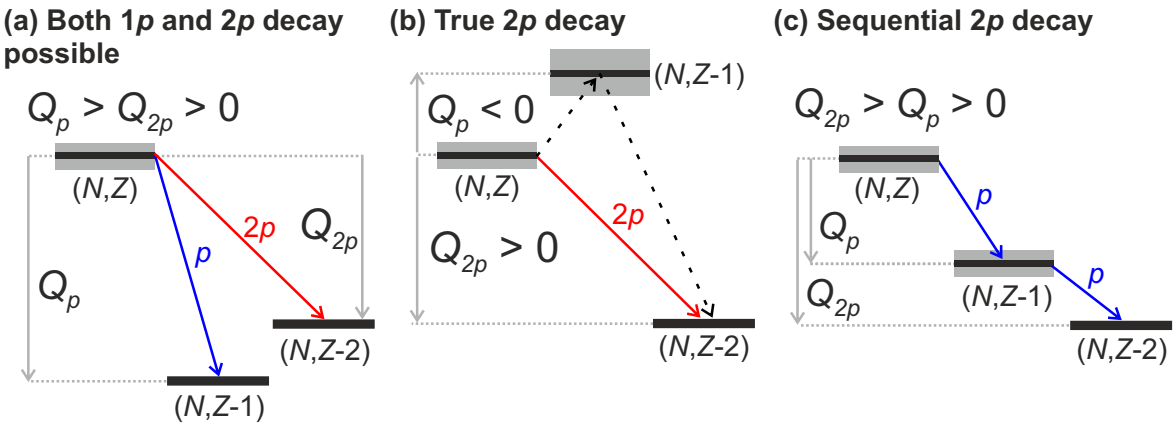

Figure 2.1: Energy levels for three different scenarios of $2p$ emission. The unbound states are indicated by gray shaded areas. Panel (a): both $1p$ and $2p$ decays are possible under the condition $Q_p > Q_{2p} > 0$. Panel (b): true $2p$ (or three-body) decay, $Q_p < 0$ and $Q_{2p} > 0$. The energetically-forbidden sequential decay channel is shown by the dashed arrows. Panel (c): sequential emission of 2 protons via a proton-unbound intermediate state, $Q_{2p} > Q_p > 0$.

that only basic scenarios of the $2p$ emission are presented in Fig 2.1. The description of special mechanisms of $2p$ emission can be found, for example, in references [19] and [20].

The evolution of proton separation energies S_p and S_{2p} for the isotopic chains of Fe and Co are presented in Fig. 2.2. The S_p and S_{2p} are taken from the Atomic Mass Evaluation (AME2016) tables [21]. The S_p of ^{45}Fe from panel (a) is predicted to be around 560 keV, and the measured S_{2p} is around -1.2 MeV. This supports the true $2p$-emission nature of the decay of this isotope. The next neutron-deficient nuclide in this chain, ^{44}Fe, is expected to emit two protons sequentially. This isotope has not yet been discovered. The predictions for the Co chain presented in panel (b) point to $1p$ emission in ^{48,49}Co decays, also it is dominating in ^{47}Co.

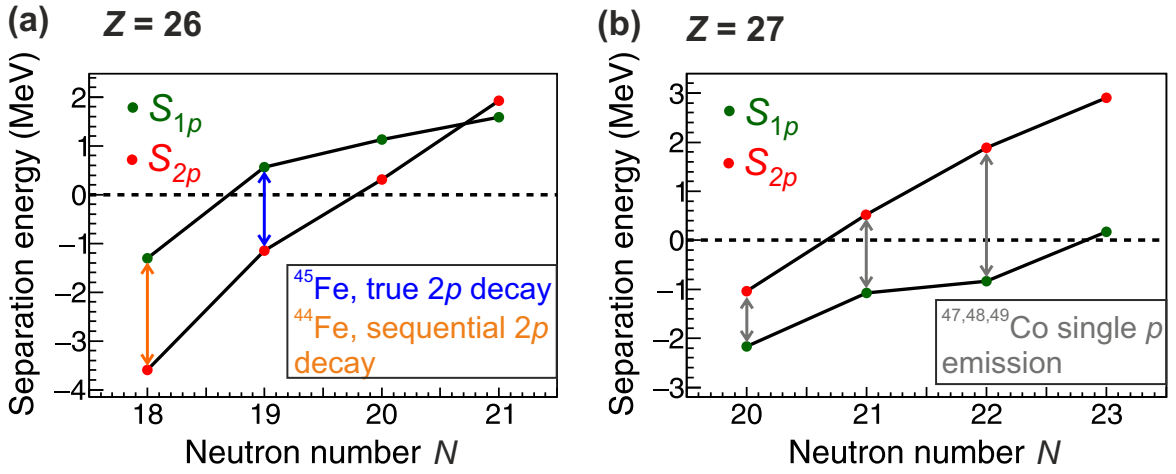

Figure 2.2: Display of the $1p$- and $2p$- separation energies $S_{p,2p}$ of iron and cobalt isotopes from the Atomic Mass Evaluation (AME2016) tables [21]. Certain types of proton emission are indicated by double-sided colored arrows, see legend.

The lifetimes of $2p$ emitters cover a broad range from the "nuclear" ones up to typical β-decay lifetimes, i.e., from 10^{-22} s up to milliseconds or even seconds. The existence of relatively long-lived p emitters can be explained by the presence of the Coulomb barrier and its confining effect on the protons [22, 23]. At the same time, the Coulomb repulsion prevents nuclei with large proton excess from being bound. Thus, the proton dripline is rather close to the line of β-stability, at least compared to the neutron dripline, where only the centrifugal barrier exists. Experimental techniques, that allow to study $2p$ emitters with different lifetimes are reviewed later in this Chapter.

2.2 Brief history of two-proton emission studies

As mentioned above, Zeldovich triggered the conceptual idea of $2p$ radioactivity, and later Goldansky suggested it in his article [15] in 1960. The work introduced the concept of true, i.e., direct $2p$ emission. According to it, "the general condition for two-proton radioactivity is that the positive binding energy of the first proton must be larger than the half-width of the emission of the second one". That is, an alternative sequential proton emission is not possible even via a tail of a broad intermediate nuclear state. In units of the decay energy and the decay width Γ this condition can be written as $Q_p < 0$, $\Gamma < Q_p$ and $Q_{2p} > 0$ for (N, Z) decaying system. It is explained and illustrated above in Fig. 2.1 (b). Goldansky showed that protons share the total decay energy $E_T = Q_{2p}$ like $E_T/2$ with the largest probability. He also noted that two protons could be treated together as one quasi-particle "diproton" with charge 2 and mass 2. For a long time, the emission of a diproton was considered to be the mechanism behind $2p$ radioactivity [24, 25]. Later, this idea appeared to be misleading. It was in contradiction with the basic quantum-mechanical uncertainty principle, and the true $2p$ decay was described by a three-body model [19].

The current knowledge on $2p$-decaying isotopes is briefly reviewed below and summarized in Table 2.1. The first attempts to reach isotopes at the proton dripline experimentally started from the region of light $2p$-unbound nuclei. The $2p$ decays of ^{6}Be [26, 27], ^{12}O [28, 29], ^{16}Ne [28, 30] were studied, see also Table 2.1. These processes could not be classified as radioactivity: the half-lives of these nuclear systems are too short because of a low Coulomb barrier: they are categorized as resonances, see Chapter 1 for definition.

One of the aims in reference [26] was to observe the diproton emission from the ^{6}Be ground state (g.s.). However, the diproton configuration could not explain the observed energy and angular correlation of the decay products, and the "democratic" decay concept arose [31]. Here, "democratic" decay means that the width of the decaying state is comparable to both outgoing protons, and no strong correlation between the decay fragments is observed. A recent high-statistics experimental study of ^{6}Be allowed for the extraction of precise three-body correlations, which were well reproduced by the three-body model of Grigorenko *et. al* [32, 33]. In this model, the decaying nuclear system is presented as an inert core and two valence protons. It is suitable for the description of proton-proton (p-p) and proton-core (p-core) correlations as well as for the prediction of lifetimes. This model has been widely used in all recent $2p$ studies. For example, the reference [32] set aside the ideas of diproton emission from ^{6}Be in favor of complex three-body dynamics.

Another search for diproton correlations was carried out for the $2p$ decay of the g.s.

Table 2.1: Overview of known $2p$ emitters. E^* denotes the excitation energy with respect to the g.s., E_T is the total decay energy with respect to the $2p$-emission threshold, Γ and $T_{1/2}$ correspond to the partial values of width and half-life to the $2p$ decay, respectively. References for experimental and theoretical studies of the isotopes are given in the corresponding columns. The values of E_T, Γ and $T_{1/2}$ are given for the most recently performed experiment.

^{A}Z	E^*(keV)	E_T(keV)	Γ(keV) or $T_{1/2}$	Experiment	Theory
^{6}Be	g.s.	1370(50)	92(6)	[26, 27]	[32, 33]
^{11}O	g.s.	∼4000	-	[34]	[35]
^{12}O	g.s.	1638(24)	< 72	[28, 29, 36]	[37]
^{16}Ne	g.s.	1466(20)	< 80	[28, 30, 38]	[37, 39, 40]
^{17}Ne	1288(50)	344	$< 1.6(3)\times10^{-4}$	[41, 42, 43]	[39, 44]
^{19}Mg	g.s.	750(50)	4.0(15) ps	[45]	[18, 39]
^{30}Ar	g.s.	2250^{+150}_{-100}	< 10 ps	[46]	[47]
^{45}Fe	g.s.	1154(16)	$1.6\ ^{+0.5}_{-0.3}$ ms	[16, 17, 48]	[47]
^{48}Ni	g.s.	1290(40)	$2.1\ ^{+1.4}_{-0.4}$ ms	[48, 49, 50]	[18]
^{54}Zn	g.s.	1280(210)	$1.59\ ^{+0.6}_{-0.35}$ ms	[51, 52]	[53]
^{67}Kr	g.s.	1690(17)	7.4(30) ms	[54]	[55]

of ^{12}O. Based on its nuclear binding energy (derived from atomic mass measurements), it was considered to be a diproton emitter [28]. The obtained opening-angle distribution between two protons in the center-of-mass system (c.m.s.) showed no evidence of diproton emission [29]. Later on, new theoretical results on ^{11}N (the subsystem of ^{12}O) triggered the re-evaluation of ^{12}O data, and the sequential $2p$ emission of this isotope was confirmed [56]. The latest experimental study of the $2p$ decay of the ^{12}O was performed utilizing invariant mass[3] method [36]. Recently, another $2p$-unbound isotope ^{11}O has been observed [34]. The obtained invariant mass spectrum was described by the newly-developed Gamov coupled-channel approach [35].

A very important of the overall understanding of the phenomenon the ^{16}Ne isotope remained poorly investigated for a long time. Based on its nuclear binding energy, it was also considered to be a diproton emitter [28]. Later, this isotope was investigated by Mukha *et al.* using the newly developed in-flight decay technique [30], see Subsection 2.6.3 of this Chapter. The obtained angular correlations between the decay products implied a genuine three-body decay mechanism of its g.s. The observables were described quantitatively by the predictions of the three-body model [39, 40] in contrast to the quasiclassical diproton model, which failed to describe the data. The most recent study of ^{16}Ne has been performed using the invariant mass technique [38]. In this work, the correlation between the momenta of the three decay products of ^{16}Ne has been measured with high resolution and statistics. This helped to reveal their dependence on the long-range nature of the Coulomb interaction. Besides, a new upper-limit on the decay width of ^{16}Ne g.s. was set, see Table 2.1.

Aside from ground-state decays, many bound nuclei possess excited states, which decay via the emission of two protons. Such states are first populated, for example, by the β-decay, and then the protons are emitted sequentially. This phenomenon of beta-delayed proton emission was observed for instance in the nuclei ^{22}Al, ^{26}P, ^{27}S,

[3]The invariant mass method applied to decay studies is reviewed in Section 2.6 of this Chapter.

^{31}Ar, ^{35}Ca, ^{39}Ti and others, see [57, 58, 59] and the big review [23]. Another possibility is the population of excited, $2p$ emitting states in nuclear reactions. For example, the $2p$ decay of the excited state of ^{14}O nucleus induced by the resonance reaction $^{13}\mathrm{N} + p$ was studied in [60]. The sequential decay pattern was observed in the data. The ^{19}Na excited states, populated via the inelastic scattering reaction of ^{18}Ne on a H-target, were also found to decay via sequential emission of two protons [61].

A promising candidate for $2p$ decay is the first excited state $3/2^-$ in ^{17}Ne. Experimental attempts to study this state were made several times [41, 42]. However, only an upper boundary on its width was established [43]. This state is expected to be a true $2p$ emitter, and it is interesting from the astrophysical point of view [62]. Moreover, this state might be a candidate to possess the two-proton halo [63, 64]. Theoretical studies of this isotope contradict each other [39, 44]. However, progress in the three-body calculations was made recently [65]. Another interesting case of $2p$ radioactivity from the high-lying 21^+ isomer in ^{94}Ag was discovered by Mukha *et al.* [66]. The evidence for true $2p$ decay of this isomer was found based on the measured p-p correlation. A very high $2p$ decay rate was explained by the large deformation of this nucleus. The discovery caused a number of discussions [67, 68, 69, 70], and further investigation of this case is required.

2.3 Discovery of two-proton radioactivity

After more than 40 years of research, finally the first true g.s. $2p$ emitter was discovered in year 2002 in the decay of ^{45}Fe [16, 17], and since then, many new theoretical and experimental studies of this phenomenon have progressed. The discovery was simultaneously performed by Polish and French groups at the fragment-separators FRS of GSI and LISE of GANIL, respectively. In both cases, the ^{45}Fe ions were produced in fragmentation reactions of a ^{58}Ni beam, separated in-flight and identified, and implanted into a silicon detector array. Several decay signals (decay time and energy) of ^{45}Fe ions have been recorded. In the GSI experiment [16], four $2p$ emission events were found. The total decay energy of ^{45}Fe was measured, and its half-life was estimated, see Table 2.1. The results are in agreement with the data obtained at GANIL a few days later [17]. A subsequent, similar experiment at GANIL collected information on ^{45}Fe decays with larger statistics [48], where the previously obtained decay energy and half-live were confirmed.

The direct observation of $2p$ radioactivity together with the study of the p-p correlation became possible with the use of gaseous time-projection chambers (TPC). These detectors allow for recording projections of the proton tracks on the anode plane of the TPC and thus confirmed the $2p$ emission of ^{45}Fe decay [71]. Shortly after, a novel optical TPC detector (OTPC) was utilized to obtain photographic images of the individual $2p$ decay events of ^{45}Fe [72]. The photographs of each proton track in the gas allowed for a complete kinematic reconstruction of the decay events. The measured distributions of p-p correlation [73] showed good agreement with the predictions of the three-body model [53, 74].

Shortly after the ground-breaking discoveries, several other true $2p$ emitters were found. For instance, one $2p$-decay event from the ^{48}Ni g.s. was indirectly observed in an implantation experiment at GANIL [48]. Shortly afterwards, direct and unambiguous evidence for the $2p$ radioactivity of this isotope was provided by the OTPC detector [49, 50]. Another $2p$-emitting isotope found by the GANIL group is ^{54}Zn [51], and the

spatial and energetic correlation of the two emitted protons was directly studied using the OTPC detector technique [52]. Finally, the fourth $2p$ g.s. emitter ^{67}Kr with a half-life of the order of a few milliseconds was observed by the French group at the fragment separator BigRIPS in RIKEN [54].

An original approach for studies of $2p$ decay, complementary to the implantation methods in gases and solids and ideally suited for the in-flight study of very short-lived $2p$ emitters (half-lives of the order of ps – ns), was developed by Mukha *et al.* [75]. The pioneering work applied to the search of two-proton radioactivity of ^{19}Mg is published in [45] and briefly described in Subsection 2.6.3 of this Chapter. The in-flight decay technique is based on the precise reconstruction of all decay-product trajectories using silicon microstrip detectors. The incoming secondary beam (produced in the primary production target and separated in-flight with the first two dipole stages of the FRS) underwent a nuclear reaction in a secondary target, which was located at the central focal plane and in which the nuclei of interest (here: ^{19}Mg) were produced. They

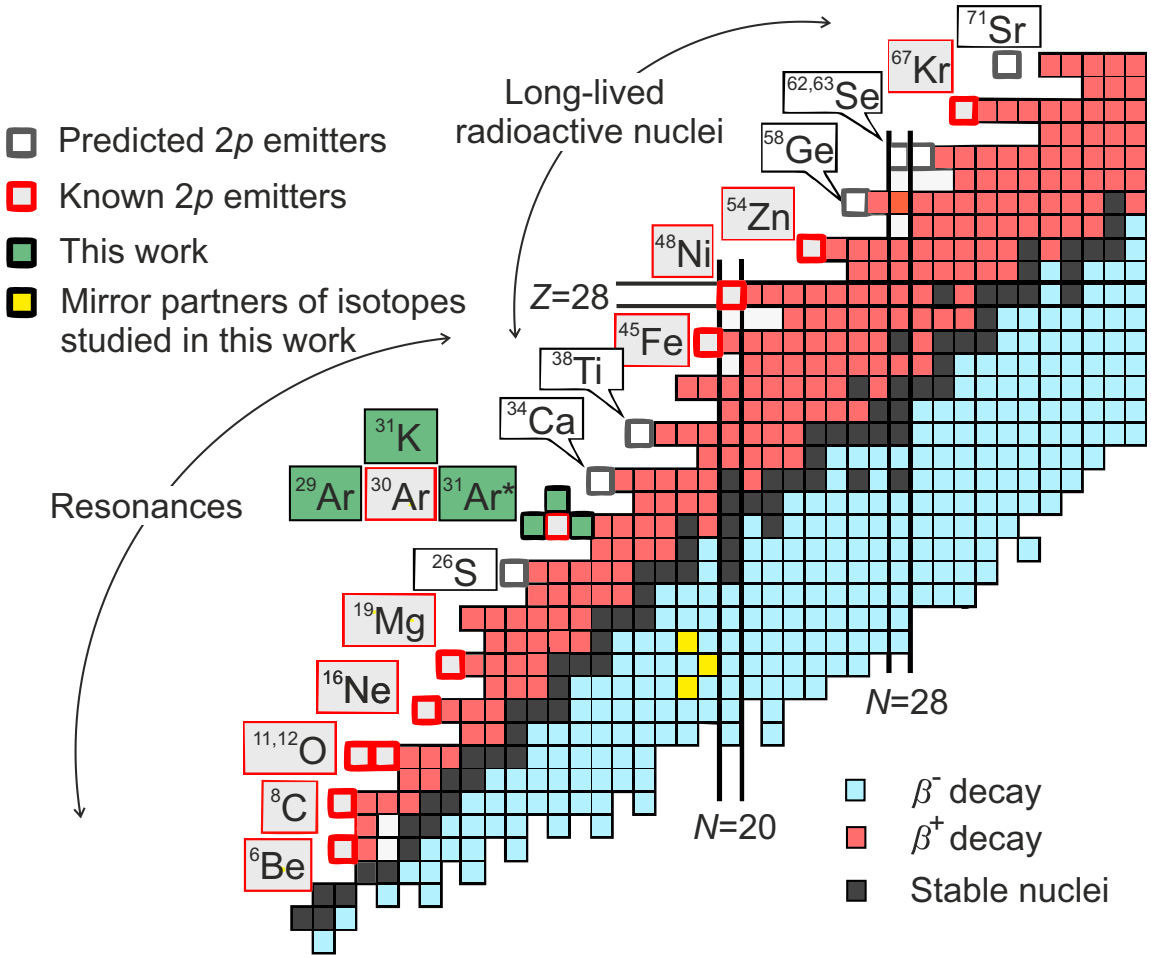

Figure 2.3: View of the lower part of the chart of nuclides with the presently known $2p$-radioactive nuclei. The regions of short- (half-lives of ps and below) and long-lived (μs-ms half-lives and up) $2p$-decaying nuclei are depicted by embracing arcs and isotope boxes. The nuclei of interest studied in this thesis, namely the $2p$-emitting Ar isotopes (^{29}Ar, excited states of ^{31}Ar) and the $3p$ emitter ^{31}K, are highlighted in green, their isobaric mirror partners (^{29}Na, ^{31}Al and ^{31}Mg, respectively) are shown in yellow. The Figure is based on the contribution to the PROCON-2019 conference [76].

decayed in-flight, still inside or shortly behind the target, and their decay products were tracked using the silicon microstrip detectors. The heavy decay products were identified with the last two dipole stages of the FRS, where also their momentum was measured. The angular correlation between the $2p$-decay products of ^{19}Mg was measured and first spectroscopy of this isotope was accomplished [45]. The measured half-life and decay energy matched the predictions of the tree-body model [39]. In conclusion, the direct mechanism of $2p$ radioactivity of the ^{19}Mg g.s. was confirmed. Also, several $2p$-decaying excited states of ^{19}Mg were discovered in the data analysis [77].

This first in-flight decay experiment and the corresponding theory developments laid the basis for the EXPERT project at the Super-FRS, see Chapter 1. Within an EXPERT pilot experiment with the FRS, the new $2p$-emitting isotopes ^{29,30}Ar, ^{31}K were discovered [46, 78, 79]. The detailed description of the pilot experiment, the data analysis and nuclear structure results of ^{29}Ar and ^{31}Ar* can be found in Chapters 3, 4 and 5 of this thesis, respectively. The most exotic case, the three-proton emitter ^{31}K, is discussed in Chapter 6.

Finally, one more proton emitter, ^{8}C, should be mentioned. This isotope was considered a candidate to decay via the simultaneous emission of four protons. However, it was shown in [80], that this nucleus undergoes a sequence of two true $2p$ decays via the g.s. of ^{6}Be.

The present status of the $2p$-emission "landscape" is sumarized in Fig. 2.3. The Figure shows the discussed $2p$ emitters and those nuclides, which are predicted to be $2p$-radioactive according to the above-mentioned theoretical models (for example, the three-body model). The Figure shows also those nuclides, which are subject of experimental study of the present thesis, including one case of the three-proton emitter (^{31}K).

2.4 Kinematics of sequential two-proton decay

Apart from the direct three-body decay, $2p$ emission can proceed sequentially. This process is significantly easier to describe mathematically because the three-body problem is reduced to two sequential two-body processes. In the following, a relativistic description of a general two-body decay is presented. To simplify the notation, the signs denoting vectors are omitted and all c.m.s. components are denoted by asterisks throughout this Section.

The two-body decay of a fast moving mother nucleus with mass M and four-momentum P is considered. The decay results in two products with masses and four-momenta m_1, P_1 and m_2, P_2, respectively. In the rest-frame of the mother nucleus (or c.m.s. in this case) its four-momentum is $P^* = (Mc, 0, 0, 0)$. The four-momenta of the decay products are $P_1^* = (E_1^*/c, p_1^*)$ and $P_2^* = (E_2^*/c, p_2^*)$, respectively, where $p_{1,2}^*$ are the three-momentum vectors. The momentum conservation law yields

$$P^* = P_1^* + P_2^*, \tag{2.2}$$

and in the c.m.s. $p_1^* + p_2^* = 0$ so that $p_1^* = -p_2^*$. The energy conservation law yields

$$E^* = E_1^* + E_2^*, \tag{2.3}$$

or, when considering the general energy-momentum relation $E^2 = m^2c^4 + p^2c^2$, Eq. 2.3 can be rewritten to

$$Mc^2 = \sqrt{m_1^2c^4 + p_1^{*2}c^2} + \sqrt{m_2^2c^4 + p_1^{*2}c^2}, \tag{2.4}$$

where p_1^* is the momentum of a decay product in the c.m.s. The derived magnitude of p_1^* is

$$p_1^* = \frac{c}{2M}\sqrt{(M+m_1-m_2)(M-m_1+m_2)(M+m_1+m_2)(M-m_1-m_2)}, \quad (2.5)$$

where one of the factors under the square root is the decay energy of the mother nucleus $Q = Mc^2 - m_1c^2 - m_2c^2$. Eq. 2.5 implies that the decay-product momenta in the c.m.s. depend only on the masses of the participating particles. The same conclusion can be drawn for the energies of the decay products. Using the energy-conservation law from Eqs. 2.3 and 2.4, the expressions for the energies of two decay products can be written as

$$\begin{gathered} E_1^{*2} = m_1^2c^4 + p_1^{*2}c^2 \\ = \frac{4M^2m_1^2c^4 + (M+m_1-m_2)(M-m_1+m_2)(M+m_1+m_2)(M-m_1-m_2)c^4}{4M^2}, \\ \\ E_2^{*2} = m_2^2c^4 + p_1^{*2}c^2 \\ = \frac{4M^2m_2^2c^4 + (M+m_1-m_2)(M-m_1+m_2)(M+m_1+m_2)(M-m_1-m_2)c^4}{4M^2}. \end{gathered} \quad (2.6)$$

The right sides of Eqs. 2.6 can be simplified, so that the energies of the decay products in the c.m.s. depend only on the masses of the particles

$$\begin{aligned} E_1^* &= \frac{c^2}{2M}(M^2 + m_1^2 - m_2^2), \\ E_2^* &= \frac{c^2}{2M}(M^2 + m_2^2 - m_1^2). \end{aligned} \quad (2.7)$$

One way to convert from the c.m.s. to the laboratory frame is to perform Lorentz transformations. Then, the longitudinal momentum components and the energy of decay product 1 (for decay product 2 the index changes accordingly) are transformed as:

$$\begin{aligned} p_x &= p_x^*, \\ p_y &= p_y^*, \\ p_z &= p_z^* + \gamma\beta\left(\frac{\gamma\beta p_z^*}{\gamma+1} + \frac{E_1^*}{c}\right), \\ E_1 &= \gamma(E_1^* + \beta p_z^* c), \end{aligned} \quad (2.8)$$

where $p_{x,y,z}$ are the momentum components of the decay product 1 in the laboratory frame, and E_1 is its energy. The velocity relative to the speed of light β and the Lorentz factor γ are related to the total energy E and momentum p of the mother nucleus as

$$\beta = \frac{pc}{E}, \gamma = \frac{E}{Mc^2}. \quad (2.9)$$

In the laboratory frame the mother nucleus has a four-momentum $P = (E/c, p)$. It moves along the z-axis in the direction of p. The four-momentum of a decay product P_1 depends on the decay angle, which is the angle between its momentum direction and the z-axis. A scalar product of the four-momentum vectors, which is a Lorentz

invariant in all reference frames, can be used to derive this angle:

$$\begin{aligned}(P \cdot P_1) &= EE_1 - p \cdot p_1 \\ &= \frac{1}{c^2} EE_1 - pp_1 \cos\theta_1 = ME_1^*,\end{aligned} \tag{2.10}$$

where E and p are the known energy and momentum components of the mother nucleus and θ_1 is the decay angle of the decay product 1. Squaring Eq. 2.10 and collecting the energy components in the laboratory frame on one side gives the following quadratic equation

$$\frac{1}{c^4} E^2(p_1^2c^2 + m_1^2c^4) = M^2E_1^{*2} + 2pp_1ME_1^* \cos\theta_1 + p^2p_1^2 \cos^2\theta_1. \tag{2.11}$$

It has two solutions regarding the magnitude of p_1:

$$p_1 = \frac{ME_1^* p \cos\theta_1 \pm ER^2}{E^2/c^2 - p^2 \cos^2\theta_1}, \tag{2.12}$$

where $R^2 = \sqrt{M^2p_1^{*2} - m_1^2p^2 \sin^2\theta_1}$. The energy E_1 can also be obtained by solving Eq. 2.11 accordingly:

$$E_1 = \frac{ME_1^* E \pm c^2 p \cos\theta_1 R^2}{E^2/c^2 - p^2 \cos^2\theta_1}. \tag{2.13}$$

The most interesting part of both Eqs. 2.12 and 2.13 is the quantity R^2, because the radicand must be positive and thus imposes constraints on the angle θ_1, so that both the momentum of the decay product p_1 from Eq. 2.12 and its energy E_1 from Eq. 2.13 have a real value. This leads to the following condition:

$$\sin\theta_1 \leq \frac{Mp_1^*}{m_1 p} \tag{2.14}$$

If the value Mp_1^*/m_1p is larger than one, the condition from Eq. 2.14 does not restrict the decay angle θ_1 (all angles from 0 to π are possible). This is true when the mother nucleus is at rest. On the contrary, when the mother nucleus is formed in a high-energy nuclear reaction, its laboratory momentum p is significantly larger than the c.m.s. momentum p_1^*. Then the condition is $Mp_1^*/m_1p < 1$, and the maximum possible decay angle θ_1 can be found like

$$\sin\theta_1(\text{max}) = \frac{Mp_1^*}{m_1 p}. \tag{2.15}$$

The latter Eq. has an important impact on proton-emission experiments, in particular for in-flight decay studies, see Subsection 2.6.3 of this Chapter. As mentioned at the begin, sequential proton emission can be considered as two subsequent single-proton emissions with two-body kinematics in each case. Thus, $1p$ emission yields two products: a proton and a heavy ion (HI) with masses m_p and m_{HI}, respectively. In the general case, $m_p \ll m_{\text{HI}}$. Decay angles are inverse-proportional to the masses of the emitted particles, thus $\theta_p \gg \theta_{\text{HI}}$. As a result, the heavy ion trajectory has a negligible angular deviation from its original flight direction, so that $\theta_p \sim \theta_{p-\text{HI}}$. In other words, the value of the proton decay angle can be considered to be approximately the same as

the relative angle[4] between the trajectories of both decay products. Considering the above-mentioned arguments and using Eqs. 2.15 and 2.5, the maximum value of the relative angle between heavy ion and proton trajectories can be obtained

$$\sin\theta_{p-\mathrm{HI}}(\mathrm{max}) = \frac{c}{2m_p}\sqrt{\frac{(M+m_p-m_{\mathrm{HI}})(M-m_p+m_{\mathrm{HI}})(M+m_p+m_{\mathrm{HI}})}{T(T+2Mc^2)}}\sqrt{Q}, \tag{2.16}$$

where T is the kinetic energy of the mother nucleus from the general energy-momentum relation $p = \frac{1}{c}\sqrt{T(T+2Mc^2)}$. Equation 2.16 shows, that the maximum value of the relative angle $\theta_{p-\mathrm{HI}}$ is proportional to the square root of the decay energy Q.

2.5 Kinematic focusing effect

Important consequences of relativistic kinematics are observed in angular distributions of decay products in the laboratory frame. Firstly, all the particles are emitted in a narrow cone in forward direction close to the trajectory of the incoming particle. Secondly, in the laboratory frame a particle has a highest probability to be found under the maximum decay angle $\theta(\mathrm{max})$, which results in a narrow peak near this angle. The resulting peak in the angular distribution can be used to evaluate the decay energy Q, see Eq. 2.16. This feature of the decay kinematics is exploited in the in-flight decay tracking technique, which is described in Subsection 2.6.3 of this Chapter. An angular distribution for products of the two-body decay of a high-energy mother nucleus and the consequential kinematic focusing effect are derived below.

Let us first assume that the decay is non-isotropic and the angles of the decay product 1 in the rest frame of the mother nucleus θ_1^* are distributed according to the known function $\eta_1^* = \cos\theta_1^*$ like

$$W(\eta_1^*) = f(\eta_1^*), \tag{2.17}$$

where $W(\eta_1^*)$ is an angular distribution of the decay product in the rest frame. All the azimuthal angles are considered to be distributed isotropically. Then using the Lorentz transformation from Eq. 2.8, the energy of the particle 1 in the laboratory frame can be determined as

$$E_1 = \frac{E}{Mc^2}E_1^* + \frac{p}{M}p_1^*\eta_1^* \tag{2.18}$$

considering that this particle is emitted under the angle θ_1^* in c.m.s.. An angular distribution in the lab frame can be written as

$$W(\eta_1) = \frac{dN}{d\eta_1}, \tag{2.19}$$

where dN is the number of particles per interval $d\eta_1$, which is a cosine function of the decay angle θ. To facilitate the derivation of the angular distribution $W(\eta_1)$ or the $dN/d\eta_1$, the latter can be re-written as

$$\frac{dN}{d\eta_1} = \frac{dN}{d\eta_1^*}\frac{d\eta_1^*}{dE_1}\frac{dE_1}{d\eta_1}, \tag{2.20}$$

[4]The angle between trajectories of decay products is referred as relative angle throughout the text, as well as in publications concerning this topic, e.g. [79].

where the three components are derived separately.

The first component $dN/d\eta_1^*$ is the function $f(\eta_1^*)$. It can be presented also as a function of η_1. First, η_1^* is derived from Eq. 2.18 as a function of E_1:

$$\begin{aligned}\eta_1^* &= -\frac{EE_1^*}{pp_1^*c^2} + \frac{M}{pp_1^*}E_1 \\ &= a + bE_1,\end{aligned} \tag{2.21}$$

where the coefficient $a = -EE_1^*/pp_1^*c^2$ and $b = M/pp_1^*$. From Eq. 2.13 it is known, that in turn E_1 is a function of η_1. Thus,

$$\eta_1^* = a + bE_1(\eta_1). \tag{2.22}$$

The second component $d\eta_1^*/dE_1$ can be derived from Eq. 2.21. It is the constant value b:

$$\frac{d\eta_1^*}{dE_1} = \frac{M}{pp_1^*}. \tag{2.23}$$

The third component $dE_1/d\eta_1$ is found from Eq. 2.10 by taking the derivative over η_1

$$\frac{E}{c^2}\frac{dE_1}{d\eta_1} - p\frac{dp_1}{d\eta_1}\eta_1 - pp_1 = 0. \tag{2.24}$$

From the basic relativistic formula $E_1^2 - p_1^2c^2 = m_1^2c^4$ one can find that $dp_1 = (E_1/p_1c^2)dE_1$ and put this in Eq. 2.24

$$\frac{E}{c^2}\frac{dE_1}{d\eta_1} - \frac{p}{c^2}\frac{E_1}{p_1}\eta_1\frac{dE_1}{d\eta_1} - pp_1 = 0. \tag{2.25}$$

Solving the last Eq. one gets

$$\frac{dE_1}{d\eta_1} = \frac{pp_1^2c^2}{Ep_1 - pE_1\eta_1}, \tag{2.26}$$

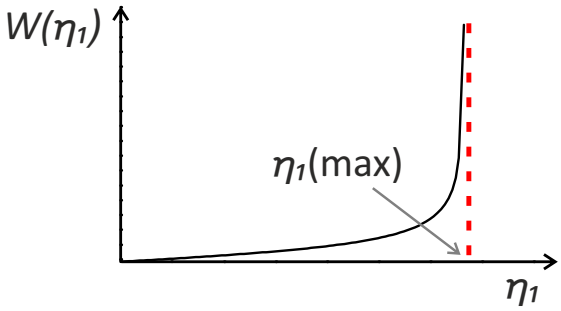

Figure 2.4: Schematic illustration of the angular distribution $W(\eta_1)$ of two-body decay products in the laboratory frame. The distribution exhibits a sharp peak close to the maximum possible angle of η_1.

where the denominator can be simplified to

$$Ep_1 - pE_1\eta_1 = R^2 \tag{2.27}$$

using p_1 and E_1 from Eqs. 2.12 and 2.13. Finally, every component for the angular distribution is derived. Thus, by plugging Eqs. 2.22, 2.23 and 2.26 into the main Eq. 2.20 one obtains

$$W(\eta_1) = f(a + bE_1(\eta_1))b\frac{pp_1^2c^2}{R^2}. \tag{2.28}$$

This is the distribution of angles between the decay products, derived for the general case. In the case of an isotropic decay in the c.m.s., the distribution is flat as a function of η_1^*. One writes $f(\eta_1^*) = 1/2$, where the averaging is carried out over the interval -1 $\leq$ η_1^* $\leq$ 1. Then the angular distribution from Eq. 2.28 is transformed to

$$\begin{aligned}W(\eta_1) &= \frac{1}{2}b\frac{pp_1^2c^2}{R^2} \\ &= \frac{1}{2}b\frac{pc^2}{R^2}\frac{M^2E_1^{*2}p^2\eta_1^2 + E^2R^4}{(E^2 - p^2\eta_1^2)^2}.\end{aligned} \tag{2.29}$$

The shape of the angular distribution from Eq. 2.29 is shown in Fig. 2.4. The most pronounced feature of this distribution is its divergence to infinity when approaching the maximum possible angle. This is mainly due to R^2 variable. It equals zero when the decay angle reaches its maximum value, see Eq. 2.15. In practice, however, the number of particles emitted under this angle cannot be infinite.

For the case of $1p$ emission a cross-check of the angular distribution in the laboratory frame has been performed using a Monte-Carlo simulation, see Fig. 7.2 (b) in Chapter 7. The resulting angular distribution has a shape similar to the one in Fig. 2.4 when using the derived laboratory angles and energies in the simulation code. More details on the kinematics of nuclear reactions can be found in various textbooks, e.g. see [81, 82].

2.6 Experimental techniques for studying two-proton radioactivity

With the mathematical support at hand, the different experimental techniques will be reviewed in this Section. As outlined in Section 2.2, various two-proton radioactivity investigations have progressed in recent years. Several $2p$ emitters have been observed experimentally, and there is a number of $2p$ precursors, which have been theoretically predicted and are expected to be discovered in the near future. The lifetimes of $2p$-unbound nuclei cover a broad range (from e.g. ps to s), which sets certain constraints on their experimental study.

2.6.1 Invariant mass method

Very short-lived proton-unbound nuclear systems can be studied by the means of the invariant mass method. It is suitable for nuclei with lifetimes of less than ~ 1 ps. A number of $2p$-unbound nuclei (or resonances) suitable for this method can be seen on the chart of nuclides in Fig. 2.3.

The basic idea of the invariant mass method is the measurement of the momenta and energies of all decay products. This information is used to reconstruct the mass of the mother nucleus in the rest frame, which is an invariant quantity. It is given by the general relativistic energy-momentum relation

$$M_{inv}c^2 = \sqrt{\left(\sum_i E_i\right)^2 - \left(\sum_i \vec{p}_i c\right)^2}, \tag{2.30}$$

where E_i and $\vec{p}_i$ are the total energy and momentum of each decay fragment i. Then, the total kinetic energy released in the decay is estimated like $E_T = (M_{inv} - \sum_i M_i)c^2$, where M_i are the known masses of all decay products.

From the technical point of view, $\Delta E - E$ detectors (ΔE is the energy deposit and E is the total kinetic energy of a particle) can be utilized for such measurements. An application of this method, for example to the studies of ^{6}Be and ^{11,12}O $2p$ emitters, can be found in references [31] and [29, 34, 83], respectively. A variation of the invariant mass method is the missing mass technique, which is employed to measure the momenta and energy components of all decay products but one. Details of this method applied to the decay of ^{17}Ne* nucleus can be found in [43].

One of the drawbacks of the invariant mass method comes from the necessity of full momentum measurement and the fact that both transverse and longitudinal components must be measured with high precision. The uncertainty of the decay energy determination receives large contributions from the transverse momentum component. Also, the method should include the contributions from γ-rays, which may be emitted in the decay process, for example, in a proton decay to a particle-bound excited state. Without additional γ-detection in the experiment, ambiguities in decay energy determination can arise.

2.6.2 Implantation method

The method is based on the implantation of the radioactive nucleus into the volume of a detector. The stopped ions decay inside, and the lifetime together with the decay energy can be measured by registering the decay products. The method is limited to studies of rather long-lived $2p$-unbound nuclei. It works in the range of lifetimes limited by the flight-time in separators e.g. 0.1 μs and up. The $2p$-radioactivity phenomenon was discovered using the implantation decay technique, see the articles devoted to the first observed true $2p$ emitter ^{45}Fe [16, 17]. The lifetime of ^{45}Fe obtained in those experiments is within the range of 3 – 6 ms.

In the first experiments of this type, ions were implanted into a stack of silicon detectors. This allowed for the total decay energy measurement. However, no momentum correlations could be obtained, because protons could not be observed individually. This problem was solved with the development and use of specialized TPC detectors. The main idea is that such a gaseous ionization chamber can record tracks of charged particles, allowing their reconstruction in three dimensions. Such a detector rendered the direct evidence for the two protons emitted by the ^{45}Fe [71]. Another design of the TPC detector included an optical readout of the light, which is emitted in the final stage of charge amplification. As a result, an "optical" OTPC detector with light collection by CCD camera and a photomultiplier was developed [8]. Application of the OTPC to studies of $2p$ emitters yielded spectacular results, providing the detailed proton-proton correlation information on ^{45}Fe [73] and ^{48}Ni [49]. Implantation into TPC and OTPC detectors has also extensively been used in studies of β-delayed proton emission, see Section 2.2 for references.

2.6.3 In-flight decay technique

A novel method was developed with the in-flight decay technique with the goal to study proton emitters with lifetimes in the ps–ns range [75, 84]. The key component of this method is the recording of tracks of all decay fragments. The latter allows for the reconstruction of the decay vertices of $2p$- (and $1p$-) emitters. Besides, nuclear-structure information of these short-lived proton-unbound isotopes can be obtained without measuring their kinetic energies but using the trajectories of all decay products only. It will be outlined in the following.

In order to illustrate how nuclear-structure information can be obtained from the angular correlations between the decay products, one may consider three different mechanisms of $2p$ emission; they are shown in the upper part of Fig. 2.5. The lower panels of the Fig. 2.5 present the corresponding transverse momentum correlation plots $k_{p1-\mathrm{HI}} - k_{p2-\mathrm{HI}}$. Panel (a) shows the energy scheme of direct a $2p$ decay of a (N, Z)

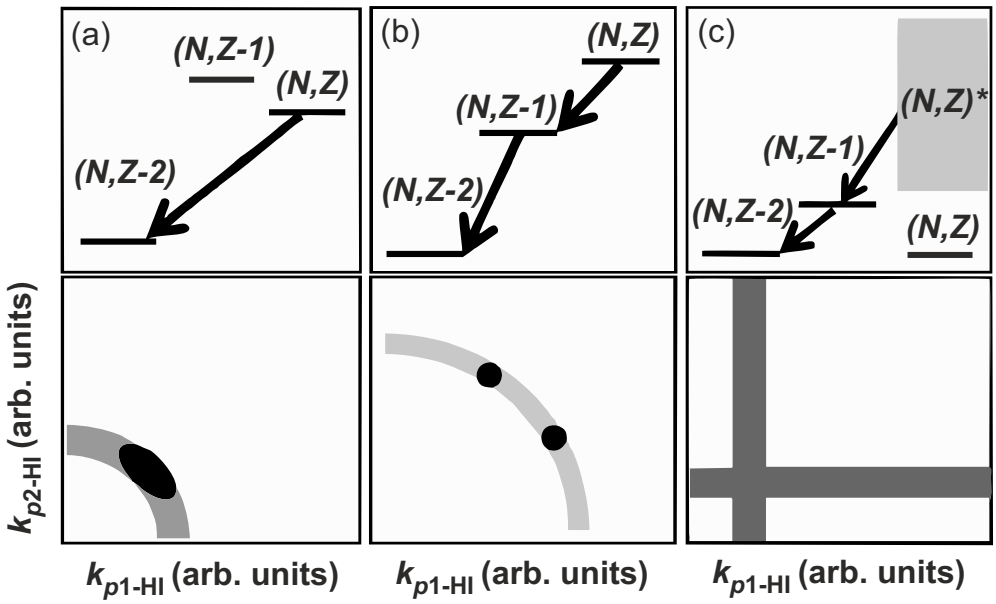

Figure 2.5: Schematic view of three $2p$-decay scenarios (upper panel) and the corresponding transverse momentum correlations $k_{p1-\mathrm{HI}} - k_{p2-\mathrm{HI}}$ (lower panel). Panel (a): direct $2p$ emission from a nucleus (N, Z). Panel (b): sequential emission of protons via an $(N, Z-1)$ intermediate state. Panel (c): deexcitation of broad continuum states of a nucleus (N, Z) via narrow intermediate state $(N, Z-1)$. The Figure is taken from [79] in modified form.

nucleus, see the detailed explanation of the process in Section 2.1. The sequential emission of protons is energetically forbidden in this case. The transverse momentum correlation plot exhibits the shape of an arc, indicated by gray color in the lower panel (a). Its radius corresponds to the Q_{2p} value, with most of the counts lying in the broad bump indicated by the black spot: because both emitted protons share the $2p$-decay energy Q_{2p} preferably equally, their spectra are broad and centered around the value of $Q_{2p}/2$. Panel (b) represents the sequential emission of protons, which proceeds through an intermediate state in $(N, Z-1)$. In this case, each proton has a well-defined, fix energy, which yields two peaks, which are indicated by the two black spots in the momentum correlation plot. It should be noted that the protons $p1$ and $p2$ are indistinguishable in all cases. Thus all the momentum correlation plots in the lower panel of Fig. 2.5 are symmetric with respect to the 45° diagonal line. The third panel (c) illustrates the case of $2p$ emission from the continuum, i.e., from broad excited nuclear states $(N, Z)^*$. The emission happens sequentially, too, via a low-lying $(N, Z-1)$ intermediate state. This leads to narrow band distributions, which are shown by dark gray color in the momentum correlation plot in the lower panel of Fig. 2.5 (c).

As mentioned above, only the trajectories of decay products are measured in the present in-flight decay experiments. The detection setup (see the detailed description of the experiment in Chapter 3) is placed directly behind the secondary target. From the two-body decay kinematics it is known that there is a maximum possible decay angle $\theta_{p-\mathrm{HI}}(\mathrm{max})$ which is proportional to the decay energy Q, see Eqs. 2.15 and 2.16. A kinematic focusing effect "forces" the particles to be emitted in a narrow cone around the $\theta_{p-\mathrm{HI}}(\mathrm{max})$, thus creating a peak in the angular distribution, see the corresponding Eq. of Section 2.5 and Fig. 2.4. These effects are illustrated in Fig. 2.6 for the case of

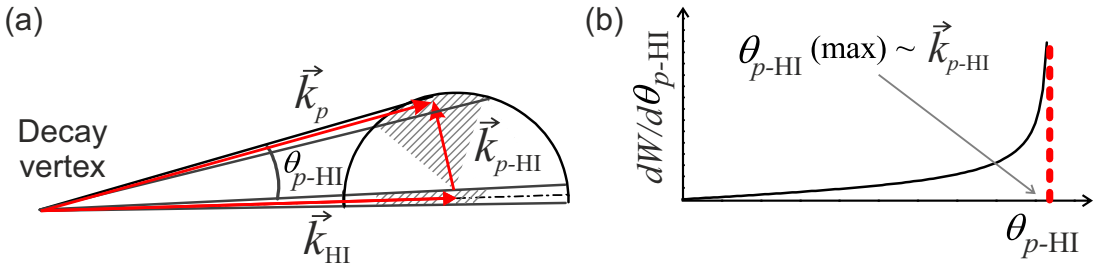

Figure 2.6: Illustration of the correspondence between transverse momentum $\vec{k}_{p-\text{HI}}$ and the maximum-possible relative angle between decay products $\theta_{p-\text{HI}}(\text{max})$ in laboratory system. Panel (a): illustration of the kinematics of an isotropic, mono-energetic single-proton emission from a swiftly moving mother nucleus. The longitudinal momenta of proton and heavy ion are labeled $\vec{k}_p$ and $\vec{k}_{\text{HI}}$, respectively. The momentum vectors are shown by red arrows. The kinematic enhancement in the laboratory frame, where $\vec{k}_{p-\text{HI}}$ has a maximum value, is shown by the dashed area. Panel (b): corresponding angular distribution $dW/d\theta_{p-\text{HI}}$ exhibiting a peak close to $\theta_{p-\text{HI}}(\text{max})$, which is directly related to the proton-decay energy Q.

$1p$ emission. Panel (a) of Fig. 2.6 shows the single proton emission from a high-energy mother nucleus. The longitudinal momenta of the decay products are $\vec{k}_p$ and $\vec{k}_{\text{HI}}$, the transverse component is $\vec{k}_{p-\text{HI}}$. The dashed area illustrates the kinematic enhancement in the laboratory in the region where $\vec{k}_{p-\text{HI}}$ has a maximum value. The corresponding angular distribution $dW/d\theta_{p-\text{HI}}$ in laboratory frame is shown in Fig. 2.6 (b). It exhibits a narrow peak near the maximum possible angle between the heavy, mother-like residual nucleus HI and the emitted proton $\theta_{p-\text{HI}}(\text{max})$. This corresponds to the situation when the proton is emitted orthogonally to the mother-particle trajectory in the rest frame. Because $\theta_{p-\text{HI}}(\text{max})$ is directly related to the decay energy Q, it is possible to derive nuclear data from the angular distributions between decay products. In the same way, the transverse momentum correlation $\vec{k}_{p1-\text{HI}} - \vec{k}_{p2-\text{HI}}$ can be replaced in the data analysis by the angular correlation $\theta_{p1-\text{HI}} - \theta_{p2-\text{HI}}$. If the initial and final states of p emission are narrow, the width of the corresponding peak in the angular distribution is governed mostly by the angular straggling of the proton in the reaction target. If those states are broad, the width results from a convolution of the states' widths with proton angular straggling [85]. It should be noted, that the sketches in Figs. 2.5 and 2.6 present the ideal cases. Contributions from several decaying states are usually seen in experimental data, which leads to complicated structures with a number of peaks. The angular-correlation data analysis can be found in Chapter 4 for the case of sequential decays of the isotopes ^{29}Ar and ^{31}Ar*.

Another important feature of the in-flight decay method is the determination of half-life limits and the measurement of half-lives. The key is the analysis of decay vertices inside or downstream from the secondary target. A decay vertex profile can be reconstructed by finding the point of the closest approach of all decay product trajectories. For illustration purposes, a cartoon of two ideal vertex profiles is shown in Fig. 2.7. A constant velocity of the beam across the target is assumed. The profile shown by the blue curve is characteristic for the case of prompt decay inside the target. Such a uniform distribution is expected for the decay of short-lived excited states, when the half-life of the mother nucleus is much smaller than the time required to pass

Figure 2.7: Sketch of two ideal vertex profiles of prompt and delayed in-flight decays, shown by blue and red curves, respectively.

through the target (under typical conditions of present in-flight decay experiments, the flight time of ions through the secondary target is of the order of 100 ps). The red curve illustrates the population of the g.s. of the mother nuclides (grow-in mode) and its delayed, radioactive decay (decay mode). The latter case is analogous to counting decay products as a function of time. Experimentally obtained vertex profiles are smeared out, because of the limited spatial resolution of the detectors and angular straggling of the decay products. Nevertheless, a Monte-Carlo simulation of the setup response is carried out so that the half-life can be estimated. An example of such analysis can be found in Chapter 6.

The very first performed in-flight decay experiment [45] proved successfully the applicability to the studies of short-lived $2p$ emitters. The experiment was devoted to the study of the previously unknown, $2p$-decaying nucleus ^{19}Mg. Indeed, the two-proton radioactivity of the g.s. of this nucleus was observed. In the experiment the trajectories of $2p$-decay products, $^{17}\mathrm{Ne} + p + p$, were measured by silicon microstrip detectors. This allowed for the reconstruction of $2p$-decay vertices and fragment correlations. The half-life of ^{19}Mg was deduced to be 4.0(15) ps. The measured angular $^{17}\mathrm{Ne} + p + p$ correlation provided the decay energy value Q_{2p} of 0.75(5) MeV. Later on, more spectroscopic information on ^{19}Mg and its $1p$-decaying sub-system ^{18}Na was deduced [77]. The angular correlation between $2p$-emission products of ^{16}Ne isotope, which was used for the calibration purposes in the first experiment, allowed for the discovery of the previously-unknown excited state of this nucleus. Besides, several new excited states in ^{15}F were discovered [30]. Later, the in-flight decay technique was applied to the studies of neutron-deficient isotopes of argon and their vicinity [46, 78, 79, 86]. Some of the results of this experiment are the subject of this thesis.

The in-flight decay technique has several advantages compared to the invariant mass method. One of them is the possible use of a thick target (e.g. up to 5 g/cm^2). Energy-loss straggling and multiple scattering inside the target material does not significantly affect the precision of the half-life determination by tracking. The errors of the decay energy measurement by the in-flight technique receive contributions only from one observable, which is the angular correlation. Last but not least, a straightforward derivation of the half-life is possible together with the spectroscopy of proton-emitting nuclei.

One possible further development and refinement of results obtained with the in-flight decay technique might be achieved by taking advantage of the precise longitudinal momentum measurement of heavy mother-like ion after the decay. This additional ob-

servable can be measured with the high momentum resolution capabilities of fragment-separator facilities like the FRS or the future Super-FRS. This has been investigated in the present work, and more details and Monte-Carlo simulations can be found in Chapter 7.

Chapter 3

The EXPERT pilot experiment

The pilot experiment of the EXPERT collaboration, labeled S388, aimed at studies of the two-proton emission processes from neutron-deficient argon and chlorine isotopes using the in-flight decay technique at the FRS. Its main objective was to discover unknown proton emitters and perform their first spectroscopy. During the run, several cases could be investigated: $2p$ emission of ^{30}Ar, ^{31}Ar* and ^{29}Ar. The study of the two latter isotopes and their nuclear sub-systems is the main subject of the present thesis. In this Chapter, the objectives of the EXPERT pilot experiment and the experimental setup within the FRS are presented.

3.1 The FRagment Separator FRS

The EXPERT pilot experiment was performed with the fragment separator FRS [3] at GSI. The FRS is a key facility for the research with exotic nuclei. The stable beams are provided by the UNILAC linear accelerator [87] and the SIS18 synchrotron [88]. An experimental complex of the institute is schematically shown in Fig. 3.1. The UNILAC is capable of accelerating ions from hydrogen to uranium to energies of 11.4 MeV/u. To reach relativistic energies, UNILAC is coupled to the SIS18 synchrotron, which provides further acceleration of ions up to a maximum magnetic rigidity of 18 Tm. The latter corresponds to an energy of about 4.5 GeV/u for hydrogen and 1 GeV/u for $^{238}U^{73+}$. After the synchrotron, the relativistic primary beam is directed to the FRS production target area TA. The secondary ion beams are produced here via fragmentation and/or fission reactions of the projectile nuclei in the target. The radioactive beams can be separated in-flight by the FRS, and the isotopes of interest are delivered to different experimental areas. For example, the FRS Ion Catcher setup [89] is located at the F4 focal plane; the F6 focus leads to the experiments in the ESR storage ring [90], etc.. The EXPERT pilot setup, temporarily placed at the F2 focal plane, will be discussed in detail in Section 3.2 of this Chapter.

The FRS is an in-flight separator for exotic radioactive beams and a magnetic spectrometer for precise momentum and angular measurements of ions with magnetic rigidities up to $B\rho = 18$ Tm [3, 91]. The separator consists of four dipole magnets for bending the passing beam by 30° each. Each dipole section is equipped with a set of quadrupole magnets to focus the beam and sextupole components for second-order ion-optical corrections. The ion-optical system of the direct branch of FRS has four focal planes corresponding to each dipole section F1, F2, F3, and F4. The spectrometer can be operated in several ion-optical modes depending on an individual

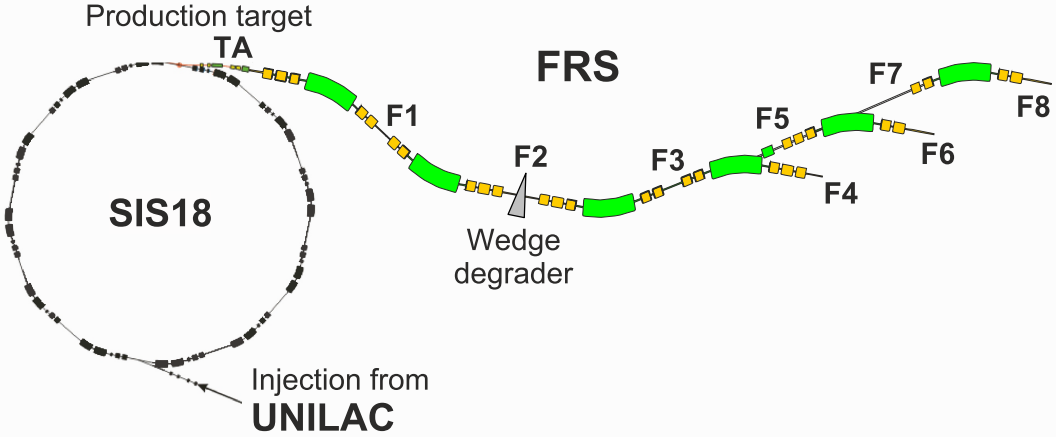

Figure 3.1: Schematic layout of the heavy-ion synchrotron SIS18 and the fragment separator FRS of GSI. The UNILAC linear accelerator injects the ion beam into the SIS18 synchrotron for further acceleration up to relativistic energies. The extracted beam is transported to the fragment separator FRS. At the entrance of the FRS, the beam interacts with the production target (TA), and a secondary beam of reaction fragments is created. These fragments are spatially separated by the FRS and can be transported to different focal planes (F4, F6, F8), where the various experiments with radioactive-ion beams take place. The direct branch of the FRS consists of four dipole sections and four focal planes, F1-F4. Bending dipole magnets are shown in green, quadrupole and sextupole magnets are shown in yellow. The wedge-shaped degrader for the separation via different energy loss preserves the achromatism of the ion-optical system.

goal of an experiment. Here, the standard achromatic mode of the FRS operation is briefly explained, and the special mode, achromatic up to F2 and dispersive up to F4, required for the present experiment is reviewed in Section 3.1.2.

The standard ion-optical mode of the FRS operation for the direct branch is an achromatic setting from the primary target at TA to F4. This means that the ions with the same $B\rho$ are focused on the same spot at the focal plane F4, regardless of the initial angular and momentum spread. For first order ion-optical matrix elements, the focusing and achromatic conditions are:

$$(x|a) = 0, \quad (x|\delta p) = 0, \quad (a|\delta p) = 0 \tag{3.1}$$

where x is the horizontal coordinate of an ion, a is its angle, $\delta p = (p - p_0)/p_0$ is the relative momentum deviation of an ion with momentum p and p_0 is a reference momentum. In x direction the point-to-point focusing is required in each focal plane, while in y direction only at F2 and F4. In this mode, the momentum acceptance of the FRS is $\Delta p/p = \pm 1\%$ including an emittance of 20 π mm mrad in both directions. The Eq. 3.1 are true at F4 focus, but the central focal plane F2 is dispersive and the dispersion coefficient is $(x|\delta p) = 6.81$ cm/%. This means, that ions with different $B\rho$ pass the middle focus at different x positions. This allows one to insert slits and thus reduce the range of accepted $B\rho$. To further separate the ions, an aluminum wedge-shaped achromatic degrader is installed at the central focal plane F2, see Fig. 3.1. Ions with the same $B\rho$ are focused at the same spot on the degrader but have different energy losses ΔE. This results in a spatial separation of different ions at the final focus

F4. This method of separation is known as $B\rho - \Delta E - B\rho$ analysis [3]. The isotopic separation is required in many cases due to the large number of different nuclides produced in fragmentation or fission reactions in the primary target.

3.1.1 Production and separation

The goal of the experiment is to study the $2p$ decays of ^{29}Ar and ^{31}Ar* isotopes by measuring their decay products in-flight. With tracking of all decay products, one can measure their angular correlation in double "heavy ion + proton" and triple "heavy ion + two protons" coincidences. The angular correlation carries information about the decay energies of $1p$- and $2p$-emission processes, thus the spectroscopy of the ^{29}Ar and ^{31}Ar nuclei can be performed. The details of the in-flight decay technique can be found in Subsection 2.6.3. The two radioactive isotopes of interest are produced in the following reactions:

$$\begin{aligned} {}^{36}\mathrm{Ar} &\xrightarrow{\text{fragmentation}} {}^{31}\mathrm{Ar} \xrightarrow{\text{inelastic scattering}} \mathbf{^{31}Ar^{*}} \xrightarrow{\text{2-proton decay}} {}^{29}\mathrm{S} + p + p \\ {}^{36}\mathrm{Ar} &\xrightarrow{\text{fragmentation}} {}^{31}\mathrm{Ar} \xrightarrow{\text{2-neutron removal}} \mathbf{^{29}Ar} \xrightarrow{\text{2-proton decay}} {}^{27}\mathrm{S} + p + p \end{aligned} \tag{3.2}$$

The schematic view illustrating the production of the reactions of interest from Eq. 3.2 is shown in Fig. 3.2. The layout of the FRS set for the EXPERT pilot experiment can be seen in panel (a), the nuclear reactions taking place at different stages of the FRS in panel (b). The primary beam of ^{36}Ar nuclei with an energy of 885 MeV/u and an intensity 10^{9} ions/s is provided by the UNILAC and SIS18 accelerators. It interacts with the 8 g/cm^{2} ^{9}Be primary target where a large variety of isotopes, including the isotope of interest ^{31}Ar, is produced in fragmentation reaction. Then, the 620 MeV/u ^{31}Ar ions with an intensity of 50 ions/s are separated and transported by the first half of the FRS to the middle focal plane F2. Here, the secondary ^{9}Be target with a thickness of 4.8 g/cm^{2} and a size of 5×5 cm^{2} is located. In the secondary target, some of the ^{31}Ar isotopes undergo inelastic excitations, producing $2p$ emitters ^{31}Ar*. Another fraction of the secondary beam loses two neutrons, thus creating ^{29}Ar radioactive isotopes. Both ^{31}Ar* and ^{29}Ar are short-lived unbound nuclei. They decay inside or right behind the secondary target, leading to two protons and a heavy ion, ^{29}S, or ^{27}S, respectively. All three decay products are tracked by the silicon detector array, see next Section 3.2 for the details of the detection setup. The second half of the FRS is set such that the HI from the $2p$ decay is transported through the ion-optical system, where it is unambiguously identified by the FRS standard PID (particle identification) detectors, which are located at F2 and the final focus F4.

It should be noted that unlike in the standard achromatic mode of the FRS operation, the aluminum wedge-shaped degrader is installed at F1 focal plane for the present in-flight decay experiment. The goal is to achieve an achromatic focus of ^{31}Ar ions already at the F2 focal plane, where the secondary target and the detection setup are placed. This special mode of the FRS ion-optical settings is discussed in the next Subsection 3.1.2.

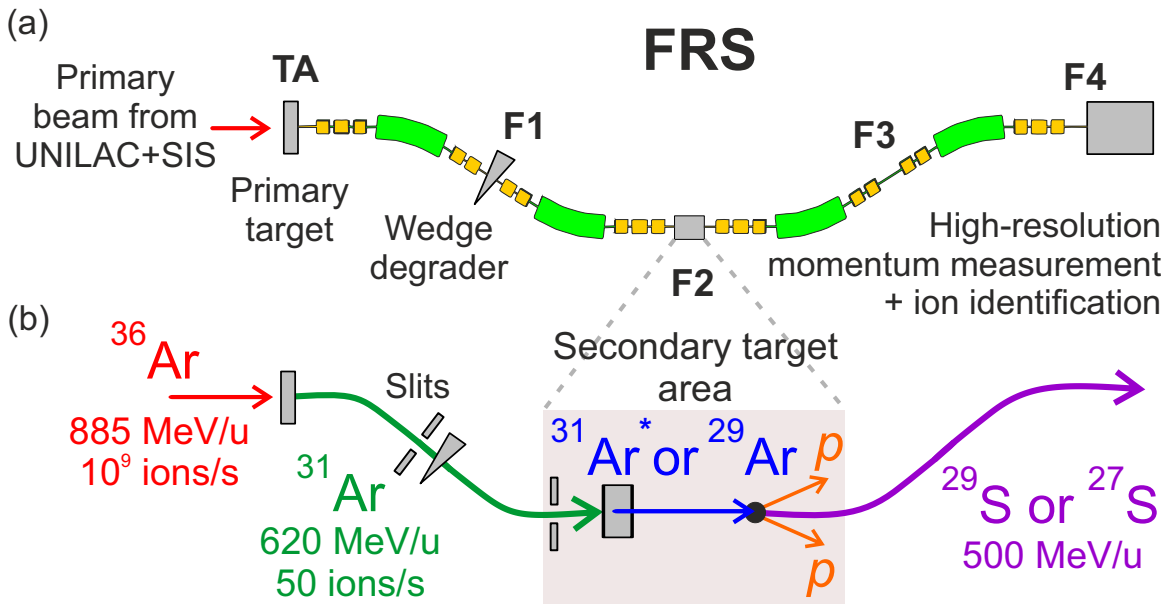

Figure 3.2: Panel (a): the schematic layout of the fragment separator FRS in its configuration for the present experiment. The wedge-shaped degrader at F1 provides achromatic conditions at the F2 focal plane (see Section 3.1.2 for details). F2 is the secondary target area, where the EXPERT prototype detectors for charged-particle tracking are placed. The focal planes F2-F4 host FRS standard detectors for high-resolution momentum measurement and particle identification. Panel (b): a schematic view of the trajectories of the ions of interest, ^{31}Ar* and ^{29}Ar, their production reactions, and the decay products together with their kinetic energies and intensities.

3.1.2 Special ion-optical mode for in-flight decay measurements

In the present experiment, the FRS is used in a new ion-optical mode. The first half of the FRS (TA – F2 section) is used as an achromatic separator. It selects the ^{31}Ar ions from the fragmentation products and focuses them on the secondary target at F2. The second half (F2 – F4) is used as a magnetic spectrometer. Its goals are an efficient transmission of the heavy proton-emission products to F4, momentum measurement of the projectile-like decay daughter and identification. This allows to study the proton emission of ^{31,29}Ar at F2 in coincidence with unambiguously identified heavy decay products ^{29,27}S from F2 to F4.

To study the proton-emission processes at the F2 focal plane, the TA – F2 dipole sections must provide an achromatic focus on the secondary target (see ion-optical achromatic conditions from Eq. 3.1). The achromatic focus is matched to the active area of the detectors. This is achieved by placing a wedge-shaped aluminum degrader at F1 focal plane. The chosen degrader thickness is 4.9 g/cm^2 on the optical axis with an angle of 194 mrad. It should be noted that the degrader can have an arbitrary mean thickness, and only the slope provides achromatism. The latter condition can only be obtained in an overall dispersive system if the angular dispersion coefficient $(a|\delta p)$ is zero without the degrader for the TA - F2 and F1 - F2 sections. This stringent requirement has been achieved with ion-optical calculations applying the programs

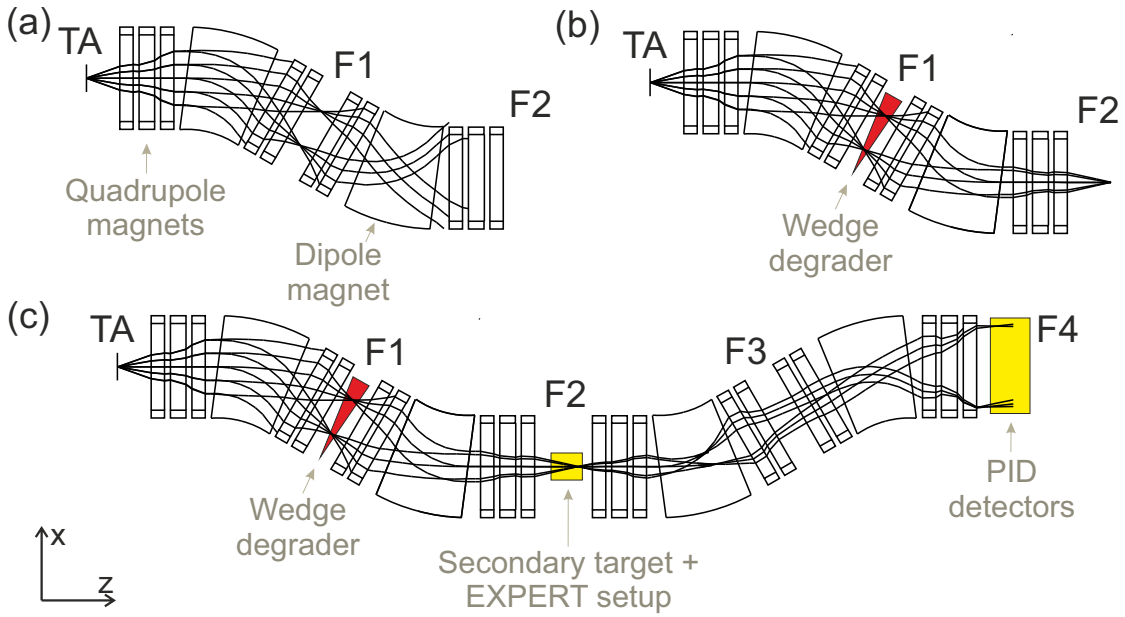

Figure 3.3: Panel (a): ion-optical mode of the FRS for TA – F2 without F1 degrader. Calculated trajectories of ^{31}Ar ions for two different relative momenta (±1%) and five different angles (0, ±4.5, ±9 mrad) are shown. Panel (b): same phase-space as in panel (a) only an achromatic degrader (colored in red) placed at F1. Panel (c): ion-optical mode of the FRS used in this experiment, which is only achromatic at F2 with the degrader inserted at F1. In this way, the beam spot is matched to the secondary target and the EXPERT tracking detector setup. The two last dipole sections F2 – F4 are operated in a dispersive mode and are used for momentum measurement and ion identification. The path length from TA to F4 along the optical axis is 73 m. The diameter of the quadrupole apertures is 0.17 m. The optical calculations are performed using the GICOSY [92] and MIRKO [93] codes.

GICOSY and MIRKO [92, 93].

The calculated ion trajectories with and without F1 degrader are shown in Fig. 3.3. The presented calculation was done using the program GICOSY [92]. On the plots, one can see the trajectories of ^{31}Ar ions with two different momenta (±1%) and five different angles (0, ±4.5, ±9 mrad) passing through the FRS dipole and quadrupole magnets. Panel (a) represents the scenario without the degrader up to F2. In panel (b), the same phase-space as in panel (a) is shown, but the achromatic wedge-shaped degrader is inserted at F1. Panel (c) presents the ion-optical mode of the FRS used in this experiment, which is only achromatic at F2 with the degrader inserted at F1. The ions with different momenta are passing through the different thicknesses of degrader matter, and the achromatic focus with a small beam spot of about 3 mm is achieved at F2.

The calculation of different ion positions in x-direction at the secondary target were performed with the LISE++ software package [94], as shown in Fig. 3.4. One can see that the main contaminants for a ^{31}Ar beam are ^{32}Ar ions. The reduction of the fragmentation background is done by closing the F1 slits to ± 14 mm and the F2 slits to ± 15 mm (the positions of the slits within the FRS geometry are schematically shown in Fig. 3.2 of the previous Section). It should be noted that the ^{31}Ar ions are

located in the center of the secondary target, and the closed slits stop the majority of the contaminants, leaving only the small fraction of ^{32}Ar ions, which are located about 10 cm off the center. The spatial contribution of the ^{32}Ar ions includes of the order of 2% of the overall ^{31}Ar intensity.

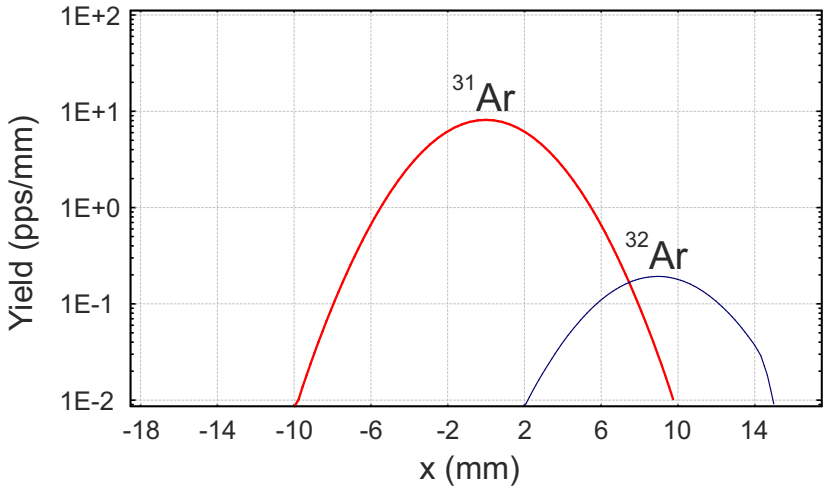

Figure 3.4: Position distribution of the incoming ^{31}Ar ions at the secondary target at F2, calculated with the LISE++ software package [94]. The simulation is set for the transmission and achromatic focusing of ^{31}Ar ions at F2. The contamination by ^{32}Ar isotopes is about 2% of the total ^{31}Ar intensity. The main simulation settings are: ^{36}Ar primary beam with an energy of 885 MeV/u and intensity of 10^9 ions/s, impinging on the 8 g/cm^2 Be primary target, a wedge-shaped Al degrader with 4.9 g/cm^2 thickness on optical axis and an wedge angle of 194 mrad at F1. The standard production mechanism of projectile-fragmentation is chosen.

In order to perform high-resolution identification and momentum measurements for the heavy decay products, the second half of the FRS is operated in a spectrometer mode as outlined in Chapter 7. The magnetic fields of F2 – F4 magnet sections are set to be dispersive, see the trajectories of ions in the Fig. 3.3 (c). The first-order resolving power at the F4 focal plane can be determined as

$$\frac{p}{\Delta p} = \frac{(x|\delta p)}{2(x|x)x_{\mathrm{TPC}}} \tag{3.3}$$

where $(x|\delta p)$ and $(x|x)$ are the dispersion and magnification coefficients, x_{TPC} is the resolution of the TPC detector (see next Section for details) at F2 focal plane. The resolving power reflects the minimum momentum difference which the system can separate. In the considered case, the resolving power of F2 – F4 section is about 4000 on event-by-event basis, including the resolution of TPC of 0.3 mm, dispersion $(x|\delta p) = 3.95$ m and magnification $(x|x) = 1.64$.

3.2 The detector setup

The detector setup of the EXPERT pilot experiment consists of two main parts: the standard FRS detectors for high-resolution momentum measurement and heavy-ion

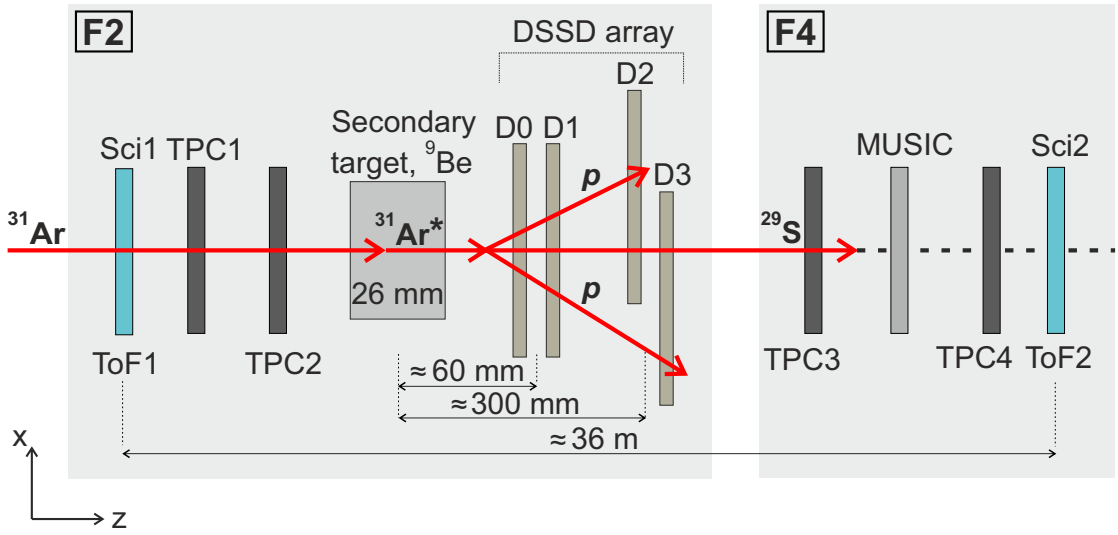

Figure 3.5: Schematic view of the EXPERT detector setup at secondary target area F2 and final focal plane F4. The trajectories of the incoming secondary-beam ^{31}Ar are measured by TPC detectors (TPC1 and TPC2) at F2. The velocity of ^{31}Ar is determined by ToF measurement between two scintillation detectors (Sci1 and Sci2). The reaction products ^{31}Ar* (or ^{29}Ar) are detected indirectly via measuring the trajectories of their decay products: two protons and the heavy ion daughter ^{29}S (or ^{27}S) using four DSSDs (light brown color). The identification of the HI is done at F4, using the energy deposition information from the MUSIC detector, tracking from the TPCs, the velocity from ToF and the magnetic rigidity $B\rho$.

identification placed at F2 and F4 focii [95] and an array of the double-sided silicon detectors for the tracking of decay products located at F2. The sketch of the setup can be seen in Fig. 3.5.

The standard FRS detectors used in the experiment are the two plastic scintillators Sci1 and Sci2 for the Time-of-Flight measurement at the F2 and F4 focal planes, respectively; the time projection chamber detectors TPCs [96] for the position measurement; and the ionization chamber MUSIC [97] for the atomic number determination. Combining the data recorded with these detectors and the magnetic rigidity $B\rho$ of the dipole sections, the mass over charge ratio A/Q and the atomic number Z can be evaluated and used to uniquely identify the heavy ions which arrive at the final focal plane F4. The details on the identification procedure of the HI from the proton decay, namely ^{29}S and ^{27}S, can be found in Subsection 4.1.2.

The heart of the EXPERT setup is a double-sided silicon detector (DSSD) array. Its main purpose is to measure the trajectories of the proton-emission products, namely the protons and the projectile-like daughter ion (heavy ion). The array consists of four microstrip DSSDs, labeled 0 to 3, placed one behind the other along the beam axis, see DSSD array in Fig. 3.5. It is known from the kinematics of the decay that the trajectories of the reaction products form a cone: the protons are emitted within an angle of a few tens of mrad relative to the heavy ion path. To register protons, the detector array is located close to the ^{9}Be 4.8 g/cm^{2} secondary target: the first detector pair (DSSD 0 and DSSD 1) is placed 6 cm and the second pair (DSSD 2 and DSSD 3) 30 cm downstream of the secondary target. The detection solid angle is enlarged by

the spatial separation of the DSSD 2 and DSSD 3 in the transverse direction (2 mm intersection) to have at least three points for the proton trajectory reconstruction. The heavy-ion decay product continues to fly very close to the trajectory of the incoming beam. It passes through all four DSSDs and then travels to the F4 focal plane. The energy deposited in DSSDs by the heavy ion (with large atomic number) is much larger than the one of the protons. Thus, it can be used as the criterion to distinguish protons and heavy decay products, see Fig. 4.2 of Chapter 4. The detectors are segmented, the readout strips have ≈ 100 μm pitch. Such properties are chosen to perform tracking with high precision. Each strip is acting as an individual detector. The general design of the DSSD detectors and the detection mechanism is discussed in the next Section 3.2.1.

The NIM- and VME-standard electronic modules for readout of the above mentioned detectors and their data streams are combined and stored by the GSI data acquisition system (DAQ) MBS [98] on the event-by-event basis. One event is caused by the trigger signal and carries the information of the signals produced by the interactions in all the detectors. In the current experiment, the signals from two scintillation detectors in coincidence are chosen as trigger: the incoming secondary ion beam interacts with the first Sci1 detector, and the outgoing fragment (for example, heavy decay product) interacts with the second Sci2. If both processes take place simultaneously (in the ns-μs range), the response from all the detectors (DSSDs and the standard FRS ones), belonging to this trigger, is stored in one event. Thus, all processes, including proton emission, are recorded, and the heavy ions of interest can be identified by the combination of F2 and F4 detectors.

3.2.1 Silicon microstrip detectors

The goal of the EXPERT pilot experiment is the precise tracking and the subsequent reconstruction of the angular correlation between all decay products. Thus the tracking array of DSSD detectors is the key component of the setup. It is comprised out of four double-sided silicon microstrip detectors, similar to those developed by the Alpha Magnetic Spectrometer (AMS) collaboration [99]. They are used as a tracker for highly-energetic cosmic particles on board of a spectrometer in space. The AMS DSSDs were designed to have a wide dynamic range and a high granularity to achieve the position resolution down to 10 μm [100, 101].

Like other silicon detectors, the principle of the DSSD detection is the following: the passing charged particle ionizes the depleted volume of the detector, creating electron-hole pairs along its trajectory. The metalized read-out strips are implants arranged orthogonally on both sides of the DSSD bulk. The arrangement of the strip implants acts as an array of charge collecting electrodes. The applied voltage forces the created free electrons and holes towards the corresponding strips, which are read-out by the front-end electronic components. In this way, the positions of the hits on both orthogonal planes (i.e., x and y coordinates of the hit) and the energy deposition of the passing particle is measured.

One DSSD is consists of a detection sensor (active area of detector) and a front-end electronic board. The sensor is schematically shown in Fig. 3.6(a). It has an area of 72×41 mm^2 and a thickness of 300 μm. The junction side (or S-side) of the sensor hosts 640 read-out strips with a pitch of 110 μm, the ohmic side (or K-side) has 384 strips with a pitch of 104 μm. The total number of strips in one sensor is 1024. To increase the position resolution and still stay within the limitations of the electronics

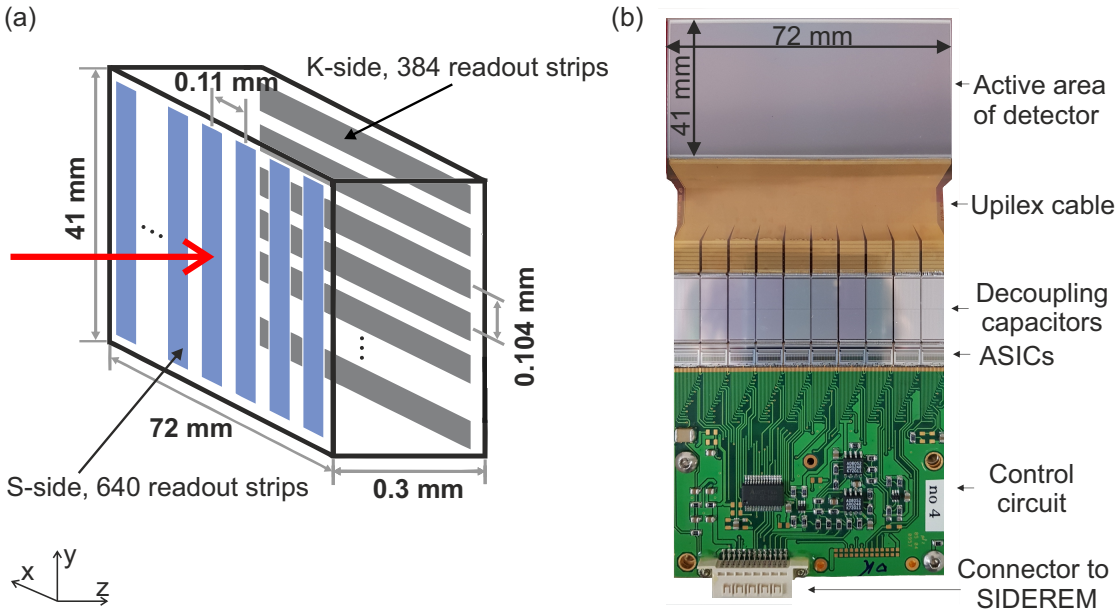

Figure 3.6: Panel (a): schematic drawing of a sensor (an active area) of the AMS double-sided silicon microstrip detector. The junction side (S-side) hosts 640 readout strips, the ohmic side (K-side) hosts 384 strips. Strip arrays are perpendicular to each other. Thus, both x and y coordinates can be measured with one detector. A red arrow represents the beam direction. The three-axis cross (on the bottom left) illustrates the orientation of detectors during the experiment. Panel (b): photo of the S-side of the AMS DSSD. The main electronic components are listed on the right of the Figure. Their description can be found in the text.

(high readout density), the readout scheme of a DSSD detector is changed in the following way for the experiment. On the S-side, an actual implantation pitch of the strips is four times smaller than the read-out one, i.e., the read-out is organized only for every fourth channel. In this way, the number of electronic channels reduces but the position resolution remains very high (about 10 μm in the best cases), due to the capacitive coupling between the adjacent implanted strips [102]. The deposited charge is shared between strips, and the number of strips fired in one interaction is almost proportional to the amount of the deposited energy. Thus, the signal position can be obtained more precisely by calculating the center-of-gravity of the charge deposit (see Eq. 4.1 of Chapter 4).

The silicon active area is connected to a front-end electronic board, see the photo of the S-side of one DSSD in Fig. 3.6 (b). The S- and K- sides of the detector are read-out independently. All strips are arranged into groups of 64, which makes 10 groups on the S-side and 6 on the K-side. First, each group is connected via a flexible Upilex cable to the capacitor chip with 64 decoupling capacitors of 725 pF each. Each group is coupled to a 64-channel high dynamic range ASIC (application-specific integrated circuit) IDE1140 or VA64HDR9A [103], which is the main component of the detector read-out[1]. Each channel of this chip hosts a charge-sensitive preamplifier, a shaper,

[1]A part of the detectors was equipped by the ASICs IDE1140, which are the updated versions of the VA64HDR9A chips.

and a sample-and-hold circuit. The channels have multiplexed analog readout, which can run at a maximum clock frequency of 10 MHz.

The S- and K- sides of the detector are connected by two flat-band cables providing power, steering and readout links to the NIM custom-designed module SIDEREM [104]. This module performs a full logic control of the front-end circuit and hosts the power supply for the detector. During the EXPERT pilot experiment, all four DSSDs with the corresponding SIDEREMs were connected to the VME-based custom-made module SAM5 [105], which reads-out, combines and integrates the DSSD data within the MBS data acquisition system. Due to the large number of channels (4×1024 for the whole DSSD array) and a multiplexing principal of the readout, the SIDEREM modules limit the read-out rate to 2.5 kHz.

Chapter 4

Data analysis

The first objective of the EXPERT pilot experiment was the production and spectroscopy of the previously-unknown isotope ^{30}Ar. It was achieved by tracking of the $2p$-emission products of ^{30}Ar. The detailed description of the procedure of corresponding data analysis and the concluded spectroscopic information on ^{30}Ar can be found in publications [86, 106].

In addition, a number of cases, interesting from the nuclear structure point of view, can be obtained from the data recorded in this experiment. Namely, excited states of ^{31}Ar are populated by various inelastic mechanisms, and the ^{29}Ar spectrum is populated by the two-neutron ($-2n$) knockout reaction. These mechanisms have smaller production cross-sections (about hundreds of μb and less), and thus the acquired data have lower statistics. The unbound ^{31}Ar and ^{29}Ar states are detected in triple ^{29}S+p+p and ^{27}S+p+p coincidences, respectively. Besides, the states of ^{30}Cl and ^{28}Cl can be populated both in the fragmentation of ^{31}Ar and as the result of proton emission from the corresponding ^{31,29}Ar isotopes. The observation of previously-unknown isotopes ^{29}Ar, ^{28,30}Cl and several nuclear-structure conclusions about ^{31}Ar*, ^{29}Ar, ^{28}Cl and ^{30}Cl are reported in reference [79], and the details of the respective analysis procedures are presented in this Chapter.

4.1 Identification of proton-emission events

Chapter 2 gives an overview, how the nuclear structure information on the resonance nuclei can be obtained from the angular correlation between their decay products. To obtain correlation of interest, one needs to find events, which belong to $2p$-emission processes, and perform tracking and identification of all decay products (HI and $2p$).

A cartoon illustrating the tracking of the decay products from a $2p$-emission event is shown in Fig. 4.1. The mother nucleus is produced by a nuclear reaction of the incoming secondary beam inside the secondary target. It is a tertiary short-lived nucleus (resonance) with a lifetime of the order of picoseconds or less. It decays inside or behind the target, resulting in two protons and a projectile-like heavy ion. An array of double-sided silicon detectors placed downstream from the target and labeled D0, D1, D2, and D3, measures the trajectories of all passing decay products. The main points of interest are the relative angles between product trajectories $\theta_{p_1\text{-HI}}$ and $\theta_{p_2\text{-HI}}$ and their derivatives. The tracking shown in Fig. 4.1 by the red arrows is applied for both reactions of interest: ^{31}Ar$^{*} \rightarrow {}^{29}$S+p+p and ^{29}Ar $\rightarrow {}^{27}$S+p+p, where ^{31}Ar* and ^{29}Ar are mother nuclei and ^{29,27}S are the heavy ion decay products.

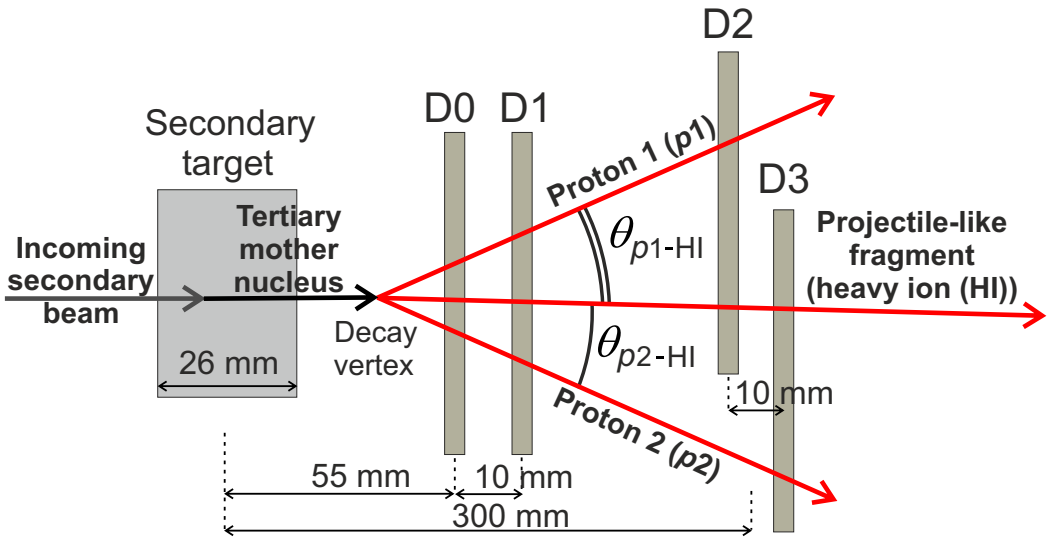

Figure 4.1: Illustration of the tracks of a $2p$-emission event. The trajectories of $2p$-emission products (shown by red arrows) are obtained by the array of double-sided silicon detectors (DSSDs) labeled D0 – D3. The corresponding decay vertex can be reconstructed and the relative angles between decay products $\theta_{p_1\text{-HI}}$ and $\theta_{p_2\text{-HI}}$ are derived. The heavy ion continues traveling through the FRS together with the secondary beam and is identified by the standard PID detectors at the final focus F4 (not shown, see Chapter 3). The protons are indistinguishable and labeled just for illustration purposes. The secondary target has transverse dimension of 5×5 cm^2 and thickness of 26 mm. The size of one DSSD is 4×7 cm^2 with the thickness of 0.3 mm, see Subsection 3.2.1 for details.

The data analysis for both $2p$ emitters of interest ^{31}Ar* and ^{29}Ar is described together in the following Subsections. It is carried out along the following steps:

- treatment of DSSD raw data,
- identification of heavy ion by the FRS standard detectors,
- identification of protons, coming from the decay,
- determination of the $2p$-emission event, by requesting coincidence of the identified heavy ion and the two protons.

4.1.1 Treatment of DSSD raw data

The treatment procedure of raw data from DSSD detectors includes the subtraction of the pedestals, identification (and exclusion from the further analysis) of broken strips, noisy strips treatment, gain corrections, and off-line detector alignment. The detailed description can be found in the reference [106].

Due to capacitive coupling between neighboring strips in a DSSD detector (see Chapter 3), several strips share an ionization charge generated by the penetrating charged particle. Such a group of strips is called a cluster, it carries information about the total deposited energy, and the hit position of the passing ion. Its position can be

determined from the center of gravity CoG of the cluster:

$$CoG = \frac{\sum_{i=a}^{b} s_i \times n_i}{\sum_{i=a}^{b} s_i}, \tag{4.1}$$

where s_i is the signal amplitude (after pedestal and noise corrections) in the i-th strip which is numbered n_i, and the sum is performed over all strips in a cluster numbered from a to b. The denominator presents the cluster integral which represents the total energy deposited by the passing particle. The distribution of the energy deposited in the D0 detector is shown in Fig. 4.2 as an example. The spectrum contains minimum ionizing particles (MIPs) and heavy-fragments contributions from triple-coincidence HI + p + p events. It can be seen that the proton signals located closer to the low-energy deposit are well-separated from the HI ones.

The CoG yields the hit position measured in units of the strip numbers. In order to convert it to the position with respect to the detector edge $X_{S,K}$, the CoG is multiplied by the value of the strip pitch:

$$X_{S,K} = CoG \times p_{S,K}, \tag{4.2}$$

where $p_S = 110$ μm is the strip pitch for S side, and the $p_K = 104$ μm is the strip pitch for K side of the DSSD. Hit positions are the main observables from the DSSD detector array. The typical number of strips in the cluster for S and Ar ions ranges from 6 to 9, see [106] for details of cluster identification. Meanwhile, protons typically trigger 1-2 strips [30, 85, 107]. The trajectories of particles are obtained by combining their hit positions measured by detectors close to the target (D0 or D1) and the ones measured by detectors located further away (D2 or D3).

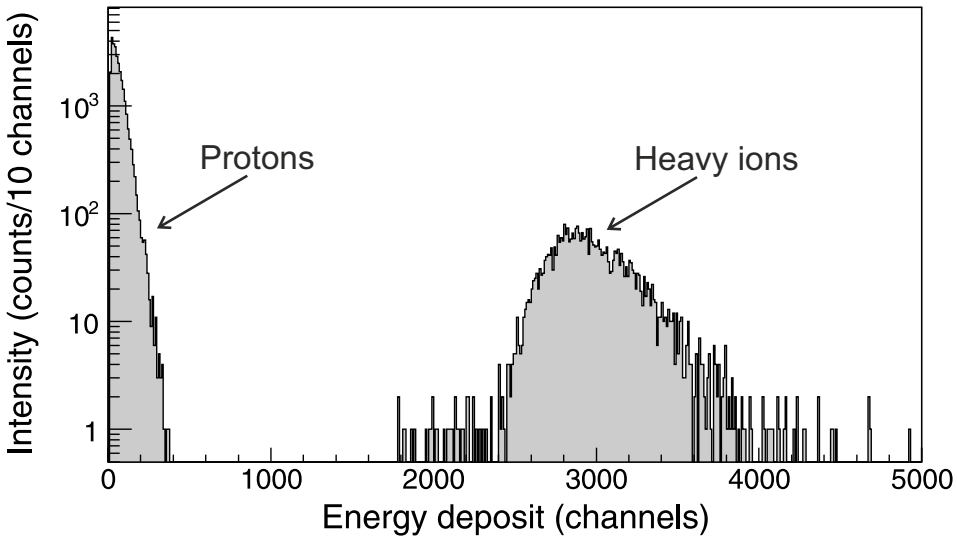

Figure 4.2: Measured distribution of the energy deposited by MIPs and heavy decay daughters in the D0 detector for the ^{29}S + p + p coincidence events. The triple-coincidence requirement has removed the noise signals.

The position uncertainty of a proton hit in the case of a homogeneous energy deposit in one strip can be expressed as:

$$\sigma^2 = \frac{1}{p}\int_{-\frac{p}{2}}^{\frac{p}{2}} x^2 dx = \frac{p^2}{12}, \tag{4.3}$$

where p is the strip pitch. The position uncertainty of the hit results in $\sigma \approx 30$ μm.

For the heavy ions, the experimental uncertainty of the cluster CoG determination is about 15 μm. It is obtained from the calibration tracking of the beam ions crossing all four DSSD planes. Namely, the difference between two alternative coordinates of the ^{31}Ar positions at the secondary target are derived from two alternative trajectories obtained by the detectors pairs D0 – D3 and D1 – D3 (or D0 – D2 and D1 – D2). The differences of positions of ions in the secondary target yield uncertainties of about 15 μm in both x and y transverse directions. It should be noted, that the HI position uncertainty is smaller than the one for protons, due to the capacitive coupling of the detectors and thus the possibility to share the charge between neighboring strips.

4.1.2 Identification of heavy ions with the FRS standard detectors

In the described experiment an unambiguous identification is required for the heavy ion originating from the proton-emission process. A heavy projectile-like decay product is usually a beta-decaying isotope (^{29,27}S in the considered case). Thus, it lives long enough time (from ms to s) to pass through the FRS and to be registered by its standard detectors. The particle identification (PID) detectors of the FRS are described in Chapter 3.

Particle identification at the FRS is done via the simultaneous measurement of magnetic rigidity of the dipole sections $B\rho$, energy deposition of the particles ΔE in the detectors placed at F4 focal plane and ToF between F2 and F4. By utilizing these values, the mass-over-charge ratio (m/Q) and the atomic number (Z) can be evaluated and used to uniquely identify all particles arriving at the final focal plane F4.

The mass-over-charge ratio can be determined according to the equation:

$$\frac{m}{Q} = \frac{B\rho e}{\beta\gamma c u}, \tag{4.4}$$

where e is the elementary charge, β is the particle velocity, γ is the corresponding Lorenz factor, u is the atomic mass unit and c is the speed of light. For particle identification, the mass number A instead of rest-mass m is sufficient, thus m/Q can be replaced by A/Q in the equation.

The velocity $\beta = v/c$ is determined by measuring the time (ToF) which the particle travels between F2 and F4 focal planes from the equation:

$$v = \frac{L}{\mathrm{ToF}}, \tag{4.5}$$

where L is the distance between F2 and F4. It should be noted that L depends also on the coordinates of the trajectories of the passing particles. The ToF measurement is obtained from the signals of the two scintillation detectors (see previous Chapter, Sci1 and Sci2 in Fig. 3.5).

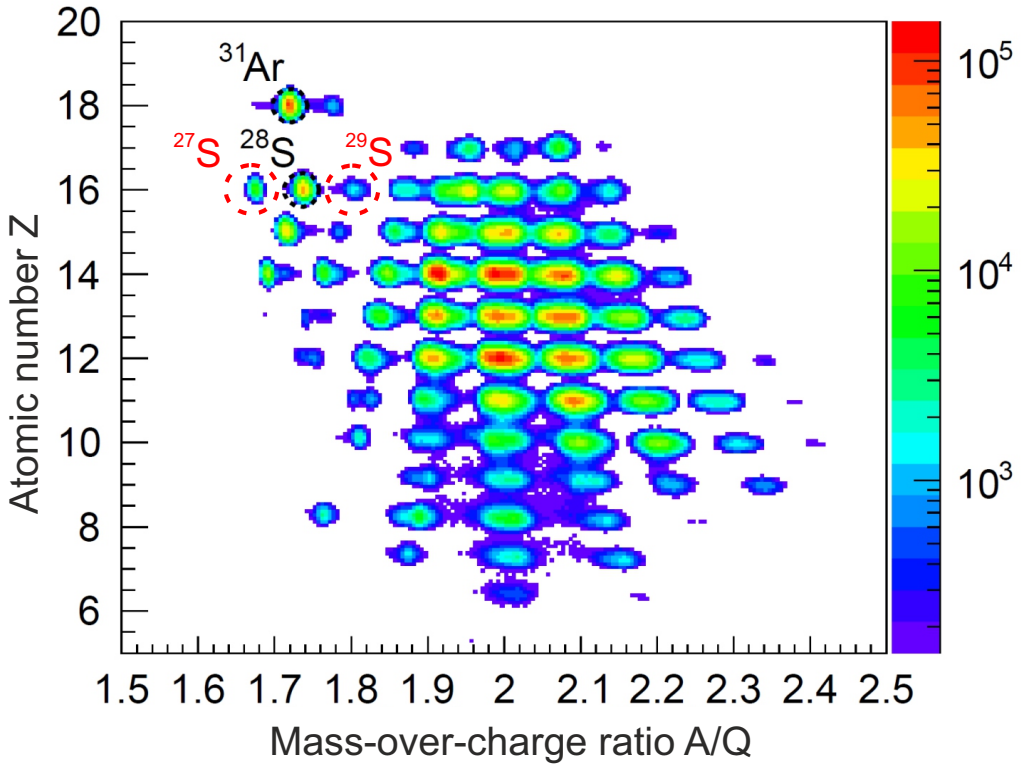

Figure 4.3: Two-dimensional particle-identification plot: atomic number Z vs. mass-over-charge ratio A/Q of the ions produced at the FRS with its first half tuned to 620 MeV/u ^{31}Ar and second half to ^{28}S. The red dashed circles show isotopes of interest, namely ^{29}S and ^{27}S. The Figure is taken from [106] and modified.

The $B\rho$ of an ion can be determined from the measured magnetic rigidity along the central optical axis of the dipole sections $B\rho_{centr}$, corrected by the entrance (F2) and exit (F4) coordinates, which allow to determine its momentum deviation:

$$B\rho = B\rho_{centr}(1 - \frac{x_{F4} - (x|x)x_{F2}}{(x|\delta p)}), \tag{4.6}$$

where x_{F2} and x_{F4} are coordinates of the particles trajectories at F2 and F4, $(x|x)$ and $(x|\delta p)$ are the magnification and dispersion optical coefficients from F2 to F4. The $B\rho_{centr}$ is given by the current of corresponding dipole sections. The position measurements are done by TPC detectors at the F2 and F4 focii, and the optical coefficients are known from the ion-optical settings of the separator.

The ions' charge can be deduced from the energy deposition measurement according to the following relation:

$$\Delta E \sim \frac{Z^2}{\beta^2}, \tag{4.7}$$

Such an approximation works under the assumption that ions are fully stripped, i.e., $Q = Z$ and the stopping power can be described by the first Born approximation. During the experiment, this condition was fulfilled due to the relativistic energy of the beam, and its rather small atomic number ($Z = 18$, only $\approx 10^{-5}$ of the ions capture electron). The ΔE was measured by the MUSIC detector located at F4.

All the above-mentioned standard FRS detectors were calibrated with the primary beam of ^{36}Ar at three different velocities. Then the mass-over-charge ratio A/Q and the atomic number Z spectra were obtained for the fragments of interest. In Fig. 4.3 the two-dimensional particle identification plot for the ^{31}Ar - ^{28}S production setting is shown. This setting was a primary objective of the experiment, aimed at studying the one-neutron removal process and subsequent $2p$ emission from ^{30}Ar [46, 86, 106]. However, the data analysis showed that the same data set contains also such processes as inelastic scattering and two-neutron knock-out followed by $2p$ emission from ^{31}Ar* and ^{29}Ar, respectively. The spots belonging to the heavy products of those reactions, namely to the ^{29}S and ^{27}S ions, are seen on the identification plot in Fig. 4.3, marked by the red dashed circles. These highlighted areas contain a fraction of ions originating from $2p$-emission processes.

The analysis steps are essentially similar for both ^{31,29}Ar $2p$ emitters, namely for the identification of decay-originating ^{29,27}S heavy ions and their tracking. The events corresponding to the ^{31}Ar* decay were obtained with more statistics, so the analysis procedures are illustrated with the example of ^{29}S ions in this Chapter.

Naturally, to select the HI of interest, namely ^{29}S, one needs to apply a gate to the particle-identification plot from Fig. 4.3. Thus, the contributions from other nuclear species are eliminated. However, the isotope selection from PID plot is necessary but not sufficient. As a next step, one has to spatially-separate the ^{29}S ions coming from the decay in the secondary target from the ones coming from the fragmentation reactions in the primary target.

To facilitate the search, the transverse positions of ions in the microstrip detectors are determined. The x-coordinate distribution from D0 detector is shown in Fig. 4.4. The distribution comprises the ^{31}Ar ions, selected by their energy deposit in TPC2 (TPC detectors are also capable of energy deposition measurement although with less

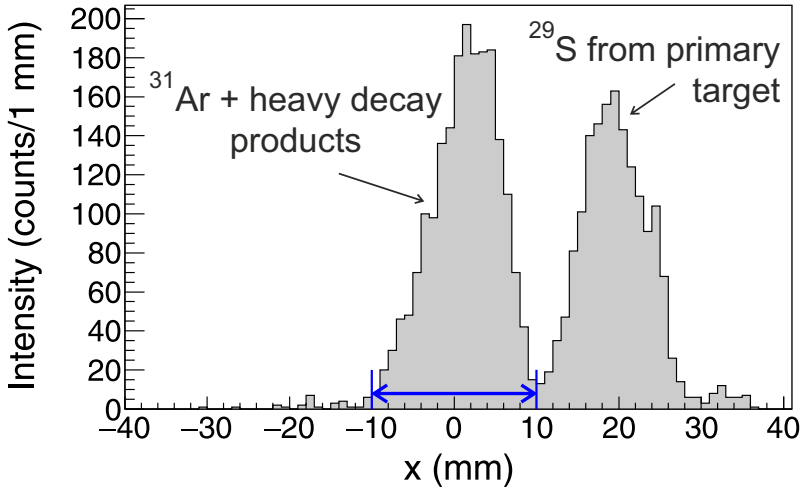

Figure 4.4: Position distribution of ions measured by the D0 microstrip detector placed directly behind the secondary target. The central peak belongs to the unreacted ^{31}Ar ions (coming from the primary target at the TA area) together with its decay daughters ^{29}S. The off-center peak contains the ^{29}S ions coming from the primary target at TA. The selection gate on the central peak and thus the ^{29}S ions of interest is shown by the blue arrow.

precision compared to MUSIC), and the ^{29}S ions from the PID plot selection. The position distribution reflects the $B\rho$ and thus also A/Q separation of the ions, see Eq. 4.4. The A/Q ratio is very different for the ^{31}Ar and ^{29}S isotopes. Thus, those nuclear species are well separated spatially. The contribution of the ^{32}Ar ions, which have a similar A/Q ratio with ^{29}S and thus can be mixed with it, is negligible, see Fig. 3.4 of the Chapter 3. The distribution in Fig. 4.4 comprises two major components: the unreacted in secondary target ^{31}Ar ions together with ^{29}S ions from the proton-emission reactions, and the fragmentation ^{29}S ions from primary target area. The unreacted ^{31}Ar ions together with the decay-originating ^{29}S ions are located in the center of the D0 detector[1]. Due to the kinematics of the reaction, heavy decay products continue to follow the longitudinal beam direction with only 0.5 mrad angular deviation. And the primary ^{29}S isotopes formed in the TA area, are off-center in the D0 (and D1). The spatial separation between the two peaks is seen. Thus, one can apply the selection gate on the central peak. This removes the contamination from the primary ^{29}S ions.

With the applied selections, the ^{29}S heavy ions of interest are identified. Their hit positions in the DSSD detectors and thus, their trajectories, are determined. However, some contamination from primary ^{29}S fragments coming from the production target TA and the ones produced in the degrader can be completely removed by the triple-coincidence $^{29}\mathrm{S} + p + p$ decay events. The latter is described in the next Subsection.

4.1.3 Identification of protons

As it was mentioned in Subsection 4.1.1 of this Chapter and based on the experience from previous experiments [85], protons induce signals in one to two strips when passing through the DSSD detectors. The challenge here is to separate the strips belonging to the proton events from the ones hit by other minimum ionizing particles. For example, MIPs, like δ-electrons created by the high-energy beam ions in the secondary target, may pass through the DSSDs and produce signals similar to the proton ones.

The trajectories of protons can be determined and used to exclude MIP events and the background noise. Background noise is eliminated automatically because there is no coincidence of signals in different DSSDs in this case. MIPs can still pass through all 3 DSSDs, but due to the multiple scattering, their trajectories will differ from a straight line (reference line) by the scattering angle ϕ. Protons also never have ideal linear trajectories but suffer much less from scattering in the DSSDs than the light δ-electrons. For proton candidates, the angle ϕ will have a smaller value. Thus, a threshold value of ϕ_{thr} can be set. The ϕ_{thr} is about 5 mrad, this value is chosen empirically. If $\phi < \phi_{thr}$, the selected trajectory is assumed to belong to a proton. Additionally, the extrapolated longitudinal positions of the proton-candidates show, that some of the events originate in front of the secondary target (taking into account its longitudinal dimensions of 26 mm). Those events are also considered to be δ-electrons and excluded from the analysis. However, some contaminants might still originate within the target and pass through the DSSD array following a straight line. Then, the most strict selection criterion is the tracking of all $2p$-decay components in coincidence. The search of the actual $2p$-emission events is described in the following Subsection.

[1]Prior to the experiment, the secondary target and first two DSSD detectors were aligned along with their centers and a longitudinal beam direction, see Fig. 3.5 with the detection setup.

4.1.4 Determination of $2p$-emission events

So far, the heavy ions of interest, ^{29}S and ^{27}S, have been unambiguously identified and their trajectories together with the ones of the proton candidates have been determined, see Subsections 4.1.2 and 4.1.3. Now, one can start looking for those events, which include all these components in coincidence. For a $2p$ decay all three particles originate from the same point in space, the decay vertex of the $2p$-emission event of ^{31}Ar* or ^{29}Ar. To find these events, the point of minimum approach of the three trajectories (belonging to HI and two protons) has to be determined.

The procedure of decay vertex determination is illustrated in Fig. 4.5. First, the minimum distance between $p1$ and the HI trajectory is found. It is shown by the red segment, which is perpendicular to both of the trajectories. This distance has be to smaller than the empirical threshold value of 180 μm. If not, then another proton candidate is considered. The minimum distance distribution derived from the ^{29}S $+ p$ coincidence between D0 and D2 detectors is shown in Fig. 4.6 (a). The threshold value is determined by the accuracy of the position measurement with the DSSD and the requested experimental precision. If this condition is fulfilled for the selected HI - $p1$ pair of trajectories, the meeting point is considered to be the middle point of the minimum distance segment. Second, the procedure is repeated for the $p2$ - HI pair of trajectories, and the corresponding meeting point is found. Thus, two double coincidence events HI + p can be found and their vertices can be determined.

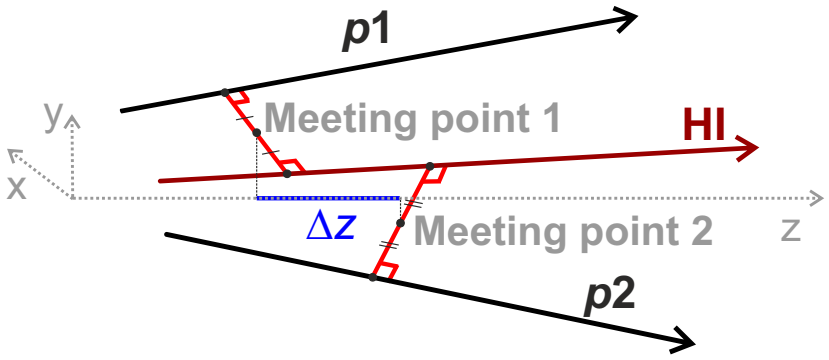

Figure 4.5: Cartoon illustrating the search for $2p$-emission events. The minimal distance between a pair of trajectories $p1$ - HI is shown by the red segment, the meeting point of these trajectories is the center of the segment. The same treatment is applied for the $p2$ - HI pair. The blue line represents the difference between the longitudinal coordinates of the two meeting points Δz. If Δz is smaller than a certain value (see text for details), then the two p - HI pairs are considered to originate from the same $2p$-emission event.

To find the triple coincidence event HI + p + p, the longitudinal coordinates of the two previously determined meeting points are calculated. The difference between their two longitudinal coordinates Δz, see illustration in Fig. 4.5 and data in Fig. 4.6 (b), is required to coincide within $\pm$ 3 mm. If the condition on Δz is fulfilled, then the two protons and the heavy ion are considered to originate from the same $2p$-emission event, and the decay vertex is determined. In longitudinal (along beam) direction, the uncertainty of the vertex position depends on the relative angles between HI and protons in the same triple coincidence event HI + p + p. If HI - p angles are small,

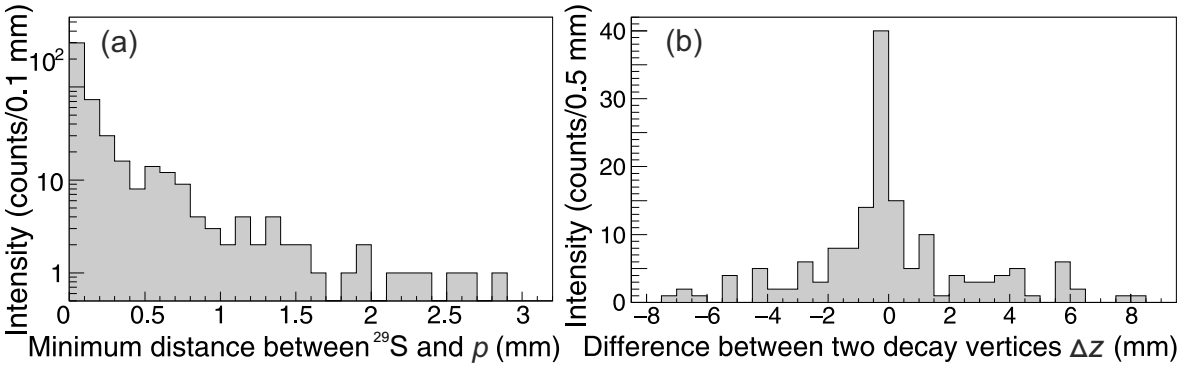

Figure 4.6: Panel (a): measured distance of closest approach of two trajectories of a proton and ^{29}S ion. The tracking information is extracted from the D0 and D2 microstrip detectors, taking into account the double $^{29}\mathrm{S} + p$ coincidence events. Panel (b): the measured difference between two longitudinal coordinates of the decay vertices Δz, defined for the $p1$ - ^{29}S and $p2$ - ^{29}S trajectories taken from the same triple-coincidence event.

the vertex uncertainty becomes larger, because ions and protons move almost parallel to each other. Typical uncertainties range from 0.3 to 1 mm. The uncertainty of the vertex distribution of n events is smaller by the factor of $1/\sqrt{n}$ in comparison with a single event. The angular uncertainty receives its largest contribution from the proton straggling in the DSSDs. The achieved angular resolution in fragment tracking is about 1 mrad [46]. It is measured by taking the difference between relative angles $\theta_{p-\mathrm{HI}}$ of two trajectories measured by alternative detector pairs D0 – D3 and D1 – D3. Similar resolution is obtained with the D0 – D2 and D1 – D2 detector pairs.

Finally, all the analysis steps outlined in Section 4.1 have been performed. The triple-coincidence $^{29}\mathrm{S} + p + p$ events, which pass the selection procedure described above, can be considered as $2p$-emission events of $^{31}\mathrm{Ar}^{*}$. One of such events found in the D1 microstrip detector is presented in Fig. 4.7. The large clusters of strips produced by ^{29}S ions and the two-proton hits are seen on both sides of the detector. The δ-electron contribution, excluded from the analysis, see Subsection 4.1.3, is also visible on the S-side of the detector.

The analysis procedures, described in this Section 4.1, are essentially similar for both $2p$-emission processes $^{29}\mathrm{S}{+}p{+}p$ and $^{27}\mathrm{S}{+}p{+}p$, since those events have been produced under the same experimental conditions.

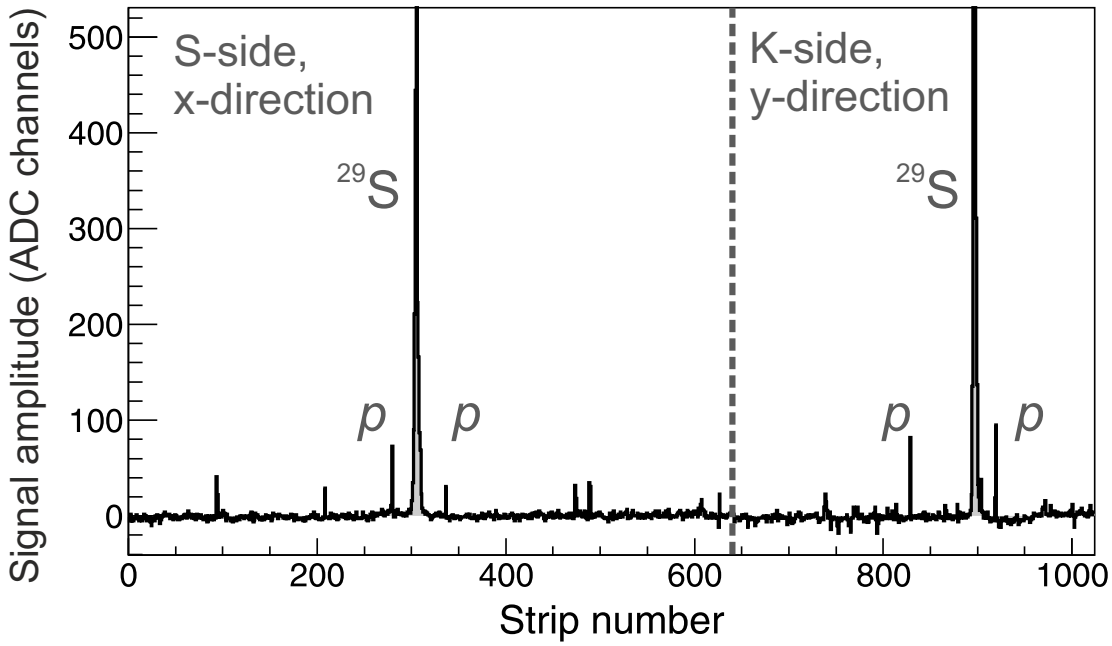

Figure 4.7: Signals of one $2p$-emission event of the ^{31}Ar excited state, measured by the D1 microstrip detector. The Figure is divided into two parts by the dashed vertical line, where each part represents a detector side. The clusters of strips corresponding to the ^{29}S and $2p$ hits are visible on both sides of the detector. The spectrum also contains the δ-electron hits, which are excluded from the analysis by the characteristic angular scattering.

4.2 Analysis of ^{29}Ar data

In the previous Section, the analysis steps taken for the ^{31}Ar* and ^{29}Ar decay-products determination were described. Decay-products trajectories for the double- and triple-coincidence 2p-emission events were identified. Subsection 2.6.3 showed that the angular correlation of the proton-emission products can provide insights to the level structure of the decaying nucleus. In this Section, the analysis of the angular distributions for ^{27}S+p+p events is described, and the first spectroscopic results for the previously-unknown isotope ^{29}Ar are presented.

4.2.1 Angular correlation of ^{27}S and protons

The measured ^{27}S+p+p angular correlation can be displayed via different representations, each of them gives hints on the structure of ^{29}Ar nucleus and its short-lived sub-system ^{27}S + p or ^{28}Cl.

One representation is a two-dimensional scatter plot, where the angle between the trajectories of ^{27}S and p_1, $\theta_{p_1\text{-}^{27}\text{S}}$, versus the angle between ^{27}S and p_2, $\theta_{p_2\text{-}^{27}\text{S}}$, are depicted, see Fig. 4.8. During the experiment seven 2p-decay events were measured in ^{27}S+p+p coincidence. Each of these events provides a pair of angles $\theta_{p\text{-}^{27}\text{S}}$, because the protons are indistinguishable from each other. This results in a symmetric scatter plot. The plot carries information about the mechanism of proton emission and the energy level structure of ^{29}Ar. The correspondence of the angular distribution with the

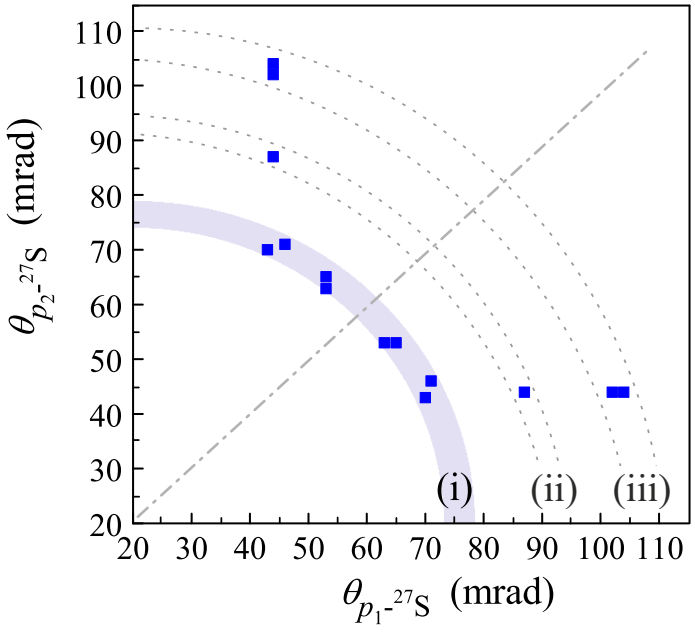

Figure 4.8: Angular correlation $\theta_{p_1\text{-}^{27}\text{S}} - \theta_{p_2\text{-}^{27}\text{S}}$ produced from the measured ^{27}S+p+p coincidences. Every blue square represents one count, 7 triple-coincidence events in total are shown in total. The shaded arc (i), where the 2p-decay events have the same decay energy, indicates a certain state in ^{29}Ar. The dashed arcs labeled (ii) and (iii) indicate possible locations of two less-pronounced states in ^{29}Ar. The dash-dotted line shows the symmetry line with respect to proton permutation, and p_1 and p_2 are labeled just for illustration purposes.

decay dynamics is reviewed in Chapter 2, namely see Figs. 2.5 (b) and 2.6. The events on the plot form groups along the contour of an arc. Each group comprises events, which share the total $2p$-decay energy of a precursor, i.e. ^{29}Ar in this case. Based on the theory support from Chapter 2 and the previous experiments [46, 45], the three states in ^{29}Ar can be assigned tentatively. The most prominent group of four triple-coincidence events placed along the blue-shaded arc is labeled (i), these events belong presumably to the first excited state in ^{29}Ar. There are two more groups, labeled (ii) and (iii), with just a couple of events. They might belong to high-lying excited states in ^{29}Ar. It is rather difficult to assign a specific decay mechanism (true or sequential emission of a proton) to the ^{29}Ar isotope from the scarce information of the scatter plot. Nevertheless, it is known that in the case of simultaneous emission, protons share the total decay energy Q_{2p} equally. This doesn't seem to be the case for ^{29}Ar. Also, this isotope has not been predicted to be a true $2p$ emitter by the three-body model [53].

The next step in the analysis is to understand, how the total $2p$-decay energy Q_{2p} is shared between the protons belonging to the same state, and to assign to each p-emission process its decay energy Q_p. To facilitate this, the special kinematic variable ρ_θ is used:

$$\rho_\theta(^{27}\mathrm{S}+p+p) = \sqrt{\theta^2_{p_1\text{-}^{27}\mathrm{S}} + \theta^2_{p_2\text{-}^{27}\mathrm{S}}}, \tag{4.8}$$

The three-body variable ρ_θ reflects the energy sum of both emitted protons, which is a constant. It represents the radius of the arcs in the scatter plot in Fig. 4.8. The ρ_θ is related to the total decay energy as $\rho^2_\theta \sim Q_{2p}$. This variable can be used to identify

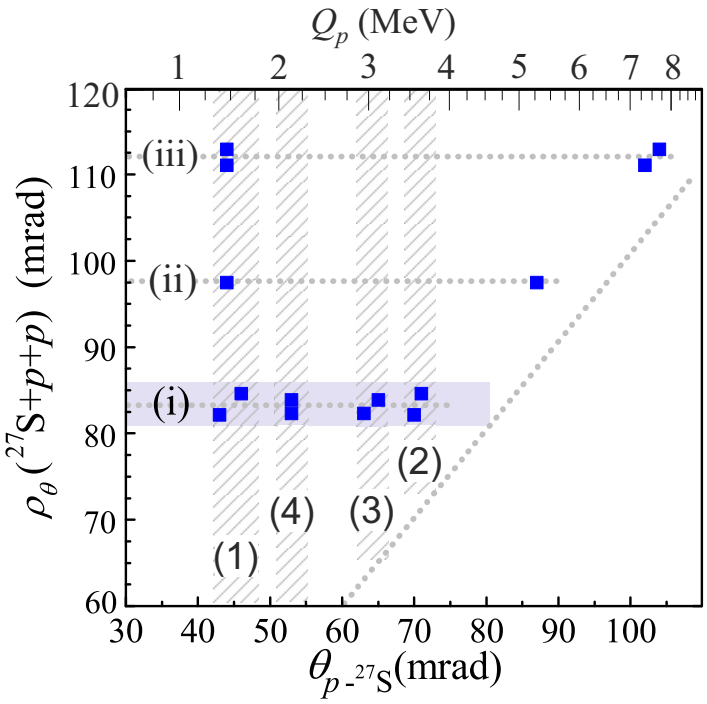

Figure 4.9: Angular correlation $\theta_{p\text{-}^{27}\mathrm{S}} - \rho_\theta$ presenting $2p$ decays of different ^{29}Ar states, dotted horizontal lines show groups of events belonging to three states, and $1p$-decay of its sub-system ^{28}Cl, dashed vertical areas give hints to the resonant states labeled (1 – 4). Each blue square represents one measured event. The upper axis shows the corresponding $1p$-decay energies Q_p. The tilted dotted line shows the kinematical limit.

certain $2p$-precursor states. In the case of ^{29}Ar, the ρ_θ-selection is not applied during the analysis, because all triple-coincidence events form well-distinguished groups. However, the representation of the angular correlation data using ρ_θ facilitates the analysis, see Fig. 4.9. It displays both, the ^{29}Ar states and the structure of the ^{28}Cl isotope.

The Figure 4.9 shows a two-dimensional plot $\theta_{p\text{-}^{27}\mathrm{S}} - \rho_\theta$. The three groups of events labeled (i – iii) belong presumably to the states in ^{29}Ar and agree with those on the scatter plot in Fig. 4.8. The hatched areas labeled (1 – 4) highlight the events from the decay of ^{27}S + p resonance assigned as ground state (1) and three excited states (2 – 4) of ^{28}Cl. The upper axis of Fig. 4.9 shows the corresponding $1p$-decay energies Q_p. The scaling to $1p$-decay energies here is approximate, it is based on the quadratic dependence of the Q_p on the relative angle, see Eq. 2.16 in Chapter 2. The calibration is taken from the known $2p$ emitter ^{19}Mg [45, 108], whose decay was re-measured exactly for the calibration purposes in the same experiment.

Let us first consider the prominent group of events located around $\theta_{p\text{-}^{27}\mathrm{S}} \approx 45$ mrad, area (1) and $\rho_\theta \approx 84$ mrad, area (i) in Fig. 4.9. The most-populated state (1) is assigned to be the g.s. of ^{28}Cl with $Q_p \approx 1.6$ MeV. The $2p$-decay state (i) of ^{29}Ar can be roughly assigned the Q_{2p} of about 5.5 MeV. The challenge is to find the second proton, the separation energy of which contributes to the total decay energy Q_{2p} of the state (i) in ^{29}Ar. This proton can be hidden in the areas (2), (3) or (4) in Fig. 4.9. The projection of Fig. 4.9 on the $\theta_{p\text{-}^{27}\mathrm{S}}$ axis facilitates the search, see blue-filled histogram in Fig. 4.10. The double-coincidence $\theta_{p\text{-}^{27}\mathrm{S}}$ angular correlation spectrum is shown in the same plot by the gray-filled histogram. The locations of the possible resonant states of ^{28}Cl are labeled (1 – 4) like in the Fig. 4.9. It is seen from Fig. 4.10, that the coincidence spectrum "supports" the triple coincidence spectrum and enhances the peaks of interest. The peak (2) has the $Q_p = 3.9(1)$ MeV, and together with peak (1)

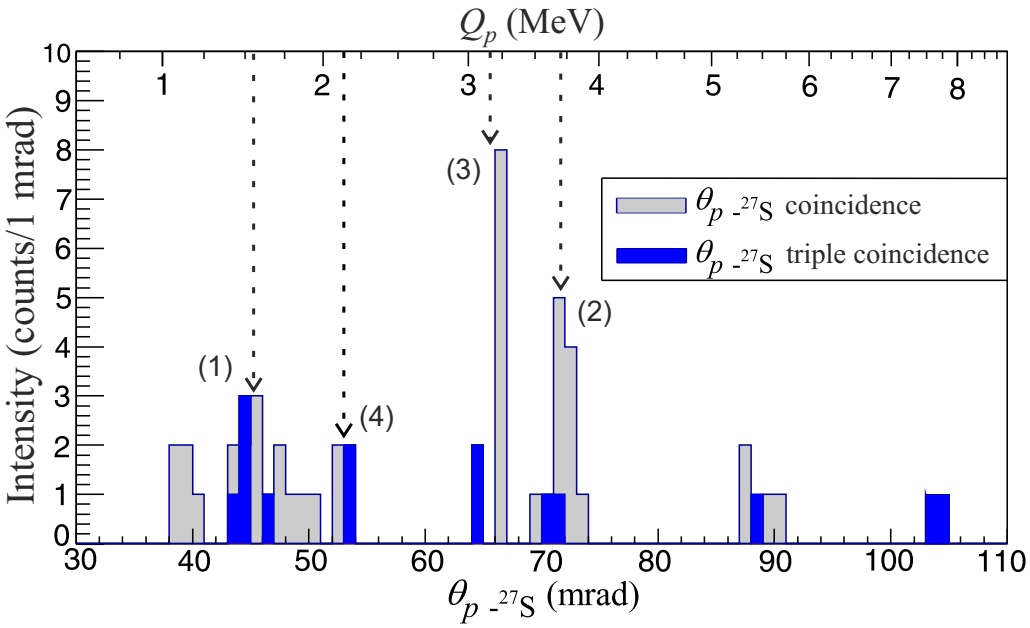

Figure 4.10: Angular correlation $\theta_{p\text{-}^{27}\mathrm{S}}$ obtained for coincidence events ^{27}S+p (gray histogram, "inclusive spectrum") and triple-coincidences ^{27}S+p+p (blue histogram). The arrows labeled (1) – (4) highlight events that are candidates for possible ^{28}Cl resonance states. The upper axis shows the corresponding $1p$-decay energies Q_p.

of $Q_p = 1.60(8)$ MeV they give the total $Q_{2p} = 5.50(18)$ MeV of the first excited state (i) in ^{29}Ar. The statistical uncertainties of Q_p and Q_{2p} are estimated from Monte-Carlo simulations of the setup response, see the next Subsection for details.

There are two more peaks in angular spectrum in Fig. 4.10 labeled (3) and (4). It is known from Fig. 4.9, that both protons contributing to those states come from the 5.5 MeV first excited state of ^{29}Ar. The peak (3) is assumed to belong to the second excited state of ^{28}Cl with $Q_p = 3.20(6)$ MeV because it is more pronounced than (4) and might be additionally populated from another unspecified reaction channels (not seen in the recorded data). The tentative assignment of peak (3) is related to the energy of peak (4) around 2.2 - 2.3 MeV. This is the least populated state, but its location on the energy scale supports the above-drawn assignments.

In addition, there are indications for ^{27}S+p+p correlation at ρ_θ of 97 and 112 mrad (states (ii) and (iii) in Fig. 4.9), which may correspond to $2p$ decays of ^{29}Ar with Q_{2p} of about 7.2 and 9.5 MeV, respectively. Both states have the second-emitted proton energy of 1.6 MeV, which corresponds to the lowest assigned state in ^{28}Cl.

4.2.2 Monte-Carlo simulations of the setup response

To quantitatively reproduce the data, justify the above-assigned decay energies and give their values with the uncertainties, detailed Monte-Carlo simulation of the detector setup response has been performed. Moreover, reproducing the behavior of the detector setup to a certain type of radiation, one can gain an understanding of the physics processes involved. The Monte-Carlo calculations described here have been performed by using the GEANT simulation framework [109]. The libraries of the GEANT package include the relativistic kinematics and information on the processes of interaction of the relativistic particles with matter. GEANT allows for the implementation of the geometry of the setup and tracking in the virtual environment similar to the real experiment conditions.

As an example, let us describe the simulations of the $2p$-emission process of ^{29}Ar. The goal of the simulation is to understand the transformation from momentum to angular correlation of the ^{29}Ar decay products. As mentioned above, the proton-emission mechanism of ^{29}Ar is assumed to be sequential, so its implementation in the simulation code is done via two subsequent two-body decays: $^{29}\mathrm{Ar} \rightarrow {}^{28}\mathrm{Cl} + p$, and then $^{28}\mathrm{Cl} \rightarrow {}^{27}\mathrm{S} + p$. The nuclei ^{29}Ar and ^{28}Cl are hitherto-unknown resonances. Their lifetimes are chosen as 10^{-19} s. The masses of those isotopes should also be provided as parameters to the simulation, and are calculated in the following way:

$$\begin{aligned} m_{^{28}\mathrm{Cl}}c^2 &= m_{^{27}\mathrm{S}}c^2 + m_p c^2 + Q_p, \\ m_{^{29}\mathrm{Ar}}c^2 &= m_{^{27}\mathrm{S}}c^2 + 2m_p c^2 + Q_{2p}, \end{aligned} \tag{4.9}$$

where $m_{^{29}\mathrm{Ar}}$, $m_{^{28}\mathrm{Cl}}$, and $m_{^{27}\mathrm{S}}$ are the masses of the related isotopes; m_p is a mass of the proton; Q_p, Q_{2p} are the $1p$- and $2p$- decay energies, respectively.

The simulation starts from a randomly-chosen point in the secondary target, which acts as decay vertex, i.e., the point where the heavy daughter ion and 2 protons are created. The tracking of the HI and $2p$ is performed throughout the matter of the secondary target and the DSSD array. The detection efficiency and the angular straggling in the detectors are taken into account. The uncertainties in the position and vertex determination are also included in the simulation code. Then, the resulting simulated

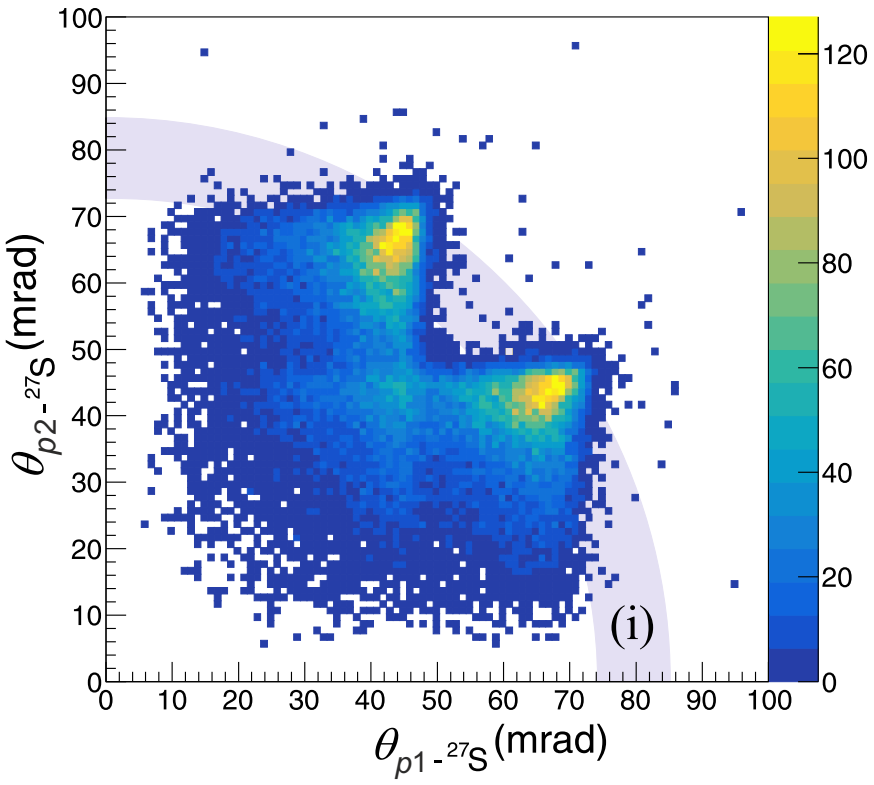

Figure 4.11: Calculated angular correlation $\theta_{p_1\text{-}^{27}S} - \theta_{p_2\text{-}^{27}S}$ obtained from a Monte-Carlo simulation of the setup response for the $2p$ emission of ^{29}Ar with the total decay energy $Q_{2p} = 5.5$ MeV, going sequentially by $1p$ emission via the intermediate state in ^{28}Cl with $Q_p = 1.6$ MeV. The arc (i) indicates the simulated state (i) in the experimental scatter plot in Fig. 4.8.

data are analyzed in the same way using the corresponding conditions and selections as the experimental data.

The result of the simulation of the sequential $2p$ decay of ^{29}Ar with $Q_p = 1.6$ MeV and $Q_{2p} = 5.5$ MeV is shown in Fig. 4.11. The two-peak pattern is characteristic for the sequential emission, see Fig. 2.5 (b) of Chapter 2. The extended "tails" of the simulated peaks are due to the kinematics of the proton emission and an angular straggling in the target and the detector setup. The scatter plot, presented in Fig. 4.11, supports the experimental one in Fig. 4.8.

The measured and simulated angular distributions can now be compared to obtain the decay energy and its uncertainty. The peak (1) around 45 mrad from the double-coincidence ^{27}S+p spectrum in Fig. 4.10, which is assumed to belong to the ^{28}Cl g.s., is compared with the corresponding simulation, see Fig. 4.12 (a). The angular distribution with $Q_p = 1.6$ MeV is shown by the red dashed curve, the data are presented by the gray-filled histogram with the statistical error bars. To get the uncertainty of the determined decay energy, several simulations with different Q_p values have been carried out. For each calculation, the probability that the simulated peak matches the data can be calculated by using the standard statistical Kolmogorov-Smirnov test [110]: this maximum-likelihood test yields the probability that two distributions have the same shape. The obtained probabilities versus the varied Q_p energies are shown in Fig. 4.12 (b). The simulation reproduces the data in the 45 mrad angle region quanti-

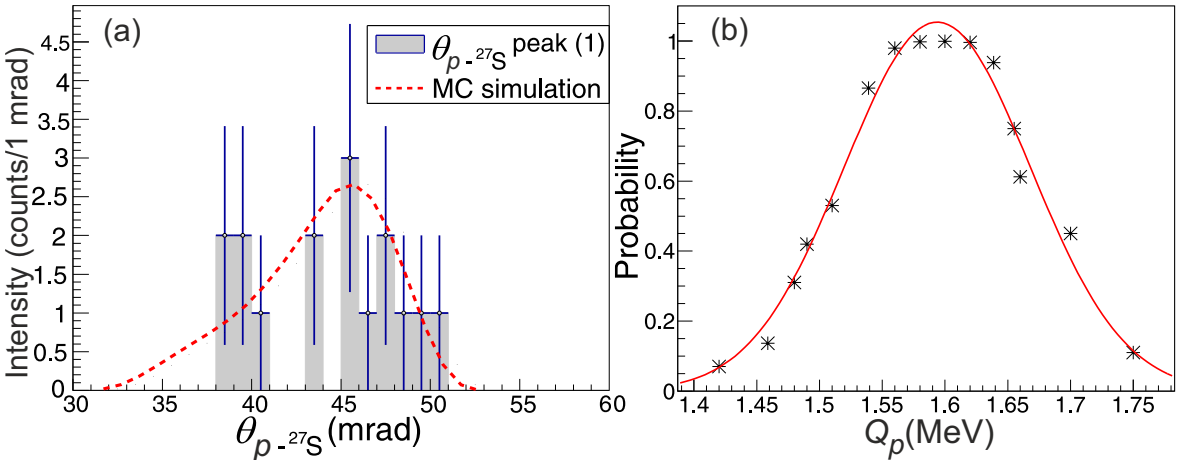

Figure 4.12: Panel (a): Monte-Carlo simulation compared to the angular distribution of the peak (1) of the $\theta_{p\text{-}^{27}S}$ "inclusive" angular correlation shown in Fig. 4.10 providing the value of $Q_p = 1.6$ MeV. The simulated setup response to the in-flight decays of ^{28}Cl is shown by the dashed red curve, the data are represented by the filled histogram. Panel (b): probability that the simulated distribution matches the data of peak (1) in Fig. 4.10 as a function of the decay energy Q_p. The red curve represents a Gaussian function, which is used to fit the calculated data. The derived $1p$-decay energy including its uncertainty is $Q_p = 1.60(8)$ MeV.

tatively with $Q_p = 1.60(8)$ MeV. The evaluated uncertainty of the fitted value is given by the energy range, where the experimental data are described by the simulation with probabilities above 50%. The red curve in Fig. 4.12 (b) is a Gaussian fit function. The same analysis procedure is performed for the ^{27}S + p peaks (2) and (3) in Fig. 4.10, providing the decay energies of 3.9(1) MeV and 3.20(6) MeV, respectively.

Based on the obtained results, the level scheme of ^{29}Ar and its sub-system ^{28}Cl is built, see Fig. 4.13. It should be noted that all the mentioned energies are given with respect to the $2p$-emission threshold.

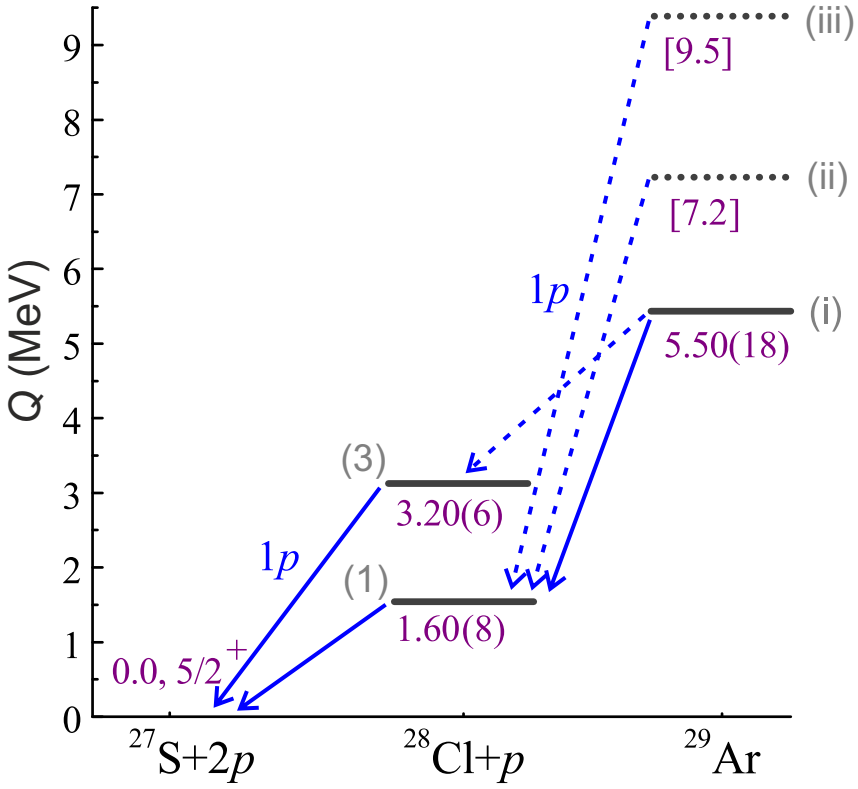

Figure 4.13: Decay scheme of ^{29}Ar and its sub-system ^{28}Cl. The assigned $1p$ transitions and the decay energies are shown by blue solid arrows and black level lines with numerals, respectively. The dashed arrows indicate tentatively assumed $1p$ transitions. The dotted levels indicate very tentative assignments based on only one or two $2p$-decay events. The vertical axis shows the energies relative to $1p$ (for ^{28}Cl) and $2p$ (for ^{29}Ar) emission thresholds. Roman and Arabic gray numerals present the naming of the ^{29}Ar and ^{28}Cl states in the data analysis.

4.3 Analysis of ^{31}Ar* data

This Section describes the analysis of the excited states of ^{31}Ar, derived from the ^{29}S+p+p triple-coincidence data. The data treatment is much more complicated than the ^{29}Ar case because the angular correlation receives contributions from a larger number of decaying states. Thus the proton disentanglement procedure is somewhat more complex. However, the method of data interpretation and the analysis steps remain the same, as described in Section 4.2, and lead to the assignment of the levels in ^{31}Ar and the previously-unknown ^{30}Cl resonances.

4.3.1 Angular correlation of ^{29}S and protons

The angular scatter plot, displaying the relative angles between ^{29}S and protons measured in triple-coincidence, is presented in Fig. 4.14 (a). Similar to the previous analysis, the events carrying information about different excited states of ^{31}Ar are tentatively selected in arcs and labeled by Roman numerals. The same groups of events can be seen in the extended angular correlation plot $\theta_{p\text{-}^{29}\mathrm{S}} - \rho_\theta$ in Fig. 4.14 (b). The ρ_θ variable is the root-mean-square (r.m.s.) relative angle, calculated for ^{29}S and protons by using the Eq. 4.8. The events in groups (i) – (vii) in Fig. 4.14 (b) belong to the decays of

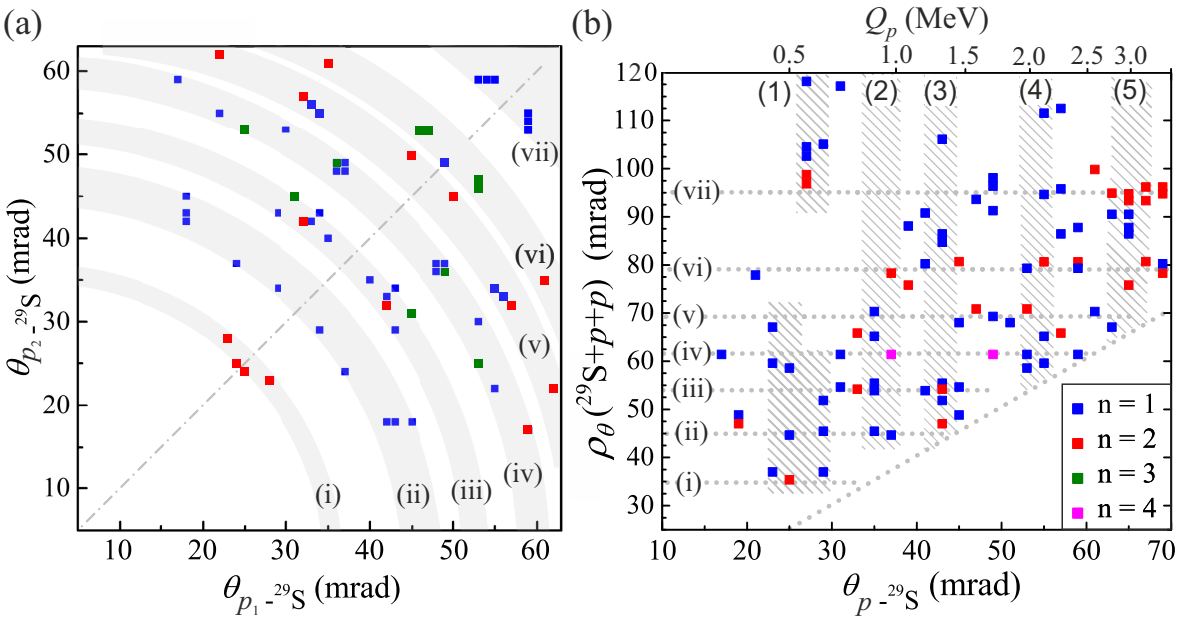

Figure 4.14: Panel (a): angular correlation $\theta_{p_1\text{-}^{29}\mathrm{S}} - \theta_{p_2\text{-}^{29}\mathrm{S}}$ deduced from the measured ^{29}S+p+p coincidences indicating 2p decays of ^{31}Ar excited states. The shaded arcs labeled by Roman numerals point to seven areas where the 2p-decay events have the same decay energy. The dash-dotted line shows symmetry with respect to proton permutations, p_1 and p_2 are numbered only for illustration purposes. Panel (b): extended angular correlation plot $\theta_{p\text{-}^{29}\mathrm{S}} - \rho_\theta$. Dotted lines labeled (i) – (vii) guide the eye to the assumed states of ^{31}Ar, hatched areas (1) – (5) indicate the decay events of ^{30}Cl. The corresponding proton-decay energies Q_p in MeV are shown in the upper axis. The tilted dash-dotted line is the kinematic limit. The color code represents the number of counts on both panels, see the legend.

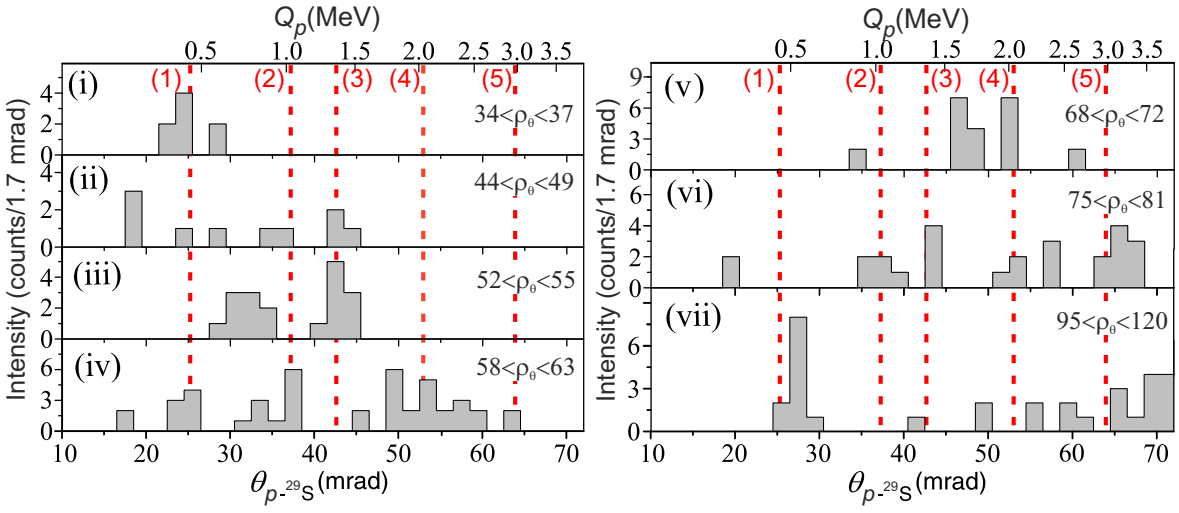

Figure 4.15: The angular correlation $\theta_{p\text{-}^{29}S}$ for triple-coincidence events ^{29}S+p+p corresponding to different r.m.s. angle ρ_θ selections. The range of ρ_θ can be seen on the right side of each histogram labeled (i) to (vii). The five red dashed lines labeled (1) to (5) guide the eye to the possible resonant states in ^{30}Cl. The upper axis shows the corresponding 1p-decay energies Q_p.

different states of ^{31}Ar, and the events in hatched areas belong to ^{30}Cl ones. Again, the challenge is to solve the "crossword" of the decay pattern and correctly assign proton-decay energies to each state. In order to understand the ^{31}Ar decay pattern shown in Fig. 4.14 (b), the ρ_θ variable can be used. By gating on ρ_θ, one can select states in ^{31}Ar and find out energies of protons which contribute to those states. The projections of each selected group of events (i) – (vii) on the $\theta_{p\text{-}^{29}S}$ axis are shown in Fig. 4.15. The gated projections exhibit several low-statistics peak-like structures, which correspond to protons with different decay energies. The red dashed lines mark the locations of the peaks assumed to belong to the five ^{30}Cl states labeled (1) to (5). Similar to the ^{29}Ar analysis procedure, the coincidence ^{29}S+p spectrum is built to tune the positions of the peaks, see Fig. 4.16. There, one can distinguish the peaks more clearly. Their

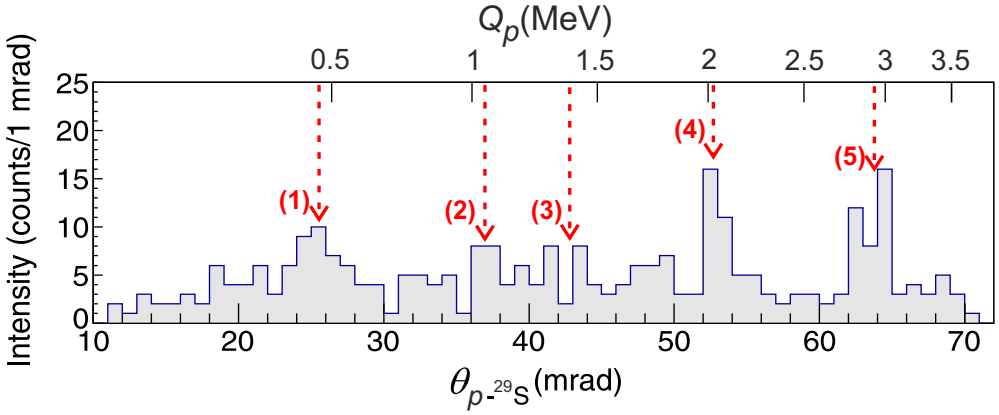

Figure 4.16: Angular correlation $\theta_{p\text{-}^{29}S}$ for double-coincidence events ^{29}S+p. The five red dashed arrows labeled (1) to (5) guide the eye to the possible resonant states in ^{30}Cl.

assumed positions are pointed by red dashed arrows labeled (1) to (5). To define the positions of the peaks quantitatively, one has to perform Monte-Carlo simulations of the detector setup response.

4.3.2 Monte-Carlo simulations of the setup response

For each peak-like structure in the angular correlation, Monte-Carlo simulations have been performed. The simulations allow to deduce the decay energy of a state and its uncertainty. The detailed explanation of the simulation procedure can be found in Subsection 4.2.2 for the example of ^{29}Ar. Here, the procedure is applied to the coincidence spectrum in Fig. 4.16 and the resulting simulation curves are shown in Fig. 4.17.

The peaks (1), (4), and (5) are assigned to 1p-decay energies Q_p of 0.48(2), 2.00(5), and 3.0(2) MeV, respectively. The peaks (2) and (3) exhibit of less confidence. Nevertheless, the fitting procedure allowed for the tentative assignment of the proton-decay energies of 0.97(3) and 1.35(5) MeV, respectively. After defining several states in the ^{30}Cl, one can assign the transitions between the excited states of ^{31}Ar and its subsystem ^{30}Cl.

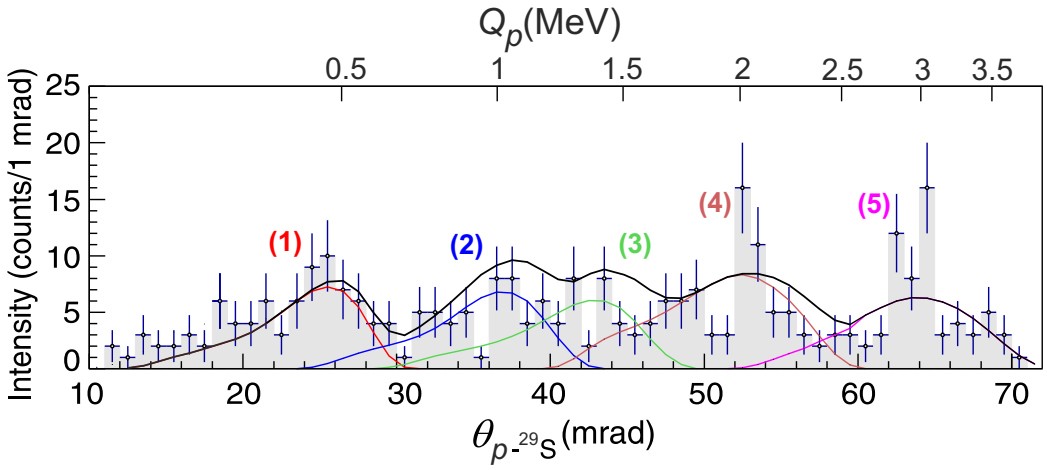

Figure 4.17: The angular correlation of ^{29}S and one of the protons $\theta_{p\text{-}^{29}S}$ (inclusive spectrum with statistical uncertainties) is shown by the gray-filled histogram. The distribution reflects the states in the ^{30}Cl subsystem of ^{31}Ar. Monte-Carlo simulation curves for the different resonant states, numbered (1) to (5), are shown with colored curves, and the sum of the simulation results is the black line. The upper axis shows the corresponding 1p-decay energies Q_p.

4.3.3 Interpretation of the ^{31}Ar* and ^{30}Cl data

As a starting point, let us consider the assignment of the earlier-defined peak (1) with $Q_p = 0.48(2)$ MeV. This is a candidate for the ground state of ^{30}Cl. Such an assignment is supported by the observed ^{29}S+p+p correlation, where one of the emitted protons has a relatively large energy (i.e., de-excitation from continuum) and the other proton energy is peaked around 0.5 MeV, see Fig. 4.15(vii). This is a typical situation for

a final-state interaction due to the ^{30}Cl g.s. resonance, see the illustration of proton-emission scenarios in Fig. 2.5 (c) of Chapter 2. The assignment of the ^{30}Cl g.s. is a very important starting point in the overall interpretation of the data before one can turn to the assignment of the decay energies to the excited states in ^{31}Ar. To make this procedure clear, each gated projection from Fig. 4.15 is considered, and their interpretation is explained stepwise below.

- The first candidate for a ^{31}Ar state is located in the (i)-th gated projection in Fig. 4.15. It has only one peak-like structure around 0.5 MeV in a low-angle region, which corresponds to the peak (1) or the g.s. of ^{30}Cl. One can assume that the second peak is also hidden in the same angular region. The two emitted protons have indistinguishable energies in this experiment. With the fixed ^{30}Cl g.s. energy, a simulation of sequential proton emission from the ^{31}Ar excited state via the ^{30}Cl g.s. is performed. The obtained value for the $2p$-decay energy is $Q_{2p} = 0.95(5)$ MeV.
- The gated angular correlation (ii) and (iii) indicates the same peak around 43 mrad, which corresponds to the peak (3) with $Q_p = 1.35(5)$ MeV in the ^{30}Cl-proton double-coincidence correlation. This means that the states (ii) and (iii) decay via the same state in ^{30}Cl. Like in the previous step, the simulation of sequential proton emission of ^{31}Ar via the 1.35(5) MeV state in ^{30}Cl is performed. It gives the two $2p$-decay energies of 1.58(6) and 2.12(7) MeV, respectively.
- The correlations (iv) and (v) have only one "intersection point". Namely, it is the peak-like structure around 53 mrad which, corresponds to the state (4) in ^{30}Cl with assigned $Q_p = 2.00(5)$ MeV. This fact gives a hint that the $2p$ emission from (iv) and (v) states occurs via the same state in ^{30}Cl. One can notice that the projection (iv) has several rather broad structures. Their interpretation is discussed below. The projection (v) has two structures around 48 and 53 mrad, which can be interpreted as contributions from the same state in ^{31}Ar. The latter one decays via the 2.00(5) MeV state in ^{30}Cl. The comparison between the angular distribution with this double-structure and the simulation gives $Q_p = 1.56(10)$ MeV. Together with the 2.00(5) MeV state in ^{30}Cl, the assignment of a new ^{31}Ar state with $Q_{2p} = 3.56(15)$ MeV is made.
- Let us get back to the consideration of the gated projection (iv) in more detail. It has the peak around 37 mrad, which "intersects" with the peak (2) of ^{30}Cl with $Q_p = 0.97(3)$ MeV and the broad distribution around 53 mrad corresponding to peak (4) with $Q_p = 2.00(5)$ MeV. One may assume that the chosen state in ^{31}Ar can decay via two different intermediate states. The corresponding simulations of two such scenarios give the two $2p$-decay energies of $Q_{2p} = 0.97(3) + 1.65(10) = 2.62(13)$ and of $Q_{2p} = 2.00(5) + 0.45(3) = 2.45(8)$ MeV, respectively. These two values agree within the statistical uncertainties. It should be noted that the assigned $2p$-decay branch via the 2.00 MeV state in ^{30}Cl has the first-emitted proton energy of 0.45(3) MeV, which coincides with the $1p$-decay energy of the g.s. of ^{30}Cl. Therefore the sequential $2p$ decay may proceed also via the g.s. of ^{30}Cl, and these two assignments are indistinguishable. Due to this uncertainty, the $2p$-decay energy of 2.62(13) MeV is tentatively assigned to the ^{31}Ar state.
- Also the projection (vi) has several peak-like structures. Each of them can possibly be a candidate of a ^{31}Ar state. The states on the "crossing points" (like structures at 37 and 43 mrad) could also belong to the ^{30}Cl spectrum. The ^{31}Ar $2p$ decay could

follow via one of its states. The simulation of $2p$-sequential emission was carried out for each combination. As a result, the only energetically-possible combination is the 0.97(3) MeV intermediate state in ^{30}Cl (assigned before) plus the Q_p of 3.2(2) MeV. The 0.97(3) MeV state is located at 37 mrad, and the 3.2(2) MeV is located at the 66 mrad. The two fitted values allow for the assignment of the excited state in ^{31}Ar with the total decay energy $Q_{2p} = 4.4(2)$ MeV.

- As discussed above, the peak around 26 mrad in both Figs. 4.15(vii) and 4.16 is assigned to the ^{30}Cl g.s. There is no other clear peak in (vii) projection but a broad data structure above 65 mrad. This gives a hint that the proton originates from the continuum spectrum. Then it also contributes to the corresponding peak (5) of ^{30}Cl, see Fig. 4.16. It is a well-populated state with the assigned $Q_p = 3.0(2)$ MeV. It might be populated by the deexcitation from the ^{31}Ar continuum above 5 – 6 MeV.

All assigned states and decay branches are summarized in the level scheme of the ^{31}Ar, and its subsystem ^{30}Cl, see Fig. 4.18.

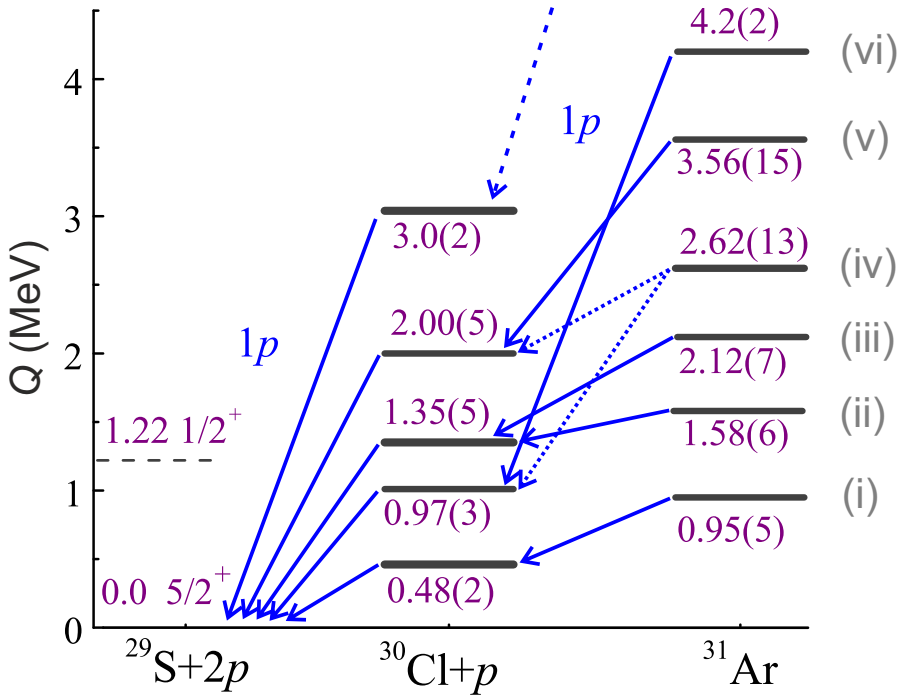

Figure 4.18: Decay scheme of ^{31}Ar and its sub-system ^{30}Cl derived from the data. The assigned $1p$ transitions are shown by the blue solid arrows. The dotted arrows show two indistinguishable decay branches of the 2.62(13) MeV state in ^{31}Ar, and the dashed arrow indicates a $1p$ transition from the unidentified states in ^{31}Ar feeding the 3.0(2) MeV state in ^{30}Cl. The vertical axis shows the energies relative to the $1p$ (for ^{30}Cl) and $2p$ (for ^{31}Ar) emission thresholds. Roman numerals present notations of the ^{31}Ar states in the data analysis.

Chapter 5

Discussion of the obtained nuclear-structure information

The decay and level schemes of $2p$-emitting ^{29,31}Ar isotopes have been assigned on the basis of the analysis of angular correlation between their decay products, see Figs. 4.13 and 4.18, respectively. In this Chapter, an interpretation of the obtained spectroscopic results is presented.

5.1 Estimation of the ^{31}Ar ground state energy

One of the fundamental properties of the nuclear force is its charge independence. Protons and neutrons with the same quantum numbers (e.g., orbital momentum, spin, isospin, etc.) are equivalent in the strong interaction. Precisely, the pair of protons, neutrons, and a proton and a neutron have equal interaction strength if the electromagnetic interaction is not taken into account. If one considers an isobar chain with mass number A, then the (A, Z) nucleus at the proton-rich side and the $(A, N) = (A, A-Z)$ nucleus at the neutron-rich side are equivalent within the accuracy of Coulomb interaction. Therefore, the structure of unknown proton-rich systems may be predicted by their known neutron-rich so-called isobaric mirror partners.

The isobaric mirror partner of ^{31}Ar is ^{31}Al. It has inverse numbers of protons and neutrons. The level scheme of ^{31}Al is known from the literature, see [111]. The obtained excitation spectrum of ^{31}Ar exhibits a high level of isobaric symmetry with respect to the ^{31}Al one. Namely, the states in ^{31}Ar with the assigned decay energies Q_{2p} of 0.95(5), 1.58(6), 2.12(7) and 2.62(13) are in correspondence with the states in ^{31}Al with excitation energies E^* of 0.9467(3), 1.61297(24), 2.090(11) and 2.676(28) MeV, respectively. Thus, one can assume that the ground states of both mirror nuclei are separated by the same energy from their excited states. This assumption allows for an estimation of the Q_{2p} for the ^{31}Ar ground state.

First, the corresponding levels in ^{31}Ar – ^{31}Al isotopes are combined into four pairs. Then the energy difference is calculated for each pair. This yields four estimations of Q_{2p}: 3(50), -33(60), 30(81) and -56(158) keV, respectively. Finally, the weighted mean of those pairs provides an averaged value of Q_{2p} = -6(34) keV for the g.s. of ^{31}Ar. This evaluation is an agreement with all previous estimates of this value, see Table 5.1. The latter are made within the β-delayed proton decay studies of the ^{31}Ar isotope, namely $\beta 2p$ [112, 113] and $\beta 3p$ [114, 115]. The evaluation of Q_{2p} = -6(34) keV for the g.s. of ^{31}Ar from this work is the most accurate, it improves the result of the previous

Table 5.1: $2p$-decay energies Q_{2p} for ^{31}Ar g.s. according to different experiments.

Q_{2p}(keV)	Reference
-6(34)	this work, [79]
3(110)	[112]
-100(210)	[21]
37(103)	[113]
70(100)	[115]

estimate by a factor of three.

However, in all the cases experimental errors do not allow for the determination of the sign of the decay (or separation, $Q_{2p} = -S_{2p}$) energy of ^{31}Ar. Thus it is unclear whether the g.s. of this isotope is bound or not with respect to $2p$ emission. The conclusion of this work is that the ^{31}Ar g.s. is bound. One argument in favor of such a conclusion is a high level of isobaric symmetry of this isotope. Though for the unbound neutron-deficient *sd*-shell nuclei the isobaric symmetry breaking (Thomas-Ehrman shift (TES) [116, 117]) is a common feature, it is not observed in the ^{31}Ar – ^{31}Al mirror nuclei pair. Recently, shell-model calculations [118] predicted the S_{2p} value of ^{31}Ar. The calculated value from [118] agrees with the measured value $S_{2p} = 6(34)$ keV, providing the positive sign of S_{2p}. The latter gives additional support to the conclusion that the ^{31}Ar g.s. is bound with respect to $2p$ emission. On the contrary, if the ^{31}Ar g.s. is $2p$-unbound, its partial $2p$-decay half-life is much longer than the β-decay one. The upper limit on the branching ratio for $2p$ decay of this isotope has been recently determined to be $7(2) \times 10^{-4}$ [114]. The latter was done within the studies of $\beta 3p$ decay of ^{31}Ar. The obtained limit on the branching ratio corresponds to a $2p$ partial lifetime larger than several ten seconds.

To clarify the $2p$-decay scenario of the ^{31}Ar g.s., the mass of this nucleus has to be measured with high accuracy and precision of a few keV [119]. This was not possible up to now. One interesting effect of the loosely-bound ^{31}Ar g.s. may be the possible existence of a $2p$ halo in this nucleus. Calculations of halo-configurations for the systems with three-body binding energy less than 100 keV [120] provide some theoretical support for this effect.

5.2 Systematics of $2p$-emitting argon isotopes

Based on the isobaric symmetry effect, briefly explained in the previous Section, one can systematically evaluate the energies of states in argon isotopes ^{29,31}Ar. The systematic evaluation of the chlorine isotopic chain can be found in publication [79].

The evolution of $2p$-separation energies in argon isotopes and corresponding isobaric mirror partners can be presented using odd-even staggering (OES) energies. The OES energy is defined as

$$2E_{\mathrm{OES}} = S_{2p}^{(A)} - 2S_{p}^{(A-1)}, \tag{5.1}$$

where $S_{2p,p}$ are the one- or two- proton separation energies of the decaying system with mass number A and its sub-system with mass number $A - 1$. The E_{OES} for the neutron-rich mirror nucleus is defined in the same way using $S_{2n,n}$ neutron separation energies. The E_{OES} reflects the nuclear pairing gap and shows the trend with A. Such

systematics has been used to evaluate the prescribed separation energies in several cases [46, 55].

The systematics of $2E_{\mathrm{OES}}$ is presented in Fig. 5.1. Each panel of Fig. 5.1 shows the $2E_{\mathrm{OES}}$ of isotonic and isotopic chains leading to the $2E_{\mathrm{OES}}$ of ^{31,30,29}Ar in panels (a),(b) and (c), respectively. The staggering energies for neutron-rich mirror partners are also shown in each panel. One can see that the shift between two trends is very stable, also the E_{OES} decreases with the mass number. Thus one can evaluate how the newly-derived $2p$ separation energies used for the $2E_{\mathrm{OES}}$ calculation follow the tendency.

For example, the E_{OES} for ^{30}Ar is smaller than expected from the systematics, see Fig. 5.1 (b). Such a behavior is explained by the three-body Thomas-Ehrman shift effect [121]. As mentioned in the previous Section, the ^{31}Ar g.s. demonstrates no TES, and its spectrum displays a high level of isobaric symmetry. Its $2E_{\mathrm{OES}}$ value follows the systematic trend, see Fig. 5.1 (a). The latter is an additional argument in favor of the isobaric symmetry in the ^{31}Ar – ^{31}Al mirror pair. The $2E_{\mathrm{OES}} = 0.966(74)$ MeV for ^{31}Ar is calculated according to Eq. 5.1 using the estimated $S_{2p}(^{31}\mathrm{Ar}) = 6(34)$ keV and measured $S_p(^{30}\mathrm{Cl}) = -0.48(2)$ MeV values.

In the case of ^{29}Ar, the $2E_{\mathrm{OES}}$ trend can help to understand whether the observed state with $S_{2p} = -5.50(18)$ MeV can be assigned to the g.s. of ^{29}Ar or not. The extrapolated $2E_{\mathrm{OES}}$ value for this isotope is 0.361 MeV, see Fig. 5.1 (c). However, the $2E_{\mathrm{OES}}$ of ^{29}Ar might not follow the systematic trend (as it was shown for the $2p$-unbound ^{30}Ar g.s.) and have a smaller value due to the expected TES. The assumed variation of the $2E_{\mathrm{OES}}$ is within the 0.310 – 0.361 MeV range. Then the derived value of $S_{2p} = -2.93(25)$ MeV may be considered for the g.s. of ^{29}Ar using the measured $S_p = -1.60(8)$ MeV. According to such an estimate, the level observed in ^{29}Ar with $S_{2p} = -5.50(18)$ MeV cannot be assigned to its ground state, therefore it is one of the excited states of this isotope. The prediction of ^{29}Ar g.s. based on the OES systematics does not quite agree with the predictions from other theoretical calculations like [122]. Therefore, this matter is a subject for further studies.

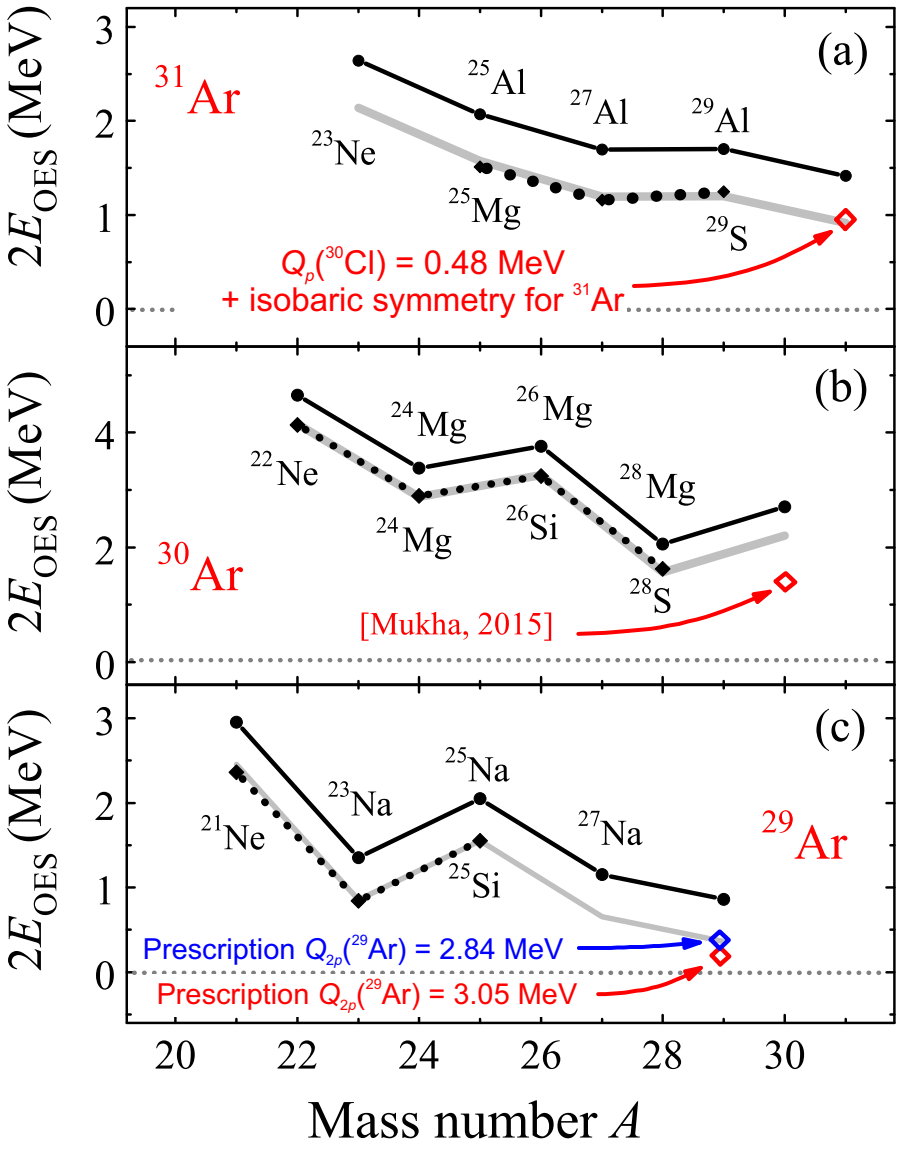

Figure 5.1: Odd-even staggering energies $2E_{\mathrm{OES}} = S_{2N}^{(A)} - 2S_{N}^{(A-1)}$ in dependence of mass number A. The trends for the isotonic chains leading to the $2E_{\mathrm{OES}}$ of ^{31,30,29}Ar are shown by dotted lines in panels (a),(b) and (c), respectively. The $2E_{\mathrm{OES}}$ values for the corresponding isobar mirror nuclei are shown by solid black lines, the values of separation energies are taken from the data base [21]. The red and blue diamonds in panel (a) and (c) are the calculations from this work, see the text for details. Panel (b) is taken from [46]. Solid gray lines are provided to guide the eye. The Figure is taken from [79] in modified form.

Chapter 6

First observation and spectroscopy of ^{31}K

The EXPERT pilot experiment resulted in one more remarkable observation, namely the most remote isotope from the proton dripline: the new isotope ^{31}K. It is located 4 mass units beyond the dripline and is unbound with respect to three-proton ($3p$) emission. The $3p$ decay of ^{31}K has been detected using the in-flight decay technique by measuring the trajectories of all decay products, using silicon microstrip detectors, see Subsection 2.6.3 for the method details. The following reactions leading to the production and decay of ^{31}K have been examined:

$$^{36}\mathrm{Ar} \xrightarrow{\text{fragmentation}} {}^{31}\mathrm{Ar} \xrightarrow{\text{charge exchange}} \mathbf{^{31}K} \xrightarrow{\text{3-proton decay}} {}^{28}\mathrm{S} + p + p + p \qquad (6.1)$$

The isotope of interest, ^{31}K, was produced in a (n, p) charge-exchange reaction of ^{31}Ar in the secondary target. In the simplest consideration, such a charge-exchange reaction proceeds as follows: a neutron in the $d_{5/2}$ shell of ^{31}Ar transforms into a proton in the $d_{3/2}$ shell of ^{31}K while all the other nucleons remain undisturbed. Such a process has typically a factor of 10 - 20 lower production cross-section than neutron knock-out reactions which populate the ^{30,29}Ar isotopes. Nevertheless, the obtained data allow for the analysis of the angular correlation between heavy decay product ^{28}S and three protons. The data analysis and the obtained spectroscopic information are described in this Chapter. The results have been published in [78].

The components of the fourfold-coincidence events, namely ^{28}S + $3p$, were obtained in the same manner as the triple-coincidence events for the ^{29,31}Ar studies, S + $2p$. The analysis steps for the HI and proton identification and tracking can be found in Chapter 4. The trajectories of the measured ^{28}S + $2p$ coincidence events set the basis for the discovery and spectroscopy of the isotope ^{30}Ar [46, 86, 106], which can be considered as a decay sub-system of ^{31}K.

6.1 Angular correlation of ^{31}K decay products

In analogy to $2p$ decays, the three decay protons of ^{31}K share the total decay energy. Then a r.m.s. relative angle variable ρ_θ, see Eq. 4.8, can be used for further analysis. In this case, the quantity is $\rho_\theta(^{28}\mathrm{S} + p + p + p)$ or ρ_3 in short, and the relation should be modified accordingly:

$$\rho_3 = \sqrt{\theta^2_{p_1\text{-}^{28}\mathrm{S}} + \theta^2_{p_2\text{-}^{28}\mathrm{S}} + \theta^2_{p_3\text{-}^{28}\mathrm{S}}}, \qquad (6.2)$$

where ρ_3 is the r.m.s. angle derived from the measured trajectories of ^{28}S and the three protons in coincidence. The distribution of the kinematic variable ρ_3, reflecting the total decay energy of ^{31}K, is shown in Fig. 6.1. One can see three well-separated peaks, labeled (i) – (iii), which are assumed to reflect the population of three states in ^{31}K. The estimated $3p$-decay energies Q_{3p}, taken from the calibration on argon isotopes, are shown on the upper axis of Fig. 6.1. The peak (i) corresponds to the total energy

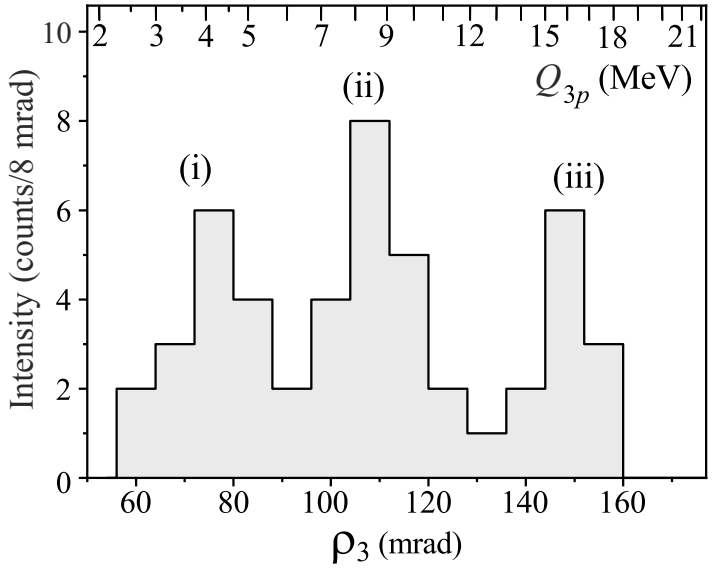

Figure 6.1: Three-proton angular correlation reflected by the distribution of the root-mean-square variable ρ_3. Three peaks (i) – (iii) point to separate states in the energy spectrum of ^{31}K. The corresponding $3p$-decay energies Q_{3p} are shown on the upper axis.

of about 4.5 MeV, peaks (ii) and (iii) correspond to energies of about 9 and 16 MeV, respectively. The state (i) may be interpreted as a ground state of ^{31}K, and (ii), (iii) as the excited states of this isotope. By gating on each peak in the ρ_3 distribution, one can select states in ^{31}K and obtain the energies of protons that contribute to them. The projections of each selected group of events on the $\theta_{p\text{-}^{28}\mathrm{S}}$ axis are displayed in the histograms in panels (i), (ii) and (iii) of Fig. 6.2, respectively.

Let us inspect the angular distribution at the panel (i) in Fig. 6.2. The projection here is assumed to be contributed from the g.s. of ^{31}K with the total decay energy around 4.5 MeV. The two peak-like structures with Q_p of about 1.2 and 2.2 MeV point to the sequential decay mechanism of this state. The broad peak at 1.2 MeV is very similar to the contribution of two protons coming from the known $2p$ decay of ^{30}Ar g.s. with $Q_{2p} = 2.45(15)$ MeV [86]. Then the peak at 2.2 MeV should correspond to a $1p$ emission from ^{31}K g.s. to the g.s. of ^{30}Ar. These two preliminary decay-energy assignments require detailed Monte-Carlo simulations of the detector setup response. It has been performed using the procedure described in Subsection 4.2.2. Thus, two angular contributions in the data have been fitted separately by the two respective components: 1) the Monte-Carlo simulation including the experimental setup response to $1p$ emission of ^{31}K, see solid red curve in Fig. 6.2(i); 2) the known detector response to the $2p$ decay of the ^{30}Ar g.s., see [86], shown by the dotted blue curve in the same Figure. The small-angle region of the $\theta_{p-^{28}\mathrm{S}}$ distribution agrees with the $2p$ decay of

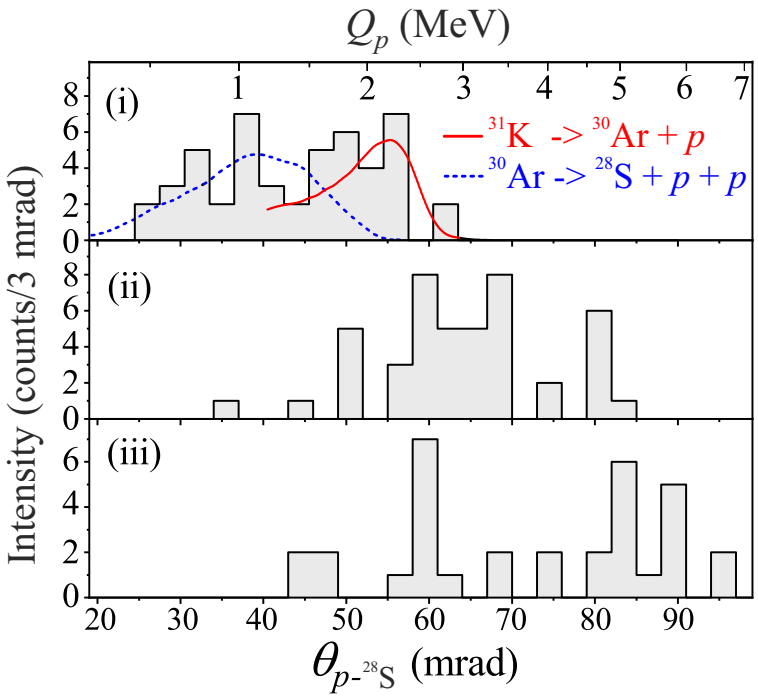

Figure 6.2: Angular $\theta_{p-^{28}S}$ correlation projected from the measured ^{28}S+p+p+p coincidences. The data in panels (i), (ii), (iii) are selected by the respective gates around the ρ_3-peaks in Fig. 6.1. The corresponding 1p-decay energies Q_p are given in the upper axis. Panel (i): the solid red curve is the simulation of the initial 1p-decay of ^{31}K to the ^{30}Ar g.s. with the fitted decay energy of 2.15(15) MeV. The contribution of a subsequent 2p decay of ^{30}Ar with the known energy of 2.45 MeV [86] is shown by the dotted blue curve.

^{30}Ar g.s. (the dotted red line accounts for the literature value of the 2p-decay energy of $2.45^{+0.05}_{-0.10}$ MeV), while the large-angle correlation can be described by the 1p emission of ^{31}K to the ^{30}Ar g.s. (solid blue line) with the decay energy of 2.15(15) MeV. The fitting procedure is based on the maximum-likelihood method explained above for the example of ^{29}Ar 2p decay, see Fig. 4.12 of Subsection 4.2.2. Finally, the 3p-decay energy of the ^{31}K g.s. may be assigned as $2.15(15)+2.45^{+0.05}_{-0.10} \simeq 4.6(2)$ MeV.

Similar angular $\theta_{p-^{28}S}$ projections with gates on the peaks (ii) and (iii), see Fig. 6.2, are more difficult to interpret because no pronounced structures are seen here and the statistics is low. This situation may be improved in future experiments. It should be noted, however, that both distributions in panels (ii) and (iii) contain no contribution from the 2p decay of the ^{30}Ar g.s., and therefore the 9 and 16 MeV excited states in ^{31}K should decay also via excited states in ^{30}Ar. All the assigned states and decay branches are summarized in the level scheme of ^{31}K, see Fig. 6.3.

6.2 Comparison of the measured 3p-decay energy with theoretical predictions

The assigned 3p-decay energy of the ^{31}K g.s., $Q_{3p} = 4.6(2)$ MeV, may be compared with theoretical predictions. In analogy with 1p- and 2p- separation energies from Eqs. 1.1

and 1.2 of Chapter 1, the $3p$ separation energy can be written as

$$\begin{aligned} S_{3p}(N,Z) &= B(N,Z) - B(N,Z-3), \\ S_{3p}(^{31}\mathrm{K}) &= B(^{31}\mathrm{K}) - B(^{28}\mathrm{S}). \end{aligned} \tag{6.3}$$

The S_{3p} value is estimated by using the predicted binding energy $B(^{31}\mathrm{K})$ from the improved Kelson-Garvey mass relations for neutron-deficient nuclei [122] and the literature value of $B(^{28}\mathrm{S})$ from [21]. This gives $S_{3p}(^{31}\mathrm{K})$ = -7.0 MeV, see the corresponding Q_{3p} value on the right-hand side of the level scheme in Fig. 6.3. The latter disagrees with the measured experimental value, and the mismatch here may be explained by the Thomas-Ehrman shift effect in ^{31}K isotope. The TES contribution is not included in the Kelson-Garvey predictions.

Alternatively, as the ^{31}K g.s. decays via the long-lived ^{30}Ar g.s., the empirical S_p systematics of $1p$-emitting states in light nuclei, based on a parametrization of experimental mirror energy differences (MED) [123], may be used. According to [123],

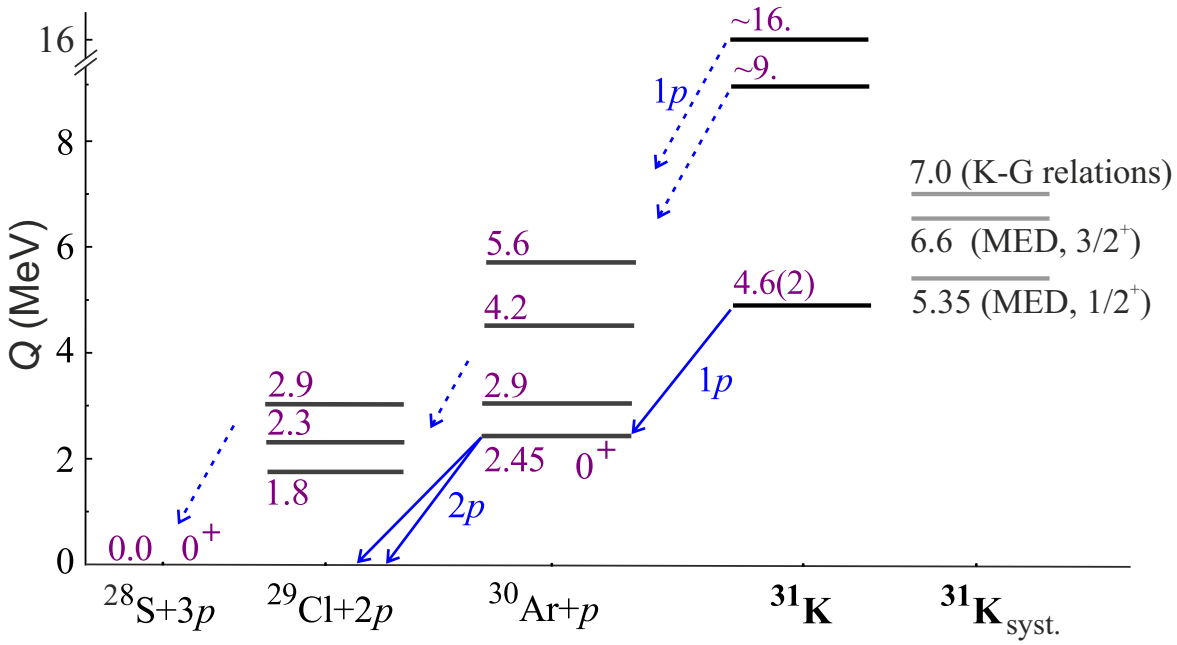

Figure 6.3: Decay scheme of ^{31}K levels with a tentatively-assigned $1p$-decay sequence through the known ^{30}Ar and ^{29}Cl states [86], see solid arrows. The dashed arrows indicate unidentified transitions. The decay energies E are given with respect to the ^{28}S + $3p$ energy threshold. On the right-hand side, labeled $^{31}\mathrm{K}_{\mathrm{syst.}}$, the energies of the ^{31}K g.s. predicted by different systematics are shown by solid gray lines: they result from the improved Kelson-Garvey mass relations (K-G relations) from [122], and the energy estimates of the ^{31}K g.s. based on mirror energy differences (MED) [123] assuming the spin-parity of $3/2^+$ or $1/2^+$.

the MED is defined as:

$$\begin{aligned} \mathrm{MED} &= S_n - S_p, \\ \mathrm{MED} &= \frac{Z}{A^{1/3}}\mathrm{MED}', \end{aligned} \tag{6.4}$$

where S_n is the neutron-separation energy of the neutron-rich isobaric mirror partner of the neutron-deficient nucleus with S_p, Z is the atomic number of the proton-rich nucleus, MED′ is the component of MED independent on A and Z.

The recipe to calculate S_{3p} of ^{31}K using MEDs is the following: 1) the MED′ is calculated using the known separation energies of the (A-2) mirror pair ^{29}Cl – ^{29}Mg [21]; 2) $S_p(^{31}\mathrm{K})$ is then calculated using the known S_n of isobaric-mirror partner ^{31}Mg from [21] and the above calculated MED′; 3) $S_{3p}(^{31}\mathrm{K})$ is estimated as $S_p(^{31}\mathrm{K})$ plus the $S_{2p}(^{30}\mathrm{Ar})$ from [86].

The spin-parity of the ^{31}K g.s. cannot be estimated from the measured data. Two possible options are considered, namely $3/2^+$ or $1/2^+$ based on the spin-parity of ^{31}Mg. The spin-parity of the ^{31}Mg g.s. is $1/2^+$, but the first excited state is separated from the g.s. by only 50 keV [124]. In addition, the level inversion is observed for the g.s. of the ^{29}Cl – ^{29}Mg pair, so both $3/2^+$ and $1/2^+$ assignments are assumed. The MED calculation using the $^{29}\mathrm{Cl}^*(3/2^+)$ – $^{29}\mathrm{Mg}_{\mathrm{g.s.}}(3/2^+)$ mirror pair gives $S_{3p}(^{31}\mathrm{K})$ = -6.6 MeV. This disagrees with the measured data. The next option is to use the separation energies for the $^{29}\mathrm{Cl}_{\mathrm{g.s.}}(1/2^+)$ – $^{29}\mathrm{Mg}^*(1/2^+)$ pair, taking into account the measured excitation energy of 55 keV for the $^{29}\mathrm{Mg}^*(1/2^+)$ [125]. The latter results in $S_{3p}(^{31}\mathrm{K})$ = -5.35 MeV. The calculated MEDs for both options of the g.s. spin-parity do not agree with the measured value[1], see Fig. 6.3, thus further theoretical investigations of this matter are required.

6.3 Half-life measurement based on decay-vertex reconstruction

As stated in Subsection 2.6.3, an important feature of the in-flight decay technique is the possibility to measure the decay vertex distribution. This allows for the evaluation of the half-life $T_{1/2}$ of the decaying isotope. As a reference, the profile of $2p$ decay vertices of the $^{30}\mathrm{Ar}^*$ short-lived excited states is shown in Fig. 6.4 (a). The latter was obtained in the same experiment under the same conditions using the measured ^{28}S+p+p trajectories [46]. The vertex profiles of the tentatively assigned ground and first excited states of ^{31}K are shown in Fig. 6.4 (b) and (c), respectively. The latter profiles are obtained from the measured ^{28}S+p+p+p trajectories and the applied gates on (i) and (ii) peaks in the ρ_3 spectrum from Fig. 6.1.

The Monte Carlo simulations for the reference case of short-lived excited states of ^{30}Ar are shown in Fig. 6.4 (a). The half-live of the $^{30}\mathrm{Ar}^*$ state is set to $T_{1/2}$ = 0.001 ps (or $\simeq$ 0 ps) in the simulation, see the solid black curve. The experimental angular uncertainties in the tracking of fragments, and reconstructing the decay vertex coordinates are also taken into account, see Subsection 4.1.4 for the details. The simulations reproduce the data quantitatively. The half-life uncertainty is illustrated by the $T_{1/2}$ = 5 ps simulation, which fails to fit the data, see the dotted blue curve. The asymmetry of the rising and falling slopes of the vertices is due to the multiple scattering of the fragments in the thick target, see Fig. 2.7 of Chapter 2 for the detailed explanation of the profile shape. Similar Monte Carlo simulations with $T_{1/2}$ of $\simeq$ 0, 5 and 10 ps have been performed for the ^{31}K states, and compared with the corresponding data in Fig. 6.4 (b). The simulation with $T_{1/2}$ = 5 ps represents the ^{31}K g.s. data the best. By using a maximum-likelihood fitting procedure like the one applied for the decay energy determination, the following probabilities P that the simulated setup response

[1]In this work, the ^{31}K isotope is considered to have a single-particle configuration. Its mirror nucleus ^{31}Mg exhibits a complicated shape-coexistence structure and ground state deformations [124], which are not taken into account in the presented estimates.

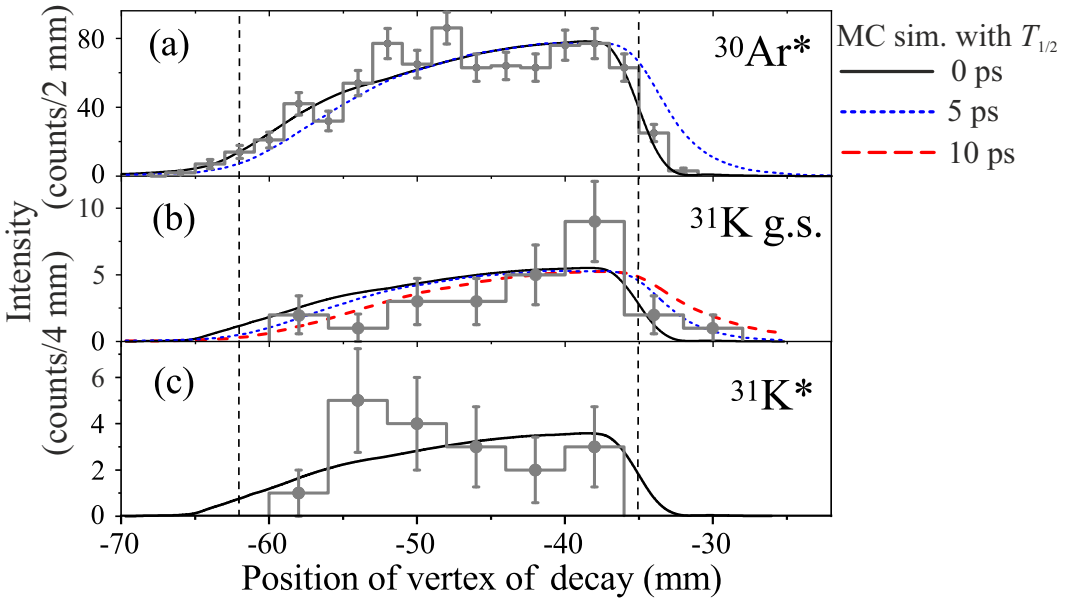

Figure 6.4: Panel (a): profile of the measured ^{30}Ar* $\rightarrow^{28}$S+p+p decay vertices along the beam direction with respect to the first microstrip detector D0, see setup details in Section 3.2. The data correspond to short-lived excited states in ^{30}Ar* [46]. Panels (b,c): profiles of the ^{31}K$\rightarrow^{28}$S+p+p+p decay vertices measured under the same conditions as those shown in panel (a). The data shown in (b) is gated by the peak (i) in Fig. 6.1, which corresponds to the g.s. of ^{31}K. The data shown in (c) is gated by the peak (ii) in Fig. 6.1, which corresponds to a short-lived excited state in ^{31}K. The solid, dotted, and dashed curves show the results of Monte Carlo simulations which include the detector setup response for the 2p decays of ^{30}Ar and 3p decays of ^{31}K with half-lives $T_{1/2}$ of 0, 5 and 10 ps, respectively. The target position is indicated by vertical dashed lines. The D0 detector is located at the origin of this drawing.

matches the experimental vertex distribution were obtained: $P = 0.93$ for the half-life of the ^{31}K g.s. of 0 ps, $P = 0.98$ for the one of 5 ps, and $P = 0.6$ for one of 10 ps. Thus the half-life value of the ^{31}K g.s. shorter than 10 ps can be concluded, which is the upper-limit estimate. For the ^{31}K excited-state, the simulation of the vertex profile is shown in Fig. 6.4 (c) giving $T_{1/2} \simeq 0$ ps. It should be mentioned that the Lorentz factor of ^{31}K is about 1.6, thus the lifetimes are extracted including relativistic effects.

The discovery and the first spectroscopy of the ^{31}K isotope is an important step towards the investigation of nuclear structure far beyond the dripline. As stated above, the ^{31}K is so far the most-remote experimentally-observed isotope, namely, 4 mass units beyond the proton dripline[2]. The obtained upper-limit estimates of ^{31}K states are in the order of ps or lower. However, these values are still much longer than the ones predicted for "last" isotopes (with the widths close to or exceeding 3 - 5 MeV) located on the limits on the existence of nuclear structure [2], see also Chapter 1. Thus, the existence of even more remote from the proton dripline isotopes of potassium is possible, and the transition to amorphous nuclear matter has not yet been reached.

[2]Another extensively studied isotopic chain belongs to fluorine. Its last observed nucleus is ^{14}F, which is 3 mass units beyond the proton dripline [126]. Also, one more 3p emitter, ^{17}Na, has been observed recently [127]. No spectroscopic information for this isotope was obtained, but the upper limit on its mass was established. The ^{17}Na nucleus is also 3 mass units beyond the dripline.

Chapter 7

In-flight decay studies with high-resolution momentum measurements of heavy decay products

In this Chapter, the possibility to derive the proton decay energy by measuring the longitudinal momentum distribution of the heavy projectile-like decay products is studied. This approach can complement the in-flight decay technique investigating isotopes with sub-μs lifetimes. For the sake of a systematic study, Section 7.3 is devoted to a simple kinematic case. In Section 7.4 the momentum measurement is studied for the case of a real detector setup of the EXPERT pilot experiment (see Chapter 3). The simulations have been performed with the GEANT4 framework integrated into the R3BRoot software [128, 109] with the following example:

- in-flight decay of ^{30}Cl $\rightarrow$ ^{29}S + p,
- kinetic energy of mother nucleus ^{30}Cl is $T(^{30}\mathrm{Cl}) = 18.54$ GeV,
- the assumed decay energy of the mother nucleus $Q = 2$ MeV.

This case of one-proton emission was experimentally observed during the EXPERT pilot experiment, see the details in Chapters 3 and 4.

7.1 Motivation and principal concept

One of the key features of the FRS [3] and Super-FRS fragment separators [5, 129, 130] is the measurement of the momenta of fragmentation products with high-resolution. The momentum resolving power $p/\Delta p \approx 1500$ for an emittance of 40 π mm mrad is required to reach a mono-isotopic separation of secondary beams. The Super-FRS has a larger phase-space acceptance of $\pm$2.5% than the FRS ($\pm$1% acceptance with the same resolving power) and an additional pre-separation stage. This makes the Super-FRS a unique and flexible facility. An idea of efficient utilization of the high-resolution momentum measurement option together with unambiguous heavy ion identification is proposed to supplement the in-flight proton-emission experiments. The determination of the decay energy from the measured longitudinal momentum of the heavy decay fragment is described below.

Proton-emitting precursors are formed in high-energy fragmentation reactions. Their decay products follow trajectories in forward direction in the laboratory frame. In the considered case, the $T(^{30}\mathrm{Cl}) >> Q_p$ condition is also fulfilled. The heavy ion ^{29}S, denoted as HI in this Chapter, continues the direction of travel of the mother nucleus ^{30}Cl with only minimal trajectory deviation of less than a mrad. Because of this, the scattering angle falls in the transverse acceptance of the separator and the momentum deviation of the HI falls into the ±2.5% acceptance of the Super-FRS. So that the HI can be identified by the standard Super-FRS detectors located at a downstream focal plane. Its longitudinal momentum is measured at the dispersive focal plane. The corresponding proton momentum can not be directly derived in most cases, because it is emitted at a relatively large angle beyond the ion-optical acceptance of the separator.

7.2 Invariant mass calculation

One of the approaches to the decay energy determination of a very short-lived system (with life time less than 10^{-19} s) is the invariant mass method, see Subsection 2.6.1. Then one can calculate the decay energy using the following equation

$$Q = \frac{4(M\vec{p}^{\,*})^2}{(M + m_p - m_{\mathrm{HI}})(M - m_p + m_{\mathrm{HI}})(M + m_p + m_{\mathrm{HI}})c^2}, \tag{7.1}$$

where M is the mass of mother nucleus, m_p is the mass of proton, m_{HI} is the mass of HI, $\vec{p}^{\,*}$ is the 3-momentum vector of the decay product in the c.m.s. frame. The derivation of Eq. 7.1 can be found in Chapter 2, Eq. 2.5. The $\vec{p}^{\,*}$ can be calculated from the components of the three-momentum vector in the laboratory system $\vec{p}$, see Lorentz transformations in Eqs. 2.8 of Chapter 2. The calculated decay energy Q of ^{30}Cl obtained by Eq. 7.1 with a simulated $\vec{p}$ of the proton is shown in Fig. 7.1. The histogram exhibits a very narrow peak centered at $Q = 2$ MeV with a standard deviation of about 2 keV, it is an ideal case with high statistics of 10^5 events.

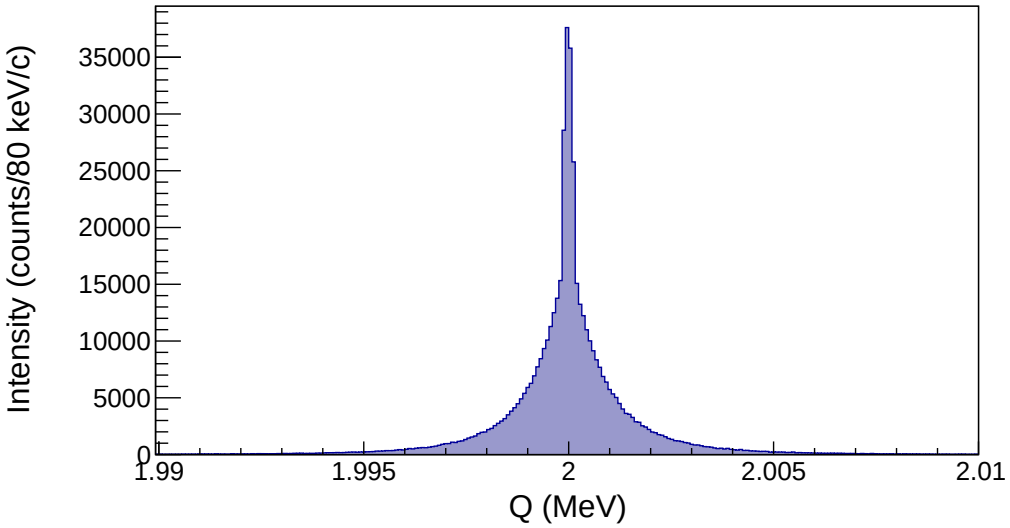

Figure 7.1: Decay energy $Q = 2$ MeV of ^{30}Cl, calculated by using the invariant mass method with the momentum $\vec{p}$ of the proton.

In a real experiment, it is very challenging to measure all three momentum components of the proton. This task requires a specific detector setup in addition to the spectrometer. Thus, one of the goals of this Chapter is to find an approach to efficiently measure the decay energy without additional devices.

7.3 Kinematics

In experiments at separator facilities, the longitudinal momentum distribution $\vec{p}_{||}$ of the charged fragments is measured. In the present case, see reaction conditions in Sec.7.1, one considers the longitudinal momentum $\vec{p}_{||}$ of the HI from the proton decay. In the current calculation, the kinematics of the decay reaction is taken into account.

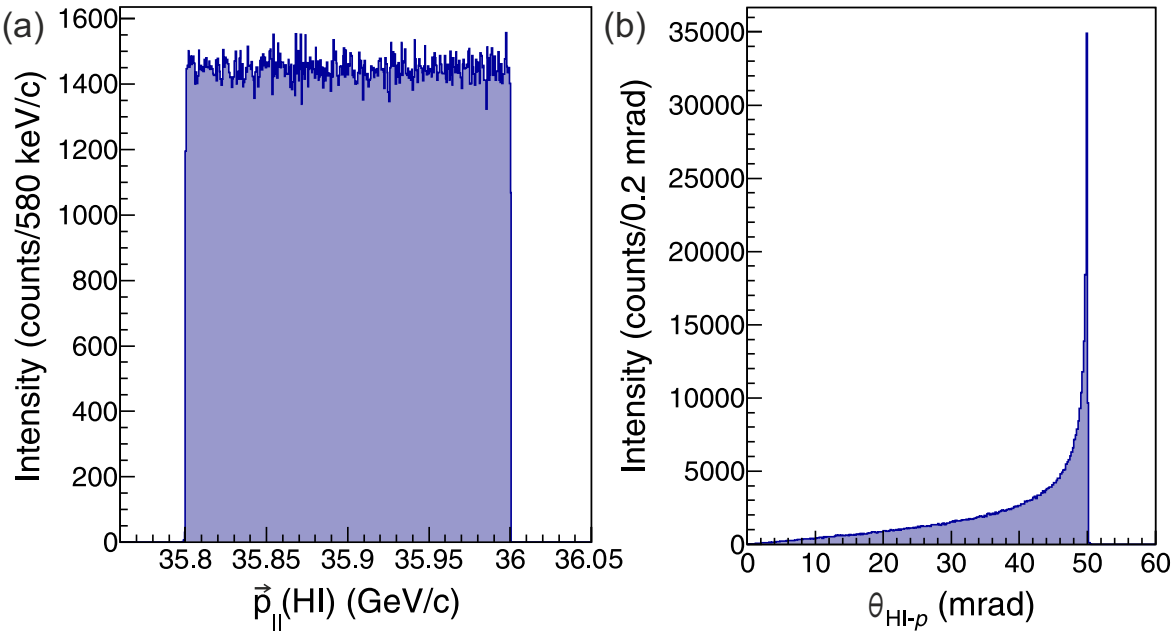

Figure 7.2: Panel (a): distribution of the longitudinal momentum $\vec{p}_{||}$(HI) of a heavy ion. Panel (b): relative angle between proton and HI.

The calculated distribution of $\vec{p}_{||}$(HI) is shown in Fig. 7.2(a). This distribution has a uniform shape and sharp edges, which is explained by the kinematic limits of the decay. To understand the origin of those limits, the relative angle $\theta_{\mathrm{HI}-p}$ between proton and HI is considered, see Fig. 7.2(b). As mentioned in Sec.7.1, a proton is emitted at a certain angle with respect to the direction of the HI. The relative angle distribution exhibits a narrow peak close to the maximum value (about 50 mrad in the considered case). The description of the shape of such angular distribution is derived in Chapter 2, see Eq. 2.29.

The relative angle $\theta_{\mathrm{HI}-p}$ depends on the direction of proton emission in the rest frame of the mother nucleus (or the c.m.s. frame). A cartoon, illustrating this effect, and the correlation between the relative angle and $\vec{p}_{||}$(HI) from the calculation are shown in Fig. 7.3, left and right panels, respectively. On the left panel in Fig. 7.3, one can see three extreme, but representative scenarios (a) – (c) of proton emission in the rest frame of the mother nucleus. In case (a), the proton is emitted in backward

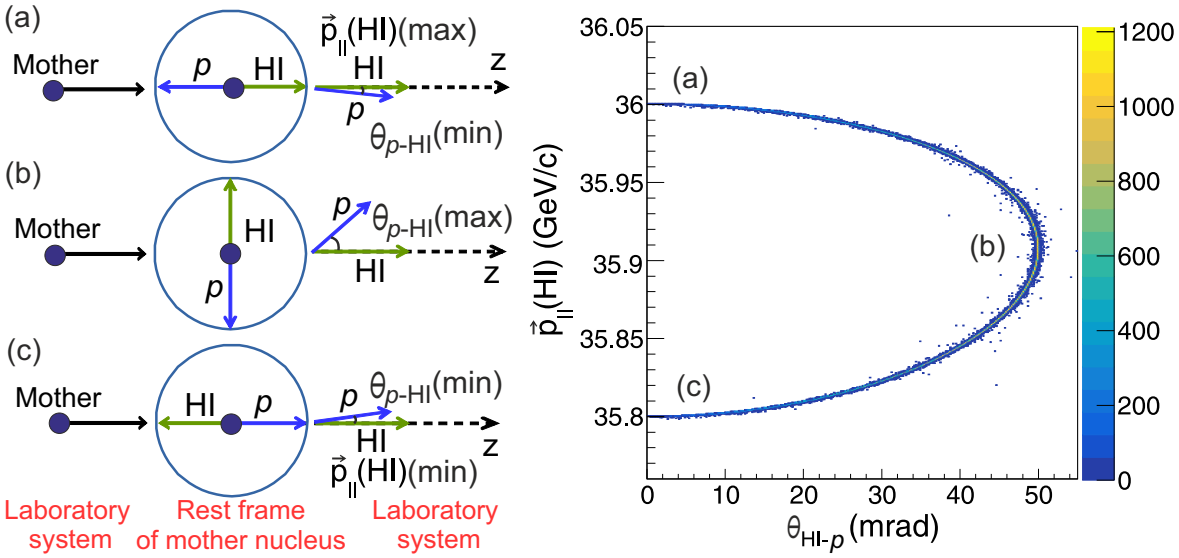

Figure 7.3: Left panel: three kinematic scenarios (a), (b), and (c) for one-proton emission from a high-energy mother nucleus. In the laboratory system, the relative angle $\theta_{\mathrm{HI}-p}$ depends on the direction of proton emission in the rest frame, see detailed explanation in the text. Right panel: two-dimensional correlation plot between $\theta_{\mathrm{HI}-p}$ and $\vec{p}_{||}(\mathrm{HI})$ from calculation. The areas corresponding to a particular emission case are also marked (a) – (c). The color code represents the number of events.

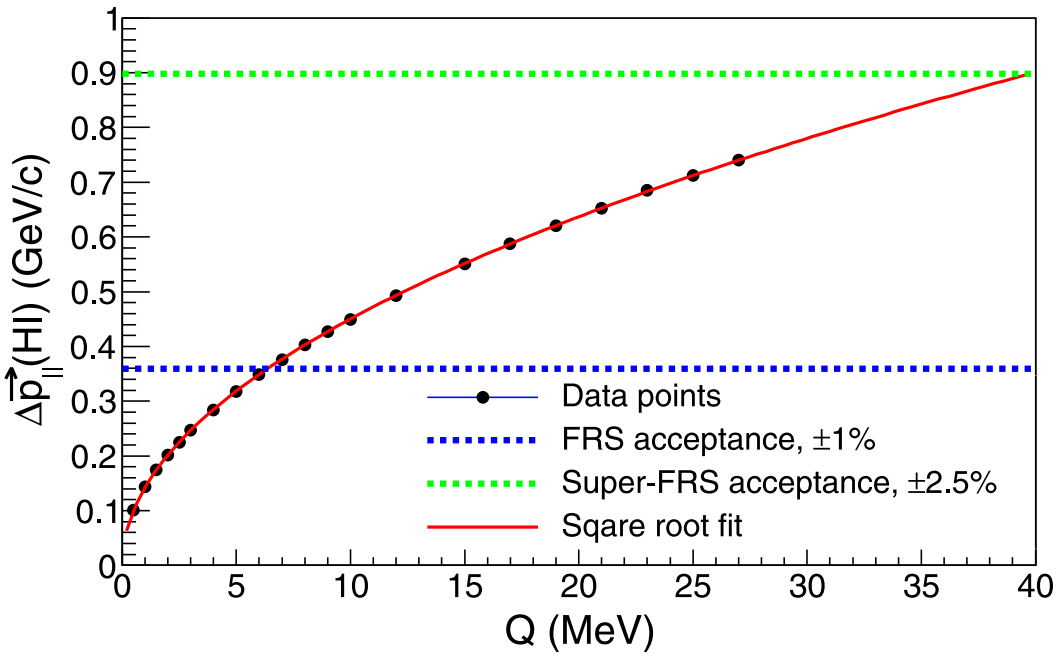

Figure 7.4: Range of longitudinal momentum $\Delta\vec{p}_{||}(\mathrm{HI})$, defined by $\vec{p}_{||}(\mathrm{HI})(\mathrm{max}) - \vec{p}_{||}(\mathrm{HI})(\mathrm{min})$, as a function of the decay energy Q in the pure kinematic case. Black points represent the calculation results for different energies. The square root fit is shown by the red curve. The momentum acceptances of the FRS and the Super-FRS are shown by the blue and green dashed lines, respectively.

direction in the rest frame, thus the HI gets maximum possible momentum $\vec{p}_{||}$(HI) in forward direction. In the laboratory frame, the proton is found at zero angle $\theta_{\mathrm{HI}-p}$ relative to the trajectory of HI. In reality the trajectories form a narrow cone. Case (b) presents the situation, when HI and proton are emitted orthogonally to the beam axis. The $\theta_{\mathrm{HI}-p}$ is reaching its maximum value in the laboratory frame. This is the most probable scenario. The third case (c) is the reversed case (a): HI has the minimum possible momentum in the lab, and the relative angle is also minimal. The right panel in Fig. 7.3 shows the simulated correlation between $\theta_{\mathrm{HI}-p}$ and $\vec{p}_{||}$(HI), the areas belonging to different emission scenarios are labeled by (a) – (c) respectively to the left panel.

There is a clear dependence of the longitudinal momentum $\vec{p}_{||}$(HI) on the relative angle $\theta_{\mathrm{HI}-p}$. Does the dependence remain if one addresses the range of $\vec{p}_{||}$(HI) instead, namely the $\Delta\vec{p}_{||}(\mathrm{HI}) = \vec{p}_{||}(\mathrm{HI})(\mathrm{max}) - \vec{p}_{||}(\mathrm{HI})(\mathrm{min})$? The value of $\Delta\vec{p}_{||}$(HI) can be calculated from the measured longitudinal momenta if the HI remains within the separator acceptance. It is known, that the relative angle $\theta_{\mathrm{HI}-p}$ reflects the decay energy Q[1]. In order to understand the dependence of $\Delta\vec{p}_{||}$(HI) on Q, several calculations for different Q values were performed, see the resulting plot in Fig. 7.4. The dependence exactly follows a square root function, i.e., $\Delta\vec{p}_{||}(\mathrm{HI}) \sim \sqrt{Q}$ with fitted quadratic coefficients. This observation allows for the estimation of the decay energy by measuring the range of longitudinal momentum of HI with the FRS or Super-FRS in in-flight decay experiments.

7.4 Simulation results

The calculations, presented in the previous Section, show the square-root dependence between the range of heavy ion longitudinal momentum and the proton-emission energy. However, this effect was considered in a pure kinematic calculation without energy-loss, straggling, and detector response effects. Is this dependence preserved in real experiment conditions? To answer this, Monte-Carlo simulations of the setup response are performed. The setup is taken from the EXPERT pilot experiment, see Chapter 3 for details, and implemented into the simulation model. The screenshot from the simulation viewing tool with the implemented setup is shown in Fig. 7.5.

The setup consists of the secondary ^{9}Be target and an array of 4 silicon microstrip detectors (DSSDs), placed downstream from the target at a distance of 60 mm (1st DSSD pair) and 300 mm (2nd DSSD pair). The thickness of the target is 26 mm. Each of the detectors is 300 μm thick. As it is described in Subsection 2.6.3, the secondary targets used in the considered type of tracking experiments are usually thick to increase the production rate of the reaction products. This leads to the effects of multiple scattering and energy straggling of charged fragments inside the target. Such effects result in the degradation of the energy and position distributions. However, they can be compensated by the tracking all the decay products, see Chapter 4 with the analysis and tracking description. So far, the range of the longitudinal momentum distribution has not been considered yet.

In the approach described in this Section, it is an essential observable. To demonstrate this, the simulation of a one-proton emission reaction has been performed, considering the specified conditions (see the introduction to this Chapter) and the described-

[1]The $\theta_{\mathrm{HI}-p}$ depends on the decay energy value Q and is increasing with the increase of Q. The nature and utilization of this effect for spectroscopic measurements is described in Chapter 2.

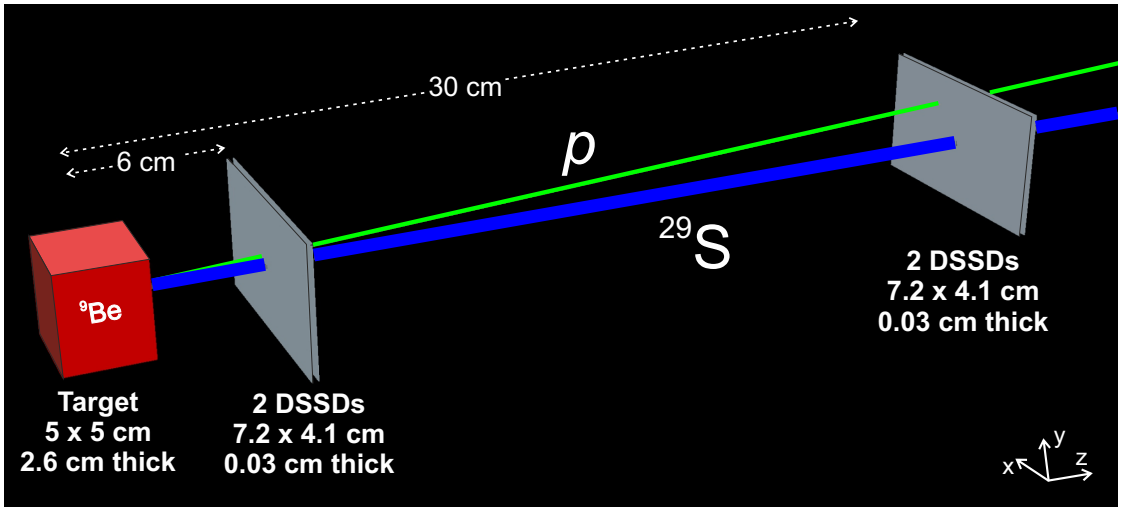

Figure 7.5: Visualization of the detector setup geometry implemented into the simulation. The thick ^{9}Be target is shown by red color, 4 silicon microstrip detectors (DSSDs) are shown by grey color. The trajectories of the decay products from one simulated decay event are shown by the blue and green lines for the heavy ion (^{29}S) and the proton (p), respectively.

above setup. The momentum distribution of heavy ions ^{29}S is strongly affected by the energy loss due to ionization (mostly in the thick beryllium target and also in the silicon detectors) because of their high atomic number ($Z = 16$). This results in a non-negligible change of the longitudinal momentum distribution, see Fig. 7.6 (a) (comparing to the case of the previous calculation shown in the left panel of the Fig. 7.2). Now

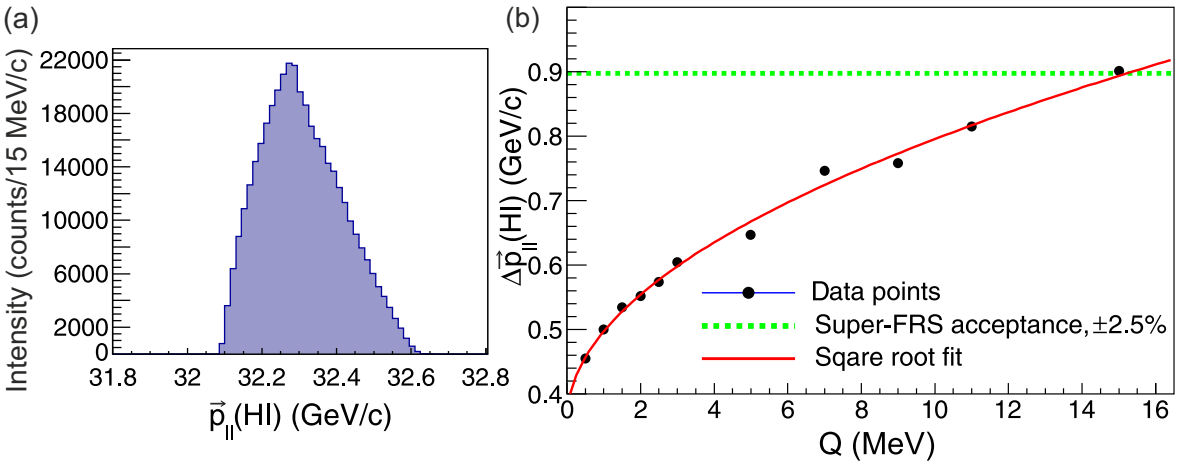

Figure 7.6: Panel (a): simulated distribution of the longitudinal momentum $\vec{p}_{||}$(HI) of ^{29}S, the heavy decay product of ^{30}Cl. Panel (b): range $\Delta\vec{p}_{||}$(HI) of the longitudinal momentum in dependence of the decay energy of ^{30}Cl. The momentum acceptance of the Super-FRS, calculated using the mean value of longitudinal momentum from panel (a), is shown by the green dashed line. The red curve is a square root fit function to the data points. The simulations are performed taking into account the interactions with matter, detector response and separator acceptance.

the shape of the distribution exhibits two components: a fast-growing one (comparable to the edge of uniform distribution for the pure kinematics case) and a slow-decreasing one. Nevertheless, the dependence of the momentum range on the decay energy preserves the square root shape, see Fig. 7.6 (b), like in the kinematic case shown in Fig. 7.4. It should be noted, however, that such a measurement can be performed only at the Super-FRS because its momentum acceptance of ± 2.5% covers the larger scope of the decay energies (up to 15 MeV, see Fig. 7.6 (b)) than the acceptance of the FRS.

7.5 Determination of the decay energy from momentum measurements

The separator can measure the longitudinal momentum of the ion very accurately and precisely, namely with the resolution of 0.025% if the resolving power of 4000 is considered (the value of the resolving power is taken as the one from the EXPERT pilot experiment, see Chapter 3). However, the largest (decisive) impact on the precise determination of the decay energy comes from the statistical error of the momentum range measurement. In this Section it is investigated what is the minimal number of measured events required to obtain an accurate value of the momentum range $\Delta\vec{p}_{||}$(HI), and what is the uncertainty of the decay energy determination, when both the statistical error of the range measurement and the separator resolution are considered? To understand this, the momentum range dependence on the number of events is calculated. The result for both, kinematic and realistic case, can be seen in Fig. 7.7 (a) and (b), respectively. The standard deviation shown in Fig. 7.7 by red error bars for the $\Delta\vec{p}_{||}$(HI) was calculated using the following standard formula

$$\delta(\Delta p) = \sqrt{\frac{1}{N-1}\sum_{i=0}^{N}(\Delta p_i - \langle\Delta p\rangle)^2}, \tag{7.2}$$

where Δp_i is the range of $\vec{p}_{||}$ of HI measured in each i-th simulation run, $\langle\Delta p\rangle$ is the mean value of $\Delta\vec{p}_{||}$, N is the number or runs. This deviation reflects the statistical error, which is dependent on the number of events measured and decreases with the increase of statistics. Also, with the increase of the event number, the mean range is approaching its maximum possible value, shown by the blue vertical line in both panels of Fig. 7.7. The maximum value of $\Delta\vec{p}_{||}$(HI), calculated in the simulation run with 10^6 events, is equal to the square root of the decay energy.

The statistical error of the range of longitudinal momentum has a decisive impact on the precise decay energy determination. However, as stated above, the statistical error decreases with the number of events measured. At some point, its value approaches the value of separators resolution. This is illustrated in Fig. 7.8, calculation is performed for the realistic case. The resolution of the separator is independent of the number of events recorded. The error it brings to the momentum range measurement is shown by black points. An absolute value of it is calculated from the errors of the direct measurement of a minimum and maximum value of the longitudinal momenta, $\vec{p}_{||}$(HI)(max) and $\vec{p}_{||}$(HI)(min), with 0.025% resolution. The statistical error (standard deviation calculated using Eq. 7.2, also shown in Fig. 7.7(b) in red) is shown by red points. The statistical error and the one determined by the resolution have close to equal values when the number of measured events is about 600. In this case, one can

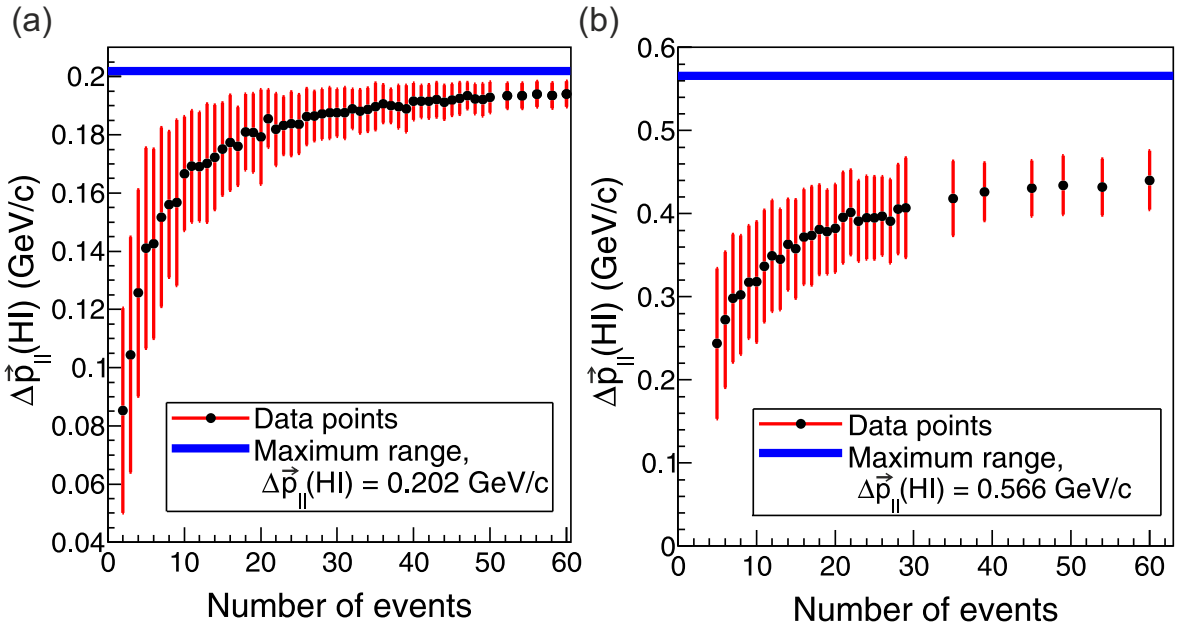

Figure 7.7: Panel (a): range of the longitudinal momentum distribution of the heavy ion ^{29}S in dependence on the number of events. The simulation considers only two-body decay kinematics. Panel (b): range of the longitudinal momentum distribution of the HI for different number of events, simulated including the F2 matter. In both cases on panels (a) and (b), for each number of events, the simulation is run 100 times to obtain the statistical uncertainty. The blue horizontal lines represent the maximum possible $\Delta\vec{p}_{||}$(HI), calculated for the chosen reaction and precursor energy.

estimate the relative error of the decay energy to be around 9% or $Q = 2.00(18)$ MeV. If more statistics (event number > 600) are obtained, the relative error of the decay energy determined by the range of longitudinal momentum of heavy ion is contributed mostly by the separator resolution, and thus can go down to 6%. This value of energy resolution is comparable with the one obtained by the angular measurement of the in-flight decay technique. Thus, the measurement of the momentum range can be used for an independent verification of the obtained spectroscopic information. It should be noted, however, that the proposed measurement can be achieved only via utilizing a dispersion-matched mode of the separator [131]. In this case, the incident momentum spread of the heavy ions is not contributing to the magnetic rigidity measurement via position at the final focal plane.

Additionally, one can estimate an impact of accurate longitudinal momentum measurement of heavy on the decay energy determination if used together with information of angular correlation between decay products. A calculation of uncertainties combining the in-flight decay method with 1 mrad angular resolution and longitudinal momentum measurement with 0.025% resolution gives the uncertainty of the decay energy Q about 4%. An estimate is performed based on the Eq. 2.16 from Chapter 2. In this case, the energy resolution of 4% is contributed mostly by the angular method. Its resolution can be improved by using the tracking detectors with smaller pitch size. Namely, the possible upgrade of the silicon tracker are the ALPIDE pixel detectors, see Chapter 9 for details.

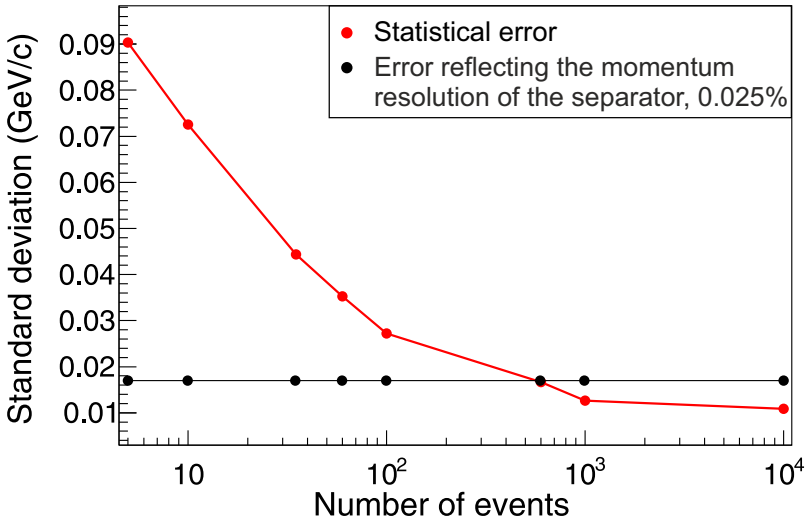

Figure 7.8: Standard deviation of the range of the longitudinal momentum of the heavy ion ^{29}S, calculated taking into account interactions with matter and detector response. The contributions of the statistical error and the error reflecting the separator resolution for the chosen case (0.025% for a resolving power of 4000) are shown by red and black points, respectively. The connecting lines are shown to guide the eye. The statistical error of the range measurement is decisive for a small number of events (below a few 100). It approaches the uncertainty given by the resolution of the separator and reaches a comparable value when the number of events is about 600.

In the real experiment, both complementary and standalone use of longitudinal momentum information can be utilized by performing calibration on the known proton emitter. For example, the measured range could be corrected with respect to its maximum possible value, which can be taken from the calibration. For that one can first measure a longitudinal momentum of a well-studied proton emitter, e.g., ^{15}F. Its proton-decay energy and the energy of the first excited state, are known with good precision of few keV [108]. Such a measurement could be a reference point. In the case of simultaneous utilization of longitudinal momentum and angular correlation information, the factor in Eq. 2.16, Chapter 2, can be also estimated from the known proton emitter.

7.6 Features of the method

The discussed method of obtaining the decay energy from the longitudinal momentum range measurement at fragment-separator/spectrometer facilities like the Super-FRS can have several advantages compared to (or utilized together with) the conventional in-flight tracking technique described in Chapters 3 and 4:

- The information on the longitudinal momenta of the heavy decay products comes from the magnetic rigidity measurement, which is always performed at the fragment-separators. This information comes complementary during the experiments with the EXPERT setup. Thus, it can be used for additional, independent verification and support of the obtained spectroscopic information.

- The described technique can be applied in a standalone mode, i.e., without the information on angular correlation, and provide an uncertainty of the decay energy of about 6%. This is comparable to the uncertainty of the in-flight decay method. Thus, the measurement of the range of longitudinal momentum provides a model-independent confirmation of the spectroscopic information obtained by the in-flight decay method. The proposed measurement is performed independently from the tracking. However, the absence of a silicon tracking array may allow for the use of secondary beams with higher intensities, which increases the obtained statistics. The maximum possible rate for silicon detectors is 2.5 kHz, see Subsection 3.2.1. It should be noted that, in a standalone mode, the proposed method is suitable only for measurements of the decaying nuclei in high-energy fragmentation reactions, where one precursor state is well-populated compared to the other states. Another constrain can be the distinction between a heavy ion from the decay and the other fragmentation products. Nevertheless, the standalone application can be a subject of further consideration.
- The technique can be used for the measurement of the decay energies of nuclei with the lifetime values in the intermediate range between what in-flight tracking (ps) and OTPC (ms and up) can measure. For example, the ^{72}Rb half-life was deduced assuming the yield systematics, namely $T_{1/2}(^{72}\mathrm{Rb}) = 103(22)$ ns was set [132]. On the basis of this measurement, the proton decay energy was indirectly derived to be $Q_p = 700 - 900$ keV for ^{72}Rb. The described method provides a complementary and direct way of decay energy determination, which is independent to the mechanism of proton emission.
- As a possible application, the measurement of the longitudinal momentum of the heavy ion from the neutron-emission process can be carried out. This could be done without the direct registration of the neutrons, which requires an additional detector setup and thus imposes new challenges in the experiment.

Chapter 8

Development and test of next generation EXPERT detectors

This Chapter is introducing the recently-performed developments of the EXPERT setup detectors. Namely, the properties of the NeuRad and silicon Time-of-Flight detectors, as well as their beam and laboratory tests, are described.

8.1 NeuRad neutron detector

The NeuRad neutron detector (the name stands for the Neutron Radioactivity), aims at providing precise information on angular correlation between nuclear-decay neutrons. Like in the case of proton-radioactivity studied via in-flight decays, information on angular correlation is used to determine the decay energy of the precursor and to derive the corresponding lifetime of the exotic nuclei[1]. The heavy, charged decay products are planned to be measured by other detectors of the EXPERT setup. For example, NeuRad will be used in combination with an array of silicon microstrip detectors, see Chapter 3, which is responsible for tracking of a heavy charged fragment.

One of the requirements of the NeuRad detector is that the trajectories of neutrons have to be obtained with high angular resolution in the order of 0.1 - 0.2 mrad. Thus, it has to be highly-segmented: the NeuRad detector will be constructed from a large number of plastic scintillating fibers (about 10^4 units). Each fiber has a shape with a cross-section of 3×3 mm^2 and a length of 1 m. The total angular acceptance of the detector is 12 mrad. The latter is determined by the low transfer momentum of the decay with energies expected in the range of 0.1 – 100 keV. The scintillating fibers are then grouped into bundles of 256, see the picture of the NeuRad prototype in Fig. 8.1 (a). Each bundle is read out by two multi-anode photomultiplier tubes (PMTs), fixed at both ends of the prototype. During the experiments, NeuRad will be placed along the trajectories of nuclear-decay neutrons, see Fig. 8.1 (b). This is planned to provide both the reasonably large detection efficiency (at least 50 %) and position resolution for neutrons with energies about 200-800 MeV interacting with the fiber material, in particular, via elastic scattering: a recoil nucleus (proton) produces ionization track in the scintillation material followed by a light flash inside the fiber. The light emitted within the total-reflection angle travels to the photodetectors on both ends of the fiber, where it is converted into electrical signals by PMTs. The signals are

[1]Description of this technique for the proton emission reactions can be found in Chapter 2.

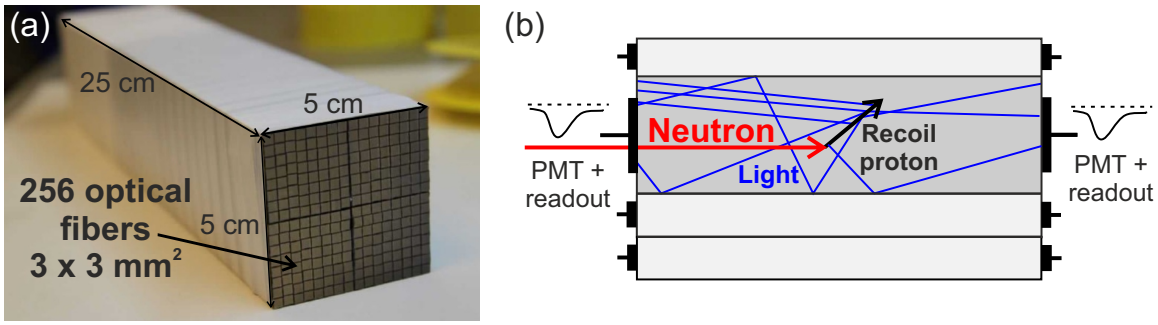

Figure 8.1: Panel (a): photograph of the prototype of the NeuRad detector. One test bundle is 25 cm long and consists of 256 fibers. Panel (b): the principle of NeuRad operation. The detector is placed along the trajectory of the decay neutrons. An incoming neutron interacts with the matter (e.g., by elastic scattering) inside one of the fibers, and the recoil proton ionizes the scintillation material, which produces a light flash. The light travels to both photomultiplier tubes (PMTs), where the signal is read out. The size of fiber where the neutron detection is shown is enlarged for illustration purposes.

read-out from each channel (fiber) independently and pass further to the corresponding front-end electronics.

One of the significant NeuRad characteristics, which deserve special attention, is the time resolution. By measuring the time difference of the signals from opposite photo-detector channels on one fiber, one can determine the first interaction point and its longitudinal coordinate along the fiber. For example, in order to obtain a position resolution of a 6 cm, one has to have time-uncertainty down to 0.5 ns. Also, it is important to distinguish exactly the first neutron hit, because this information serves for discrimination of multi-neutron events from the multiple hits of a single re-scattered neutron (neutron cross-talk).

8.1.1 First test of the NeuRad prototype

The first test, aimed to obtain timing characteristics of the NeuRad detector, has been conducted in Flerov Laboratory of JINR, Russia [133]. The prototype of NeuRad, made out of plastic polystyrene-based scintillating fibers BCF-12 [134] and coupled with two H9500 PMTs [135] has been tested. The setup was placed in a light-tight black box together with a radioactive source of γ-rays ^{60}Co with the γ-energies E_γ = 1173, 1333 keV. The source was placed near the middle of the prototype, see Fig. 8.2 (a). A γ-ray from the source interacts via the Compton scattering inside one of the fibers, followed by a scintillation light flash due to the ionization of the Compton-scattered electron. The light signal from this fiber was registered by the PMTs on both sides and then converted into an electrical pulse that was transmitted to the front-end ADC (analog-to-digital converter). During the test, two channels on each PMT were used and connected to neighboring fibers. The signal from one of the PMT channels was set as a trigger, requiring its amplitude to exceed the 20 mV threshold. The data

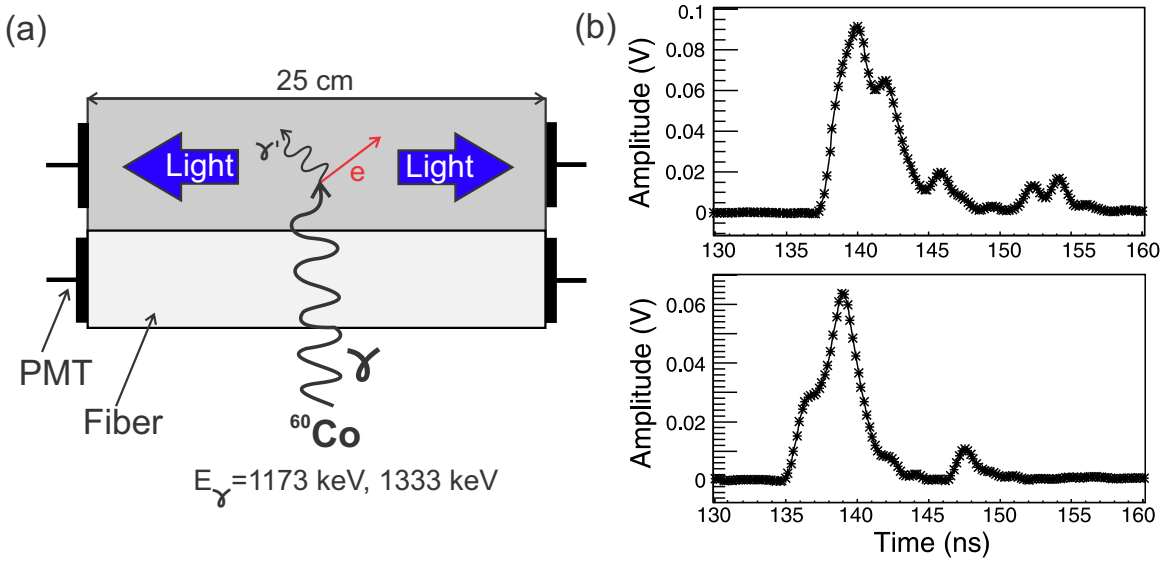

Figure 8.2: Panel (a): scheme of the NeuRad prototype test with the ^{60}Co gamma-ray source. Two fibers are optically coupled to four read-out PMTs. A sketch of Compton scattering is shown in one of the fibers. Compton-scattered electrons create light inside the fiber. Panel (b): two typical signal shapes of the NeuRad prototype, recorded by the DRS4 digitizer. The sampling points are shown by stars.

readout was done by the four-channel DRS4 digitizer board[2] with sampling frequency of 5 GS/s and 1024 sampling points [137]. The DRS4 board functions are very similar to the standard oscilloscope ones, it produces the data in the digitized form of signal shapes.

The typical signal shapes[3], obtained during the gamma-ray source irradiation of the NeuRad prototype, are presented in Fig. 8.2 (b). One can see that the signal shapes show various structures. Such behavior may have several reasons: reflections of light due to accidental clearances in the light-tight coverage of the fibers, low amount of collected light (small statistics) or gamma-ray scattering. In order to understand the signal shape, a Monte-Carlo simulation of the NeuRad response has been carried out within the ExpertRoot framework [138], see details in [139]. One detector signal was calculated as a sum of single photo-electron pulses taking into account such effects as the light collection efficiency, inter-fiber cross-talk, detection threshold, and luminescence kinetics.

An integral signal spectrum from one PMT channel has a smooth shape due to integration by parasitic capacities, see Fig. 8.3. The sum of the signals cancels out the randomly-distributed single photo-electron pulses, pronouncing the clear exponential decay shape of the emitted light. As a first approximation, the time evolution of the reemission process may be described as a simple exponential decay [140]. In this case, the rise time of the signal from zero to the maximum is shorter than the decay time. The estimated rise time of the integral signal from Fig. 8.3 is about 3 ns. As for the decay time, one can try to resolve its fast and slow components by performing the

[2]In future, the EXPERT group plans to equip the prototype and the final version of the NeuRad detector with the multi-channel electronics board from PETsys company [136].

[3]The negative amplitudes of the PMT signals have been inverted by the DRS4 board.

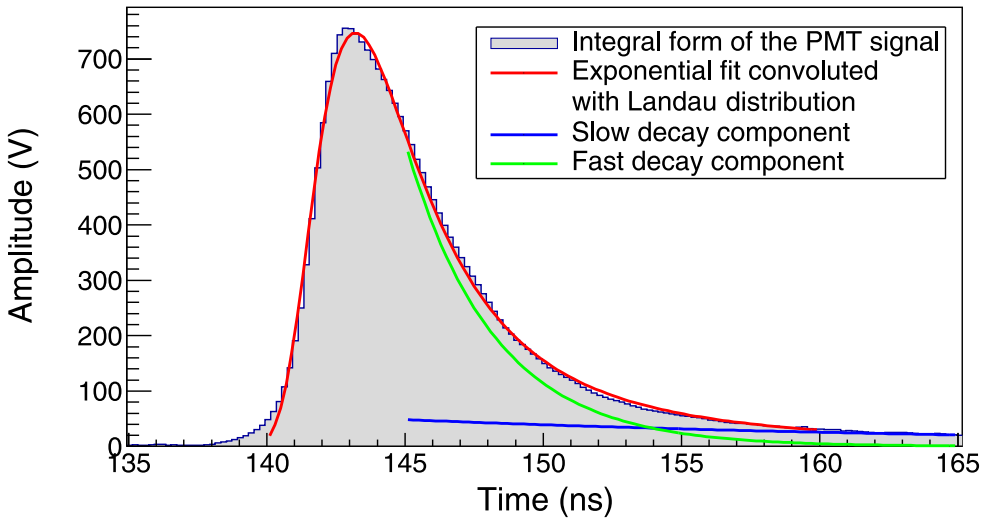

Figure 8.3: Integral form of the signal from one PMT channel. The two-exponent function from Eq. 8.1 convoluted with a Landau distribution is shown in red. The fast and slow exponential decay components are shown by green and blue curves, respectively.

two-exponential fit of the integral signal slope using:

$$N = A \exp\left(\frac{-t}{\tau_f}\right) + B \exp\left(\frac{-t}{\tau_s}\right) \tag{8.1}$$

where N is the number of photons emitted at the time t, τ_f and τ_s are the fast and slow decay constants, respectively, and A and B are the relative magnitudes of the decay constants.

Performing a fit of the integral signal with the double-exponential decay function from Eq. 8.1, one can estimate that the fast component τ_f has a value around 3 ns. It dominates over the slow one with a value of $\tau_s \approx 25$ ns. To properly fit the whole signal shape, one needs to convolute the exponential decay with the appropriate detector response function. Here, the response is considered as a Landau distribution. One must note, that the tail of the rise time can not be described well by a Landau fit function. Therefore, this issue requires further investigation.

8.1.2 Analysis of the timing properties

There are widely-known techniques to obtain the precise timestamp of a signal, i.e., that moment in time, which is determined by the physical event (interaction of the particle). The present data analysis implements different signal-treatment procedures, such as Constant Fraction Discrimination, Leading Edge Analysis, fitting the shape of rising edge, etc. The complex signal shapes, recall Fig. 8.2 (b), show the necessity to apply selections on the time marks (Time-over-Threshold, rise time, slope coefficient). All the above-mentioned procedures are briefly presented below and their illustrations are shown in Fig. 8.4. The analysis is carried out by the means of a dedicated pulse-shape-analysis in the software package ExpertRoot.

- **Constant Fraction Discrimination (CFD).** The CFD method yields a time stamp at a certain fraction of a rising edge of the analog signal. This is done by

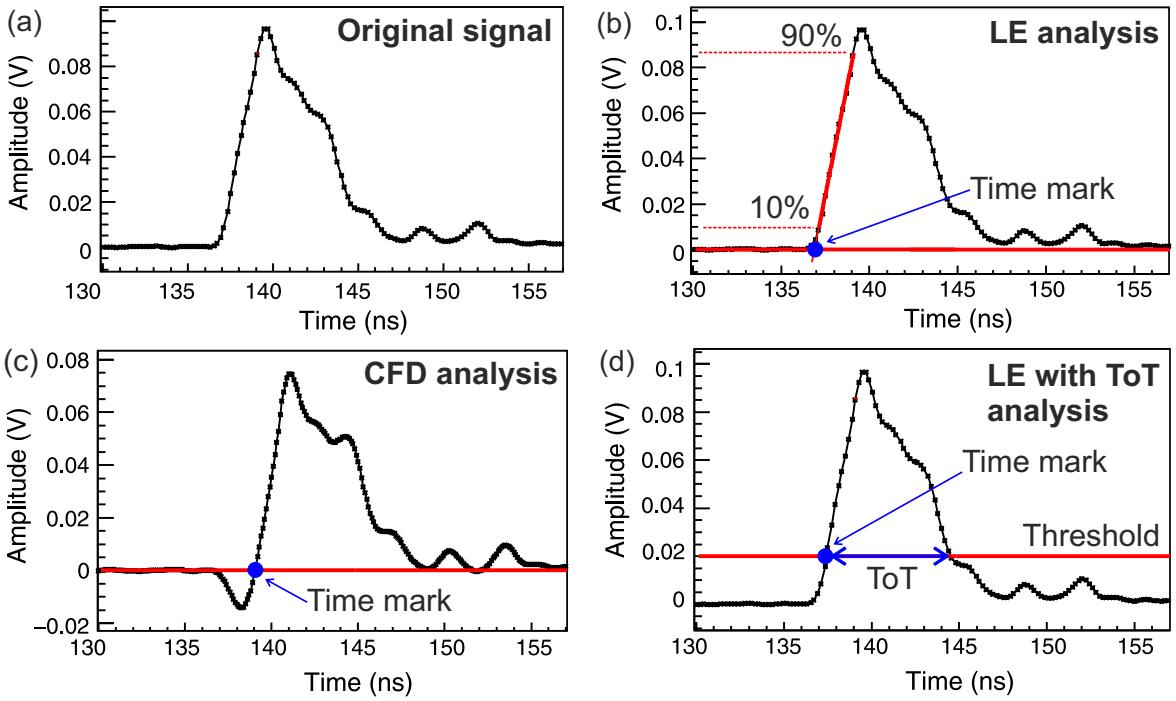

Figure 8.4: Panel (a): original signal of the PMT. Panel (b): leading edge analysis. The time mark is determined by the crossing point of the rising edge linear fit (from 10% to 90% of the maximum amplitude) and the zero level. Panel (c): CFD transformation of the signal from the original shape in (a) with an attenuation value of 0.3 and time delay of 1.5 ns. Panel (d): leading-edge analysis with Time-over-Threshold. The time mark is determined by the crossing point between the set threshold value and the rising edge of the signal. The Time-over-Threshold value is the time between points where the rising and falling edges cross the threshold.

dividing the signal into two parts: one is inverted and attenuated, the other is delayed. These two signals are summed, and the obtained "zero-crossing" point is defined to be the time stamp. In Fig. 8.4, the original and the CFD-transformed signals are shown on panels (a) and (b), respectively. The attenuation value and the time delay are the main parameters that can be varied to obtain the best result. The values around 0.3 for attenuation and 1.5 ns for the time delay were selected for the present analysis.

- **Leading Edge analysis (LE).** The rising edge of a signal can be fitted by a linear function, and the arrival time of the particle is determined by the crossing point between the fitting function and a fixed threshold level, see Fig. 8.4 (c). In the considered case the data between 10% and 90% of the signal amplitude have been fit with a polynomial of first order and the crossing point with the baseline is taken as the time stamp.
- **Time-over-Threshold analysis.** One more way to obtain the timestamp of the particle arrival is to set a fixed threshold value. This, as well as the CFD method, can be realized either within an analog electronic device (leading edge discriminator), or numerically during the data analysis procedure. By setting a certain threshold value, one can obtain a time mark twice (two points where the rising and falling edge of the signal cross the set threshold) as well as a Time-over-Threshold parameter (ToT),

see illustration in Fig. 8.4 (c). The ToT value depends on the signal amplitude and width. For example, by setting a threshold value, one can eliminate background noise signals with small amplitudes. In the present analysis, the optimal threshold value was determined to be 0.02 V. This choice can be explained by the presence of one-electron events with low amplitudes. These events can be considered as a single-electron background produced by the PMT. In such a case, a PMT signal occurs on one side of a fiber only, which contradicts the detection of a light flash at both ends of the fiber.

The above-mentioned methods have been implemented into the analysis, aimed to obtain the difference between the time marks of the signals from opposite PMTs on one NeuRad fiber. In the case of detection of γ rays from a source located near the middle of the prototype, the time distribution is expected to have a peak-like shape. It can be fitted by a Gaussian function. Its standard deviation σ is considered to be the time-uncertainty parameter. The obtained time-difference distributions are shown in Fig. 8.5 (a-d). Panel (a) hosts the time-difference histogram obtained by the CFD method. Panels (b) and (d) illustrate the leading edge analysis method with the threshold set on the 50% and 10% point of the leading edge, respectively. And (c) shows the time difference for the marks obtained with the linear fit of the leading edge crossing zero. The following information could be extracted out of the time-difference distributions and their Gaussian fits: the values of the time-uncertainty σ are in the range of 1.3 – 1.9 ns. The best result $\sigma \approx 1.3$ ns is obtained for the CFD method, which corresponds to the position resolution larger than 10 cm. This doesn't quite satisfy the NeuRad requirements. Therefore, a more careful analysis is required.

One opportunity of improving timing is the correction of a time-amplitude dependence or so-called "walk" effect. To do so, the charge or the amplitude of the signal has to be taken into account. The charge transfer through the surface over the time t can be estimated as:

$$Q = Ut/R, \tag{8.2}$$

where U is an integral over the signal amplitudes, t is the time of the signal duration, R is the input impedance of the DRS4 device. Now, the correlation between the charge and the time difference can be obtained, see Fig. 8.6(a,b,c). The two-dimensional histogram on panel (a) exhibits a charge or amplitude dependence on the time difference calculated by the leading edge method. In an ideal case, independent of the amplitude, the time difference should be constant. But the presence of the "walk" effect spoils the time resolution. It can be partly compensated by the application of the CFD method instead, see Fig. 8.6 (b). Comparing histograms from panels (a) and (b), one could notice that the time-amplitude correction by the means of CFD doesn't perfectly straighten the dependence curve. This can be due to the variation of the signal shapes, recall Fig. 8.2 (b).

The excessive CFD walk can be reduced by a correction of the time-amplitude dependence [141]: each event's time value is shifted relative to an arbitrary determined standard, based on its corresponding charge/amplitude value like $t' = t + k/a$. Here, k is a coefficient which value depends on the desired shift along the time-axis, t and t' are the initial and final time values, a is an amplitude. As an example, let's take the point with the coordinates (-3, $0.02 \cdot 10^{-9}$), see the histogram in panel (c) in Fig. 8.6. To straighten the dependency it has to be shifted to the right on the value of 2 then the expression is $t' = t + 2 \cdot 0.02 \cdot 10^{-9}/a$. The coefficient $k = 2 \cdot 0.02 \cdot 10^{-9}$, applied to another

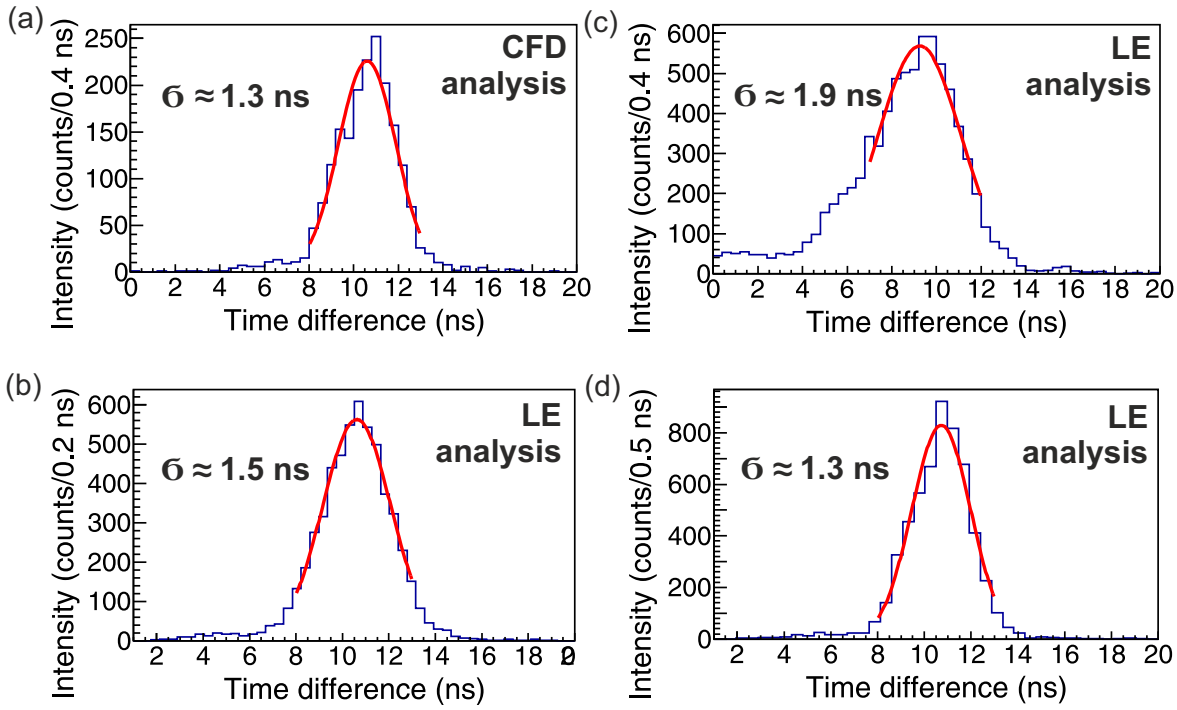

Figure 8.5: Time difference histograms - the difference between time marks of the signals from opposite PMTs obtained by different methods. Panel (a): Constant Fraction Discrimination technique. Panel (b): Leading Edge analysis with a linear fit crossing zero level. Panel (c): Leading Edge analysis with the threshold crossing the 50% level of the rising edge. Panel (d): Leading Edge analysis with the threshold crossing the 10% level of the rising edge. The red curve on all panels is a Gaussian fit function, from which the time-uncertainty parameter σ is derived.

point, gives a time shift depending on the amplitude's value. Then the dependency is straightened a bit more, see panel (c) in Fig. 8.6. Unfortunately, the applied correction procedure gives an insignificant improvement in terms of time-uncertainty value, see the time difference distribution with $\sigma \approx 1.3$ ns in Fig. 8.6(d).

Another possibility to improve the resolution is to apply the Time-over-Threshold selection to large signal amplitudes. In Fig. 8.7 (a) the ToT spectrum for one PMT channel can be seen. The spectrum has a specific shape. The first maximum with ToT < 1 ns can be referred to as the electric noise. The second maximum with ToT from 1.0 ns to 3.0 ns is the single-electron background. Finally, the scintillation signals induced by the γ-ray source have ToT values in the range of 3 to 8 ns, see the typical amplitudes in Fig. 8.2 (b). If the corresponding ToT selection is applied, the time difference spectrum has a time uncertainty of $\sigma \approx 1.0$ ns, see Fig. 8.7 (b). It should be mentioned that the γ-particles in this experiment were not perfectly collimated, which could also give an additional time spread of 0.4 - 0.5 ns of the time signal.

8.1.3 Reference measurement

To pinpoint the limiting factors of the NeuRad timing properties, a reference measurement has been carried out. The scheme of the measurement was similar to the prototype test as described in Subsection 8.1.1 with the setup sketched in Fig. 8.2 (a).

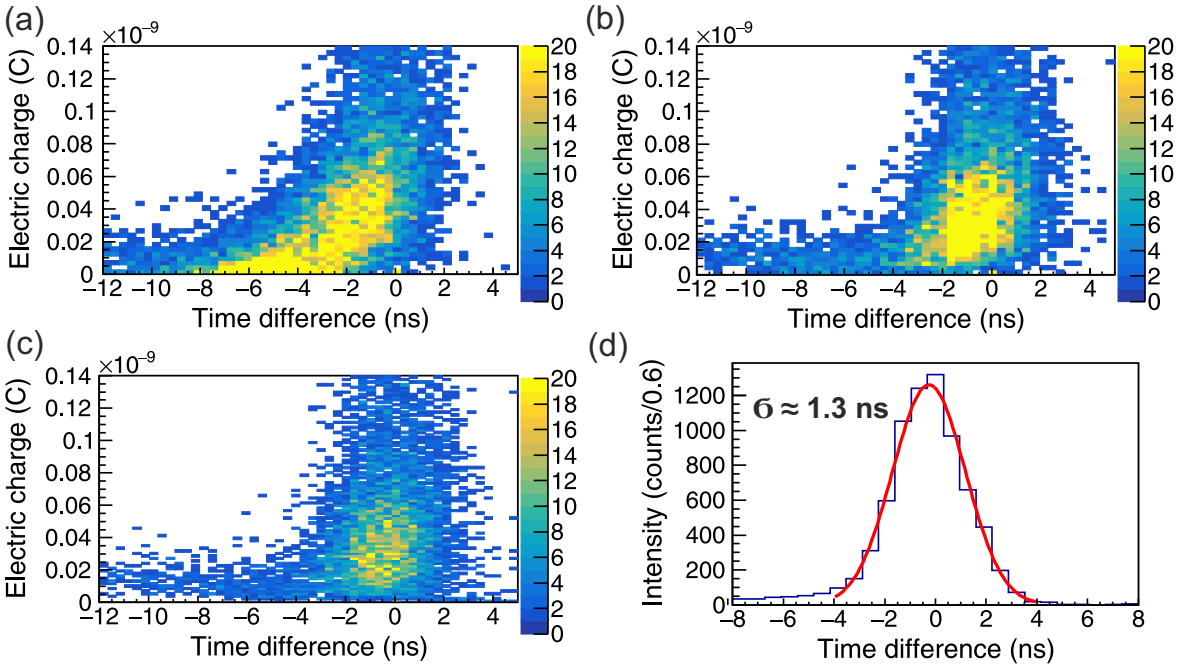

Figure 8.6: Illustration of the "walk" effect and its correction. Panel (a): collected signal charge as a function of the time-difference, obtained by the leading edge analysis method. Panel (b): collected charge as a function of the time-difference, obtained by the CFD method. Panel (c): manually-corrected charge – time-difference dependence from panel (b). The color code in (a–c) represents the number of counts. Panel (d): the manually-corrected time-difference from (c) with the Gaussian fit, shown by the red curve.

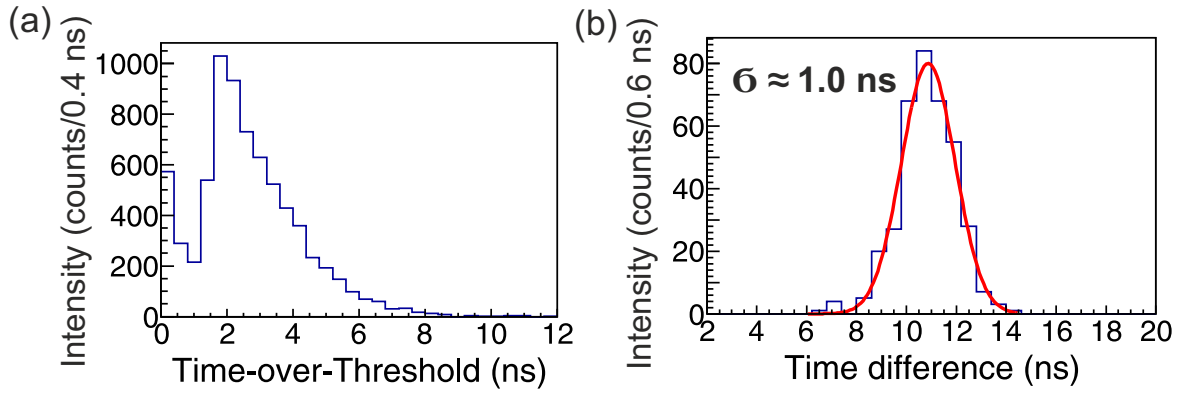

Figure 8.7: Panel (a): Time-over-Threshold spectrum for one of the PMT channels. Panel (b): the time difference spectrum with the ToT selection on the scintillation signals coming from the gamma-ray source. The red curve is a Gaussian fit with the time uncertainty of $\sigma \approx 1.0$ ns.

A plastic scintillator BC-420 (4 mm thick) coupled to two H9500 PMTs was irradiated by a γ-ray source ^{137}Cs with $E_\gamma = 672$ keV. An oscilloscope with 20 GS/s sampling frequency has been used as a data acquisition device. Rise and decay time of the scintillator signal has been determined to be 0.5 and 1.5 ns, respectively. The time

difference histograms have been obtained in two ways: with the help of built-in oscilloscope formulas and the developed pulse shape analysis procedures described earlier in this Section. Both the built-in mathematical functions and the developed analysis allowed for the measurement of the time mark on the level of 50% of the opposite PMT's rising edges. The obtained time difference spectra showed the time-uncertainty σ values of 0.5–0.7 ns.

8.1.4 Test with multi-channel electronics

The next test of the NeuRad prototype has been done with a multi-channel electronics [142]. For this purpose, the readout system from the PETsys Electronics [136], has been chosen. This system is based on the high performance TOFPET2 ASIC [143], which is a new 64-channel chip combining a current amplifier, discriminator, Time-to-Digital Converter (TDC), and Charge-to-Digital Converter (QDC). It is developed for the readout and digitization of signals from fast photon detectors in applications where high data rates up to 0.5 MHz and time resolution down to 100 ps are required. To test the TOFPET2 performance, the PETsys company provided an Evaluation Kit. It includes two LYSO crystals (Cerium doped Lutetium based scintillation crystal) of 3×3×5 mm^3 viewed by two silicon photo-multiplier (SiPM) arrays mounted on a board that plugs into the TOFPET2 ASIC test board. The kit has been tested with a ^{22}Na source producing two gamma rays emitted in opposite directions with 511 keV energy each. The time resolution obtained with the kit is $\sigma \approx 95$ ps, see Fig. 8.8 (a), or $\sigma \approx 67$ ps per channel.

The NeuRad prototype (see Fig. 8.1 (a) and the above text for details) has been tested with the PETsys evaluation kit using cosmic radiation. The H9500 PMTs were coupled to the electronics, so the signals from only 64 fibers on each side were measured. The data acquisition was set in coincidence mode, i.e., only events creating signals on both PMTs with a time difference less than 20 ns were recorded. The precise timing of

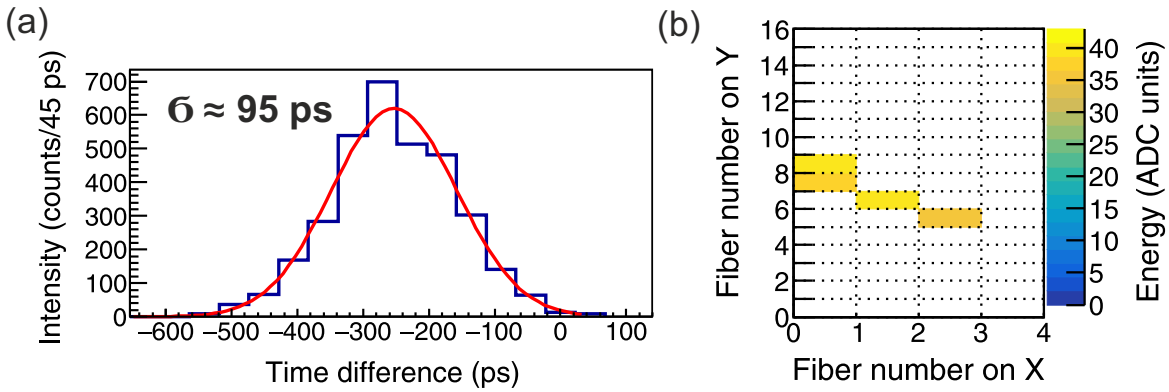

Figure 8.8: Panel (a): time resolution obtained in the reference measurement of two gamma-rays from a ^{22}Na source with two LYSO crystals, SiPM photo-sensors, and the front-end electronics TOFPET2 ASIC. The red curve is a Gaussian fit function. Panel (b): the track of a cosmic-ray particle in the transverse plane of the NeuRad prototype. Both sides of 4×16 fibers are read out by the PMTs and TOFPET2 system. The measured light intensity (proportional to ionization energy loss in a fiber) is shown on the right scale.

the signals in each channel (fiber) allowed for the restoration of the track of the cosmic minimum-ionizing particle crossing the NeuRad prototype. In Fig. 8.8 (b), one can see a typical track from a cosmic particle presented in the transverse cross-section of the prototype. The presented event has the time uncertainty of $\sigma = 0.5(3)$ ns.

8.1.5 Timing performance of the NeuRad prototype

- The time uncertainty of the 25 cm long NeuRad prototype was measured with a γ-ray source ^{60}Co and evaluated by the developed off-line pulse-shape analysis software. The resulting time-uncertainty parameter is 1.0 ns.
- The reference test with a 44 mm thick scintillator BC-420 and a ^{137}Cs γ-ray source has shown that the time resolution can be improved down to $\sigma \approx 0.5$ - 0.7 ns.
- The measurement with the PETsys evaluation kit has shown that the tracks of minimum-ionizing cosmic-ray particles can be determined within each fiber of the NeuRad detector prototype by using the TOFPET2 ASIC electronics with a time uncertainty value $\sigma \approx 0.5$ ns. With such a resolution, it is possible to measure the longitudinal coordinate of a neutron hit with a precision of about 6 cm. This meets one of the main requirements on the NeuRad timing properties.

8.2 Silicon Time-of-Flight detectors

One more principal component of the EXPERT project is the silicon Time-of-Flight detectors, see Chapter 1 for the description of the setup. These silicon detectors are planned to be used for triggering, time, and energy-deposition measurements. They should provide timing information with the resolution $\sigma \approx 50$ ps for heavy ions like gold, uranium, and $\sigma \approx 100$ ps for the lighter ions. Similar ToF detectors are also planned to be used at the Super-FRS for the particle identification.

An important part of the beam diagnostics of the future super-conducting fragment-separator Super-FRS at FAIR will be the time-of-flight measurement. The in-flight separator will provide a broad range of exotic nuclei beams from hydrogen up to uranium. In order to obtain information on the specific desired isotope, one needs to perform an event-by-event identification of the ions transported through the Super-FRS. The conventional method of the $B\rho - \Delta E -$ ToF particle identification is the simultaneous measurement of the energy deposition, time-of-flight, and the magnetic rigidity, see Subsection 4.1.2. The reliability of this particle identification depends, in particular, on the accuracy of the time measurements, i.e., on the ToF detectors time resolution. For example, for unambiguous identification of the light ions with mass number around 10, the time resolution should be about 300 ps (σ). For the heavy isotopes like uranium, the time resolution of ToF detectors is more demanding and should be of about 30 – 50 ps. Such a a value is challenging to obtain with the present detectors and the corresponding electronics. Typically, scintillation detectors are used for the ToF measurements. However, they have a short lifetime when detecting heavy ions with high intensities. Thus, fast radiation-hard silicon strip detectors (SSDs) for the ToF measurement for beam diagnostics [144] at the Super-FRS and as well as at the EXPERT experiments [4] have been suggested.

In this Section, the tests silicon detectors for time measurements at the Super-FRS and within the EXPERT experiments are presented. The main part of the work is

devoted to an investigation of the time characteristics of the silicon detectors under the irradiation caused by intermediate-energy Xe and C beams. The work, presented here, has been published in [145].

8.2.1 Beam test of silicon detectors for ToF measurement

The test of a few SSD prototypes has been performed using ^{124}Xe and ^{12}C primary beams at energies of 600 MeV/u at GSI. The beam intensity was varied between 10^3 and 10^5 ions/s. Several types of silicon detectors were used: a prototype SSD B with an active area of 64×64 mm^2 and a strip pitch of 1 mm, and a prototype SSD A with the same strip length but a different topology (it was divided into 3 groups of strips with pitch widths of 1, 1.5 and 2 mm). In addition, a non-segmented silicon quadrant detector was used as a start detector. It consisted out of four 3×3 mm^2 pads. Each of the detectors had a thickness of 300 μm. The scheme of the measurement setup is shown in Fig. 8.9.

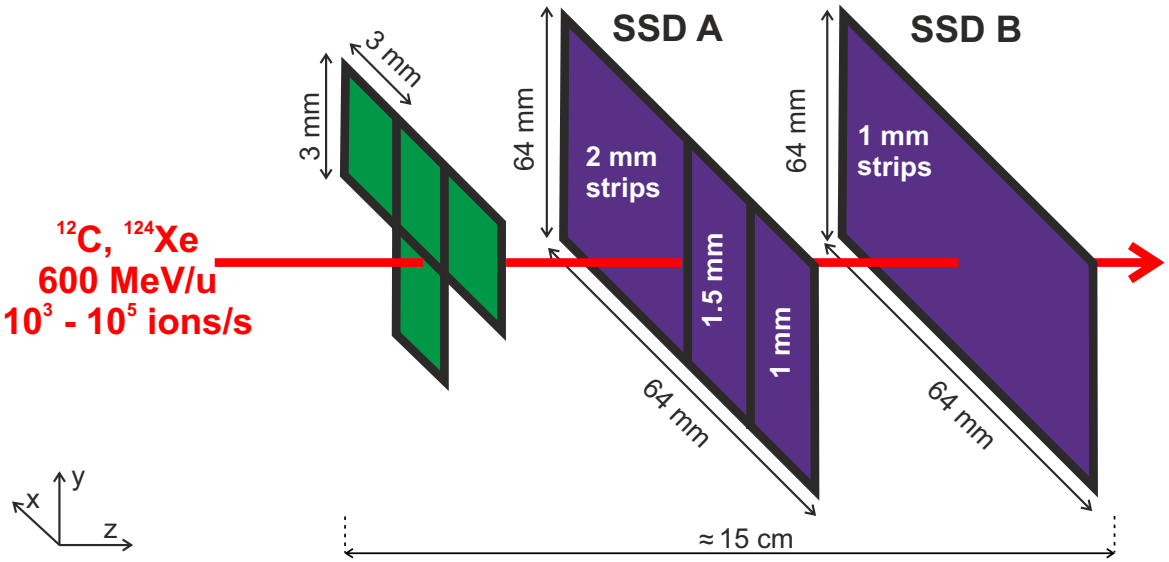

Figure 8.9: Scheme of the beam test of silicon detectors. The prototype strip detectors SSD A and B are shown in purple. Four non-segmented reference detectors are shown in green. The dimensions and strip pitch of the detectors are indicated.

In order to perform fast time measurements, dedicated fast readout electronics was used: a preamplifier/discriminator PADI ASIC [146] and a VME-based high-resolution TDC implemented in a Field Programmable Gate Array (FPGA) VFTX2 [147]. Both devices are custom-designed and developed at the GSI Experiment Electronic Department.

The ions of ^{124}Xe produce signals in SSD prototypes with amplitudes of about 40 mV and for ^{12}C of about 15 mV. The signals had rise times of about 1.2 ns. The amplifiers of PADI increased the signal amplitude by a factor of 100. The thresholds for the PADI discriminator were set to the value just above the noise level. The PADI output signals in LVDS (low-voltage differential signaling) standard were connected to the VFTX2 TDC. The FPGA of VFTX2 is running on a 200 MHz clock, which corresponds to a 5 ns time cycle. In order to perform the precise timing, the measurement

is split into the coarse time with clock cycle of 5 ns and fine time for "tuning", see Fig. 8.10 (a). The internal time resolution of VFTX2 is around 7 ps.

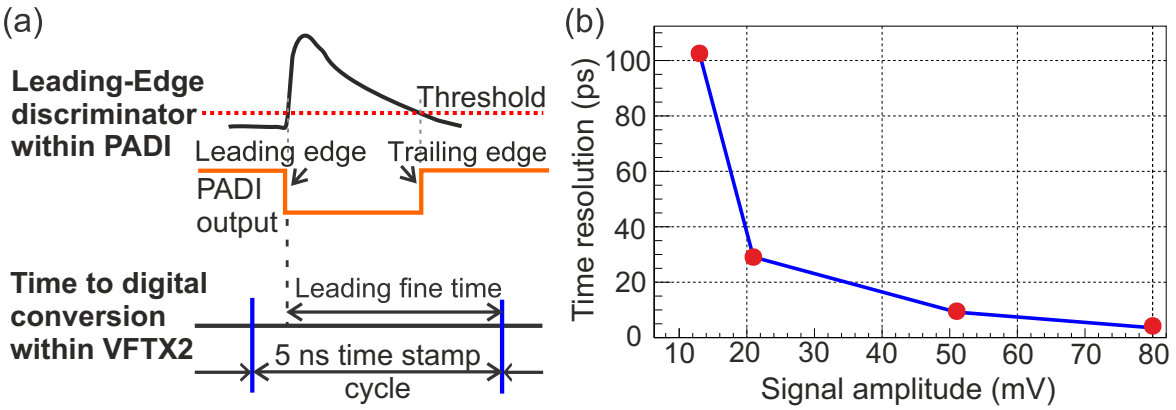

Figure 8.10: Panel (a): scheme of signal processing within the PADI-VFTX2 electronics. The top panel shows the signal treatment by PADI, the bottom panel by VFTX2. For leading/trailing edges of the input signal from PADI, two values are recorded by VFTX2: the corresponding time stamp and a fine time. (b) Dependence of the intrinsic time resolution σ (channel-to-channel) of PADI-VFTX2 electronics on the amplitude of the input signal, generated by a pulser.

8.2.2 Data analysis

An important parameter for accurate time measurements is the slope of the rising (leading) edge of the signal. A very steep and short (order of 1 ns or less) leading edge helps to decrease such effects as time jitter. Also, the noise level must be kept as small as possible. Another phenomenon that influences the accurate time marking is the time-amplitude dependence. A short review of the time measurement techniques can be found in Subsection 8.1.2 of this Chapter. The PADI board has only a Leading-Edge discriminator, but the output signal length depends on the amplitude (see Fig. 8.10 (a)). Due to this and the fact, that the VFTX2 performs time measurements of both, leading and trailing edges, a parameter like ToT can be used for a signal selection and correction of the time-amplitude dependence. The value of ToT is proportional to the amplitude of the signal. One can improve the time resolution by applying the correction of the time difference vs. ToT value. In the considered case, this dependence is rather small.

In Fig. 8.11 (a) the ToT two-dimensional distribution derived from the SSD A and SSD B channels measured in coincidence is presented. The histogram in Fig. 8.11 (b) shows the ToT spectrum for one of the detectors. By applying the selection gate shown in Fig. 8.11 (a) by the solid black line, one takes into account only the events with similar ToTs and the highest number of coincidences. The applied gate helps to improve the time resolution by a factor of 2, which is illustrated below.

The time difference distribution is obtained using the following equation

$$dt = (lts1 - lts2) * 5000 - (ft1 - ft2) \tag{8.3}$$

where dt is the time difference in picoseconds; $lts1$, $lts2$ are the coarse time stamps of channels 1 and 2; $ft1$, $ft2$ are the corresponding fine times. The fine time values were calibrated.

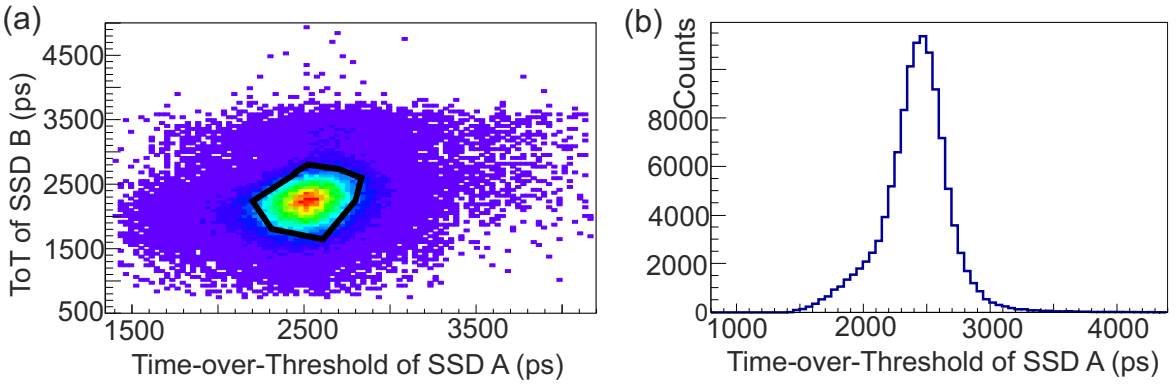

Figure 8.11: Panel (a): measured Time-over-Threshold coincidence distribution. The solid black line shows the area with the highest number of coinciding events with similar ToT values. Panel (b): ToT spectrum of the SSD A channel.

The resulting time difference spectrum is presented in Fig. 8.12. Its shape is a narrow symmetric peak which can be approximated by a Gaussian distribution. For the case of ^{124}Xe, the standard deviation of the time difference is $\sigma \approx 20$ ps, which is, in fact, the total time resolution for the detector pair, see Fig. 8.12 (b). One can estimate that for one detector the time resolution is $\sigma \approx 14$ ps [148].

As mentioned in the previous Section, the signals from ^{12}C were at least two times lower in amplitude than the ones from ^{124}Xe. The time resolution obtained for the SSD pair in the case of ^{12}C is about 100 ps, see Fig. 8.12 (a), which corresponds to individual detector resolution $\sigma \approx 70$ ps, and in the ^{124}Xe case $\sigma \approx 20$ ps. It was found that the different resolution is mainly due to the properties of electronics itself: a test with a pulser has shown, that the intrinsic time resolution of PADI deteriorates with the decrease of the input signal amplitude, see Fig. 8.10 (b). Nevertheless, for the FRS and Super-FRS beam diagnostics and application for the EXPERT experiments, the obtained time resolution is sufficient.

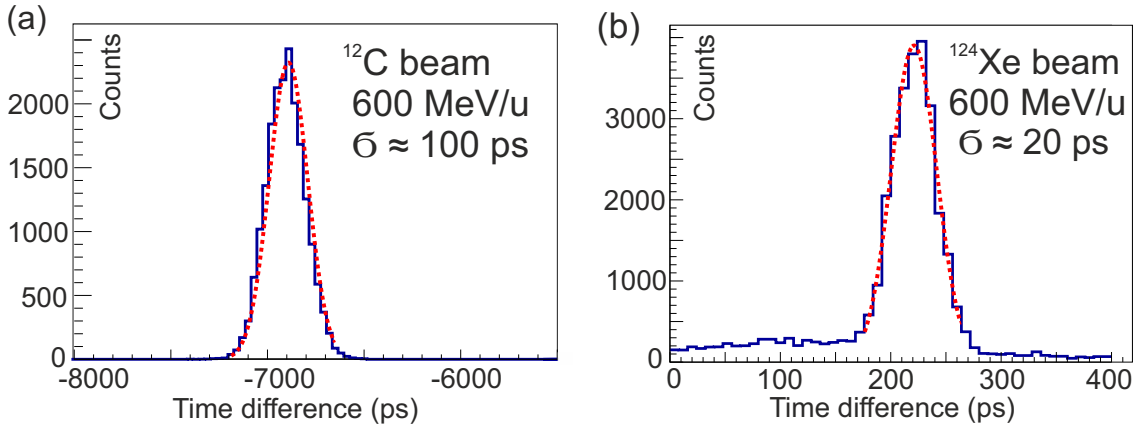

Figure 8.12: Panel (a): time difference spectra obtained with ^{12}C beam at 600 MeV/u. Panel (b): time difference spectra obtained with ^{124}Xe beam at 600 MeV/u. A Gaussian fit is shown by the red dashed curve on both panels.

8.2.3 Timing performance of the silicon detectors

The measured time resolution of the full-size silicon detector prototype with ^{124}Xe beam is $\sigma \approx 20$ ps (including the resolution of 3×3 mm^2 non-segmented quadrant detector). This fully matches the requirements of the ToF system of the beam diagnostics of the future Super-FRS fragment-separator of the FAIR project. Signals from ^{12}C beam have a much lower signal-to-noise ratio leading to the time resolution of $\sigma \approx 100$ ps. This value is mainly determined by the PADI front-end electronics. For light isotopes, this value is sufficient for particle identification.

The time-resolution requirements for the EXPERT silicon ToF system are the same as for the Super-FRS one. Considering the results presented above, one may conclude that these detectors are also suitable for the EXPERT purposes. In this case the silicon ToF detectors are planned to be utilized together with a new selective trigger concept, see Chapter 9 for details.

Chapter 9

Future of in-flight decay technique

The in-flight decay technique utilized by the EXPERT pilot experiments has proven to be a powerful approach to the studies of proton-unbound nuclei far beyond the dripline. A number of proton-decaying isotopes has been investigated up to now: $2p$-emitters ^{16}Ne [30], ^{19}Mg [45], ^{29,30,31}Ar and their decay sub-systems [46, 79, 86], and a $3p$ emitter ^{31}K [78]. There are still many undiscovered nuclei predicted to emit one or several protons. Thus, one can look forward to a continuation of the studies presented in this thesis.

The present Chapter acquaints ongoing in-flight decay studies in Section 9.1, and accepted experiment proposals in Sections 9.2 and 9.3. The final Section 9.4 describes intended EXPERT detector developments (Subsection 9.4.1) and ideas for future investigations of proton-unbound nuclear systems using the in-flight decay technique (Subsection 9.4.2). These studies are particularly interesting, because they allow an excursion far beyond the dripline, into a region where nuclear structure dissolves and the transition to amorphous nuclear matter is expected.

9.1 One-proton emission of ^{69}Br

The upper limit on the lifetime of the $1p$-unbound isotope ^{69}Br is known to be the tens of ns [149]. Thus, this nucleus is a perfect candidate for the in-flight decay experiment. The properties of the ^{69}Br nucleus are essential for understanding some specific aspects of the synthesis of chemical elements in the Universe. Namely, the waiting point of the rp-process (i.e., rapid proton capture, which is one of the mechanisms of the elements synthesis in astrophysical scenarios), ^{68}Se can be bypassed by a sequential two proton capture [150]. The rate of the latter reaction depends on the separation energy of ^{69}Br. The first measurement of the $1p$ separation energy of this isotope was realized in a complete kinematic complete measurement [151]. However, the sensitivity of the measurement depends on the lifetime of ^{69}Br, which was not known at that time.

Thus, the most recent EXPERT experiment was devoted to the studies of the in-flight $1p$-decay of ^{69}Br, precisely speaking: to the measurement of the lifetime of its ground state. Two experimental setups, the EXPERT and the FRS Ion Catcher [89, 152], utilized the same beam of ^{70}Br produced by fragmentation of 1150 MeV/u ^{124}Xe at the FRS fragment separator. The simultaneous use of the secondary beam by the two independent setups was a special feature of the experiment. The FRS Ion Catcher collaboration used the ^{70}Br ions for the implantation into the gas stopping cell placed at the F4 final focal plane to test a novel technique of long-time storage of radioactive

ions (on the example of the isomer 9^+ of ^{70}Br).

The following reaction leading to the production and in-flight decay of the short-lived ^{69}Br isotope was studied:

$$^{124}\mathrm{Xe} \xrightarrow{\text{fragmentation}} {}^{70}\mathrm{Br} \xrightarrow{\text{one-neutron removal}} \mathbf{^{69}Br} \xrightarrow{\text{one-proton decay}} {}^{68}\mathrm{Se} + p \qquad (9.1)$$

The ^{69}Br isotope was created in a one-neutron removal reaction in a 2.25 g/cm^2 carbon secondary target placed at the F2 focal plane. The trajectories of the $1p$-decay products of ^{69}Br, namely ^{68}Se and p, were recorded by the silicon DSSD array placed downstream the target. The detector setup and the FRS ion-optical settings were similar to the ones used in the EXPERT pilot experiment, see Chapter 3. The heavy-ion decay product ^{68}Se was unambiguously identified by the standard FRS detectors at the F2 – F4 focal planes. The data analysis based on the angular correlation measurement and the decay vertex reconstruction (see Chapter 4 for details of the analysis procedures) is ongoing.

9.2 Two-proton radioactivity of ^{34}Ca

Another in-flight decay experiment, devoted to the investigation of $2p$ radioactivity of ^{34}Ca isotope, has been approved for beam time at the BigRIPS fragment-separator [153] in RIKEN, Japan. The ^{34}Ca isotope has been predicted to be $2p$-radioactive by the three-body model [47]. Only an upper limit of 35 ns for its half-life value has been estimated [154]. This fits with the experimental method for the decay-in-flight measurements.

The idea of the experiment is the following. Several proton-rich unbound isotopes, see Fig. 9.1, will be produced with a secondary beam of ^{35}Ca created via fragmentation of ^{40}Ca projectiles (345 MeV/u energy and 200 pnA intensity) at the entrance of the BigRIPS, impinging on a secondary ^{9}Be target at the focal plane F8 of the separator. New proton-unbound isotopes will be studied by tracking their in-flight decay products with silicon microstrip detectors and identifying the heavy decay products (mostly Ar isotopes) by the Zero-Degree spectrometer [155] and its detectors.

Several new physics topics will be addressed in the experiment:

- Search for the $2p$-proton radioactivity of previously unobserved ^{34}Ca isotope, measurement of its decay energy and half-life down to the ps time range, as well as the three-body angular correlation studies. The decay energy of the ^{34}Ca g.s. will provide information on its predicted bubble-like structure[1].
- First spectroscopy of ^{35}Ca isotope. The measurement of its g.s. energy will allow for the investigation of possible halo effects in this nucleus. A discussion about a similar effect in the ^{31}Ar nucleus is presented in Chapter 5.
- Observation and spectroscopy of the most remote ^{35}Sc isotope, which is located 5 mass units beyond the proton dripline. A similar investigation of the ^{31}K isotope (remote by 4 mass units) is presented in Chapter 6, also see [78].

[1]Bubble structure is a central depletion of nucleonic density, predicted for the nuclei with magic numbers of N and Z [156, 157]. Studies of density profiles, form factors, single-particle levels, and depletion fractions reveal that the central depletion is correlated to the shell structure and occurs due to non-occupancy in the s-orbit states and inversion of levels in nuclei with Z $\leq$ 82. In the proposed experiment, the lowest energy states of ^{34}Ca isotope will be measured and compared with the ones of its mirror partner ^{34}Si. The energy shifts may provide first experimental evidence on the bubble-structure effect in ^{34}Ca.

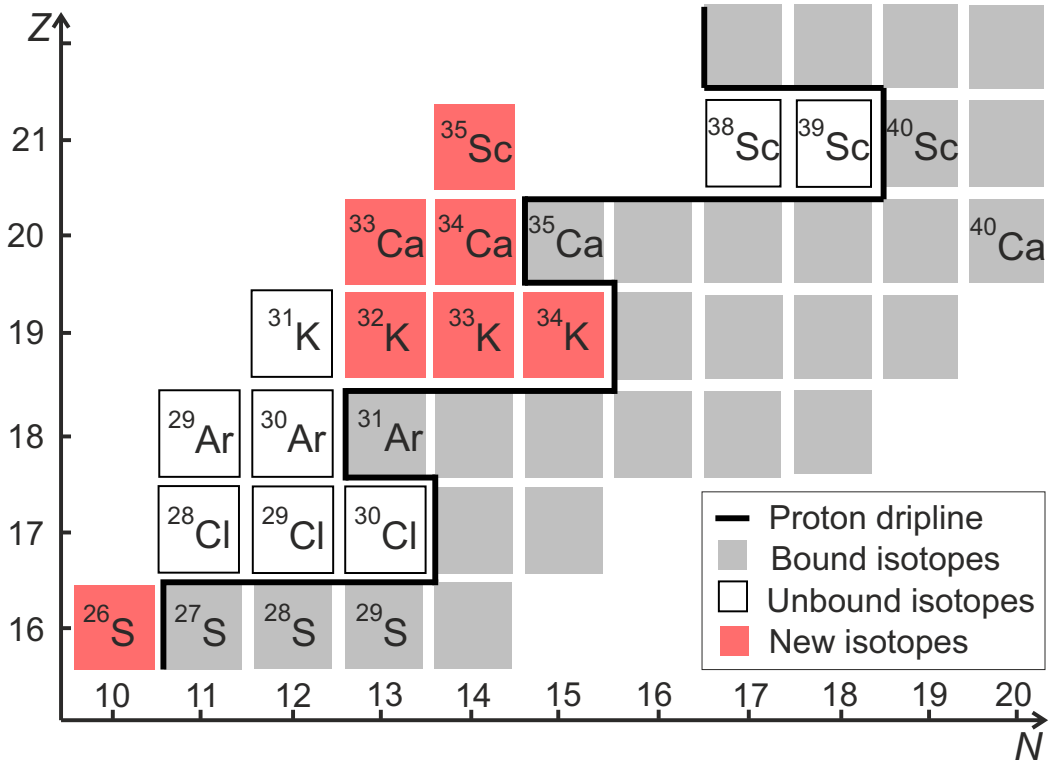

Figure 9.1: Chart of nuclides around the neutron-deficient calcium isotopes according to the database [21]. Discovered bound and unbound isotopes are given by the gray and white squares, respectively. The solid black line indicates the proton dripline. The red-colored squares denote new nuclear species to study in the proposed experiment. They will be produced by primary and secondary beams of ^{40}Ca and ^{35}Ca isotopes, respectively. The location of the undiscovered ^{26}S isotope, a possible candidate for the future in-flight decay studies, is also shown.

- Spectroscopy of previously-unknown isotopes ^{33}Ca, ^{32,33,34}K by tracking their decays in-flight. These measurements will allow for the comparison within bound-unbound mirror nuclei pairs, thus, the investigation of the Thomas-Ehrman shift effect in this remote region.
- Measurements of β-delayed multi-proton emission of ^{35}Ca by an implantation-decay method with the OTPC, which will be performed by utilizing the same beam of ^{35}Ca at the end of the BigRIPS separator. A similar experiment (on β-delayed $3p$ emission from ^{31}Ar) can be found in [20, 114].

All suggested measurements are very similar to the ones performed during the EXPERT pilot experiment, see Chapters 3 and 4 for details.

It should be mentioned that there is another expected but so far undiscovered $2p$ emitter ^{26}S [158], see the location of it on the chart of nuclides in Fig. 9.1. An upper limit on its half-life value of $T_{1/2} < 79$ ns is known [159]. Considering also the theoretical lifetime estimates for the $2p$ decay from the same work, a decay energy limit of $Q_{2p} > 640$ keV for ^{26}S is derived. According to this, it is likely that this nucleus has a lifetime in the ps range. The ^{26}S nucleus is theoretically predicted to possess a $2p$ halo [160]. Altogether, this makes a study of ^{26}S very appealing. Its radioactivity and the accompanying effects may be studied in-flight in the same manner as proposed

above for the ^{34}Ca nucleus.

9.3 Proton radioactivity of light isotopes around carbon

One more in-flight decay experiment has been suggested recently to be conducted at the FRS fragment-separator. It proposes the study of previously-unobserved proton-unbound ^{5}Be, ^{6}B, ^{7}C, and ^{9}N nuclei, see their locations on chart of nuclides in Fig. 9.2. Those isotopes will be created with a secondary beam of ^{9}C produced via fragmentation of a ^{12}C beam. The unbound nuclei will be studied by tracking of their in-flight decay products with silicon microstrip detectors at the F2 focal plane. Their heavy decay fragments, namely, ^{3,4}He isotopes, will be identified by the standard FRS detectors at the F2–F4 focal planes.

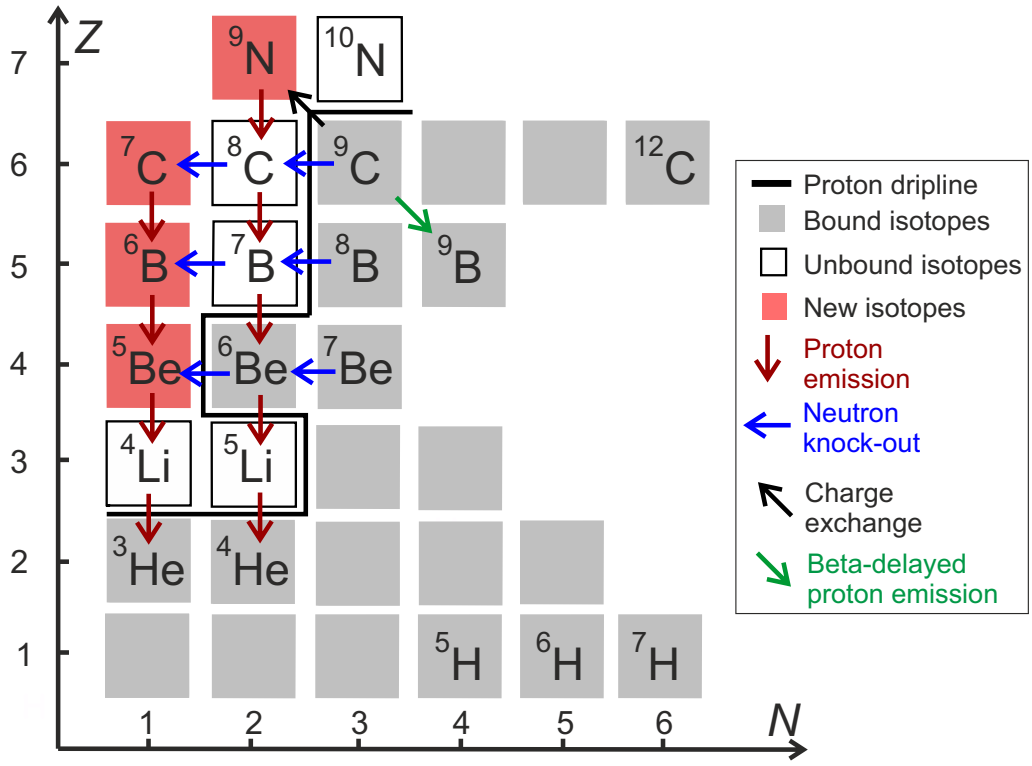

Figure 9.2: Chart of nuclides around the carbon isotopes according to the database [21]. Discovered bound and unbound isotopes are given by the gray and white squares, respectively. The solid black line indicates the proton dripline. The red-colored isotopes are new nuclear species to study in the proposed experiment. They will be produced by a ^{12}C primary and a ^{9}C secondary beams. The colored arrows indicate different reaction mechanisms planned for the investigation, see the legend for details.

Several physics cases are of interest and importance:

- Search for $2p$, $3p$, $4p$ and $5p$ decays of the previously-unobserved ^{5}Be, ^{6}B, ^{7}C and ^{9}N isotopes, respectively. Their decay energies will be derived from the measured three-, four-, five- and six-particle angular correlation. The half-lives will be determined

(down to the ps time range) by detecting the decay vertices at the F2 central focal plane of the FRS. The feasibility of such investigations have been shown in the $2p$-decay study of ^{19}Mg [45], the EXPERT pilot experiment studying argon isotopes [46, 86, 79] and the $3p$ decay of ^{31}K [78], see also Chapters 3 and 4 of this thesis.

- The comparison of the ^{7}C isotope level structure with its isobaric-mirror partner ^{7}H nucleus. The ^{7}H nucleus was intensively investigated in last years, e.g., using the missing mass method [161]. Both mirror partners are the nuclear systems with the largest imbalance between Z and N numbers. In a similar way, the mirror states in the isotope pairs ^{6}B-^{6}H and ^{5}Be-^{5}H shall be studied.
- Measurements of β-delayed proton emission of the ^{9}C nucleus will be performed using the implantation-decay method with the OTPC detector. Similar to the previous experiment of this type [114, 20], the same beam of ^{9}C will be utilized twice, namely also at the final focus of the FRS.

9.4 Further EXPERT setup developments and related investigations

9.4.1 Planned upgrade and improved measurement concept

The planned experiments studying very exotic, short-lived nuclei increase the demands on the detector systems and measuring methods. In this Subsection, the intended developments of the EXPERT detectors and new measuring concepts are outlined.

- **Silicon tracker.** Up to this point, the array of microstrip DSSDs (see Chapter 3 for details) has been used as a charged-particle tracker in the in-flight decay experiments. A perspective alternative for the existing DSSDs are the ALPIDE pixel detectors [162]. Those are the new state-of-the-art tracking detectors developed by the ALICE collaboration of CERN. One sensor with half a million readout channels (pixels) has dimensions of 15 $\times$ 30 mm and is 50 μm thick. It has a position resolution for very light particles down to 5 μm and can stand a readout rate up to 100 kHz. These characteristics may significantly increase the capabilities of in-flight decay experiments. Thus, a version of the EXPERT tracking array comprised out of ALPIDE sensors will be developed in the near future, and the corresponding software, coupling the ALPIDE data with the EXPERT DAQ system, must be created.
- **The further improvements of the NeuRad detector.** As mentioned above in Chapter 8, the detector is planned to be equipped with the PETsys readout electronics. Based on the results of the time-resolution tests and signal-shape analysis of the NeuRad prototype, the PETsys company has developed a new version of the front-end ASIC. With this updated version of the readout electronics, the time resolution of the detector will be improved. A test of an upgraded system is foreseen in the near future.
- **A new trigger concept.** One of the main challenges for the in-flight decay experiments is the background produced by the secondary beams. One possibility of decreasing the rate of unwanted events is a special trigger scheme which is in preparation. It can select precisely the signals from the decay products after the secondary target and provide the trigger to the data acquisition. The rejection of

the contaminant signals based on the velocity measurement is not possible because of the short ToF within the EXPERT setup. And the selection based on charge measurement can not be performed due to the long processing time. Thus, a new trigger scheme based on the charge-selection via the ToT measurement has been proposed. The signals from heavy ions of interest have a particular time length above the set threshold. Thus, a trigger window on this signal time value can be set. A special firmware for the FPGA of the fast waveform digitizer [163] capable of processing the signals from the front-end electronics and producing such a ToT-based trigger has been recently developed by the Struck electronics company. Trigger decision based on this concept is possible within 100 ns which is much faster than any direct charge measurement. The first tests of this module with a signal generator prove the feasibility of the concept. Thus, further investigations of the selective trigger are planned. It should be mentioned that the proposed concept may be universal for other similar secondary-beam experiments.

9.4.2 Opportunities for studies of proton-unbound nuclei

Upgraded detector systems and new measuring concepts outlined in the previous Subsection are planned to be utilized in future in-flight decay studies. Several promising proton-unbound nuclei suitable for such experiments are outlined in this final Subsection.

- **$1p$ emission of ^{73}Rb.** The measurement of its $1p$-separation energy is of interest to astrophysical investigations. Namely, the waiting point of the rp-process, ^{72}Kr ($T_{1/2}$ = 17 s), can be bypassed by the $2p$-capture mechanism going through ^{73}Rb. So far, no direct measurement of the separation energy which is critical for the understanding of this process is available.

  However, this nucleus was found to be unbound with respect to $1p$ emission [164] with no spectroscopic information provided. Recently, based on the flight-path calculations and measured yields of neighboring isotopes, an upper limit on $T_{1/2} < 81$ ns for ^{73}Rb was set [132]. In the same experiment, the decay energy of this nucleus was assumed to be $Q_p > 600$ keV, which is close to the value of $Q_p = 570$ keV from systematics [21]. Considering those limits on half-life and decay energy, one can assume the ^{73}Rb isotope to be suitable for the studies using the in-flight decay technique.

  The short-lived isotope of interest may be produced in the following sequence of reactions:

  $$^{124}\mathrm{Xe} \xrightarrow{\text{fragmentation}} {}^{74}\mathrm{Rb} \xrightarrow{\text{one-neutron removal}} \mathbf{^{73}Rb} \xrightarrow{\text{one-proton decay}} {}^{72}\mathrm{Kr} + p \qquad (9.2)$$

  An experimental approach here might be very similar to the one used in the recent EXPERT experiment studying ^{69}Br, see the first Section of this Chapter.

- **$2p$ emission of ^{38}Ti isotope.** This nucleus has been widely investigated theoretically and predicted to be a $2p$ emitter [19]. An upper limit on $T_{1/2} < 120$ ns was indirectly deduced from the cross-sections estimations [165]. The value of its $2p$-decay energy from different calculations is in the range of 2.5 - 2.7 MeV, for example, see [21, 122]. In contrast, an experimental approach to this nucleus is not so straightforward because it is expected to be plausible for studies in the gap between two techniques: in-flight and implantation decay (see Fig. 2.3 of the Chapter 2). However, one may investigate this nucleus using the in-flight decay technique

combined with the high-precision momentum measurement, see Chapter 7 for the method details. The following chain of reactions may lead to the production of ^{38}Ti isotope:

$$^{46}\mathrm{Ti} \xrightarrow{\text{fragmentation}} {}^{39}\mathrm{Ti} \xrightarrow{\text{one-neutron removal}} \mathbf{^{38}Ti} \xrightarrow{\text{two-proton decay}} {}^{36}\mathrm{Ca} + p + p \qquad (9.3)$$

The combination of in-flight decay tracking and precise momentum measurement may lead to the derivation of the $2p$-decay energy of ^{38}Ti. This discovery may be a step towards filling the gaps in the $2p$-radioactivity landscape.

- **$1p$ emission of ^{44}Mn isotope.** This isotope is a decay sub-system of the "famous" $2p$-radioactive nucleus ^{45}Fe. The latter isotope is extensively studied both theoretically and experimentally, see Chapter 2 for details. The $2p$-decay energy Q_{2p} of ^{45}Fe has been measured several times and the most precise value is 1154(16) keV [48]. However, the value of the $1p$-decay energy of this isotope is only available from systematics, namely, Q_p = 560(640) keV [21]. Thus, the study of $1p$ emission of ^{44}Mn and the derivation of its decay energy may shed some light on the Q_p of ^{45}Fe. The most recent estimate of Q_p for the ^{44}Mn nucleus is 1710(640) keV [21], which is in the order of the total decay energy Q_{2p} of ^{45}Fe. Also, the upper-limit on the ^{44}Mn isotope half-life is known to be $T_{1/2} < 105$ ns [166].

  Thus, taking into account the above-mentioned arguments, one can consider the short-lived ^{44}Mn nucleus to be suitable for the in-flight decay technique. The following reaction sequence may be used to study this isotope:

$$^{50}\mathrm{Cr} \xrightarrow{\text{fragmentation}} {}^{44}\mathrm{Cr} \xrightarrow{\text{charge-exchange}} \mathbf{^{44}Mn} \xrightarrow{\text{one-proton decay}} {}^{43}\mathrm{Cr} + p \qquad (9.4)$$

The production of the prospective in-flight decay candidates, mentioned in this Subsection, might be a challenging task for the present fragment-separator facilities. The forth-coming Super-FRS fragment-separator together with advanced technologies and developments will provide extremely intense and high-purity secondary beams. And, together with the EXPERT setup, new unbound nuclear systems far beyond the driplines will be discovered, expanding the present knowledge about the nuclear structure and its basic principles at the transition to amorphous nuclear matter.

Summary

Several exotic nuclei, located beyond the proton dripline, have been studied in the present thesis. Four new isotopes were discovered, and a variety of nuclear structure findings could be accomplished. In particular, this thesis reports the first observation and spectroscopy of the proton-unbound isotopes in the vicinity of very neutron-deficient isotopes of argon. They are depicted in Fig. 9.3. The corresponding experiments have been performed with the fragment separator FRS [3] of GSI using a start version of the EXPERT setup [4], which is under construction and designed for experiments with even more exotic nuclei at the Super-FRS of FAIR.

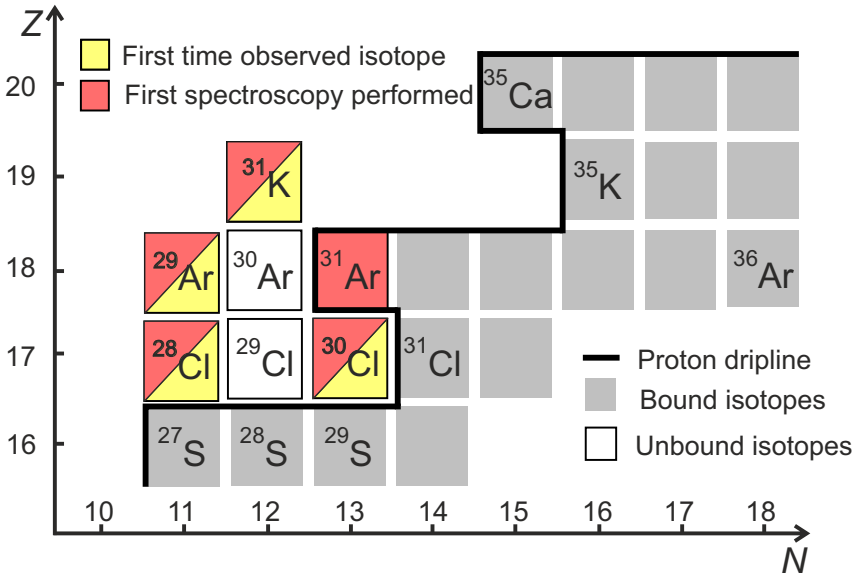

Figure 9.3: Chart of nuclides showing the isotopes that are known to date (according to the database [21]) in the surroundings of the nuclei studied in this work (colored squares). Bound and unbound isotopes are indicated by gray and white squares, respectively. The solid black line shows the proton dripline.

A secondary beam of ^{31}Ar ions has been created via projectile fragmentation of 885 MeV/u ^{36}Ar ions with an intensity of 10^9 ions/s impinging on the production target at the entrance of the FRS. The spatial separation of ^{31}Ar ions has been performed with the FRS operated in a special ion-optical mode applying a degrader at F1 to achieve an achromatic focus at the central focal plane F2, where the detector setup of the EXPERT pilot experiment has been installed. The setup consisted of the 4.8 g/cm^2 Be secondary target and an array of silicon microstrip detectors. The proton-unbound isotopes of interest have been studied by the well-established in-flight tracking technique [75], where the trajectories of the decay products are measured with the array

of silicon microstrip detectors. This allows to measure particularly short-lived nuclei, which exhibit half-lives of the range from ns to ps or even below. Using the in-flight decay spectroscopy, the $1p$ and $2p$ emission processes have been reconstructed from the measured angular correlation in double "heavy ion + proton" and triple "heavy ion + two protons" coincidences, respectively.

In the course of the analysis, the two previously unknown isotopes ^{28,30}Cl, which are unbound with respect to $1p$ emission, have been observed for the first time. To their ground states, the $1p$-separation energies S_p = -1.60(8) and S_p = -0.48(2) MeV, respectively, could be assigned. Excited states of the $2p$ emitter ^{31}Ar have also been identified for the first time. The high level of isobaric symmetry observed in the ^{31}Ar-^{31}Al mirror pair allows to assign a $2p$-separation energy S_{2p} = 6(34) keV to the ground state of ^{31}Ar. The obtained ground state energy of ^{31}Ar is the most accurate evaluation available so far. It improves the results of previous estimates by a factor of three. Also, the $2p$ emitter ^{29}Ar has been discovered. The first excited state of this nucleus with S_{2p} of -5.50(18) MeV has been identified. The data on argon isotopes are published in [79, 2]. One more highlight of this thesis is the discovery of ^{31}K: its observation marks the nuclide, that is hitherto found to be farthest away (four mass units) beyond the proton dripline [78]. It is a $3p$ emitter and has been studied by means of the angular correlation of its decay products, ^{28}S and $3p$. The $3p$-separation energy of the ^{31}K ground state has been assigned to S_{3p} = -4.6(2) MeV. An upper half-life limit of 10 ps of ^{31}K has been derived from the measured decay-vertex distribution.

Overall, the performed studies and obtained results are an essential first step towards wider nuclear-structure studies far beyond the proton dripline, where basic nuclear properties, theoretical concepts (like mean-field theory) and the strong nuclear force in general may be examined. They may open a transition from ordered nucleons in nuclei to amorphous nucleon matter.

Further investigations exploiting the in-flight decay technique shall be performed within the EXPERT project at the future super-conducting fragment separator Super-FRS. Leading to this direction, this thesis presents recent developments of new EXPERT detectors, which aim at the tracking of neutrons originating from neutron-decay reactions (NeuRad detector) and Time-of-Flight measurements for improved secondary-beam identification (ToF detector) at the Super-FRS. Moreover, the further development and refinement of the in-flight decay technique by using in addition precise longitudinal momentum measurements of the heavy ion from the decay performed by the subsequent spectrometer stages of the separator, has been discussed. A novel, complementary method has been proposed and proven to provide a model-independent evaluation of the spectroscopic information. Finally, prospects to forthcoming physics cases that can be studied, dedicated experiment proposals, intended developments of the EXPERT detectors, and ideas for further investigations of proton-unbound nuclear systems using the in-flight decay technique have been discussed.

Zusammenfassung

In der vorliegenden Arbeit wurden exotische Nuklide jenseits der Protonen-Abbruchkante experimentell untersucht. Vier Isotope wurden entdeckt und es konnte eine Vielzahl von Strukturuntersuchungen an ihnen durchgeführt werden. Insbesondere werden der erstmalige Nachweis sowie erste Spektroskopie-Ergebnisse von protonen-instabilen, neutronenarmen Kernen in der Umgebung von ^{30}Ar dargestellt. Die untersuchten Nuklide sind in Abbildung 9.4 veranschaulicht.

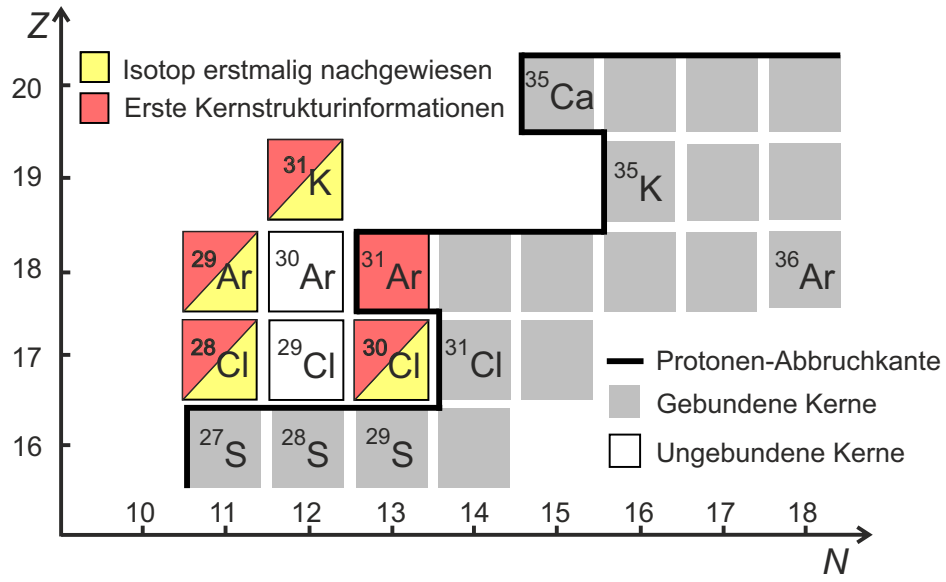

Figure 9.4: Schematischer Ausschnitt aus der Nuklidkarte mit den entsprechend Referenz [21] bisher bekannten Nukliden (grau) in der Umgebung von ^{30}Ar. Die in dieser Arbeit untersuchten Nuklide sind farblich gekennzeichnet, ungebundene Kerne sind weiß. Die schwarze Linie repräsentiert die Protonen-Abbruchkante.

Die entsprechenden Experimente, die zu diesen Ergebnissen führen, wurden am Fragmentseparator FRS [3] der GSI in Darmstadt mit einer Startversion des EXPERT-Detektorsystems [4] durchgeführt. EXPERT ist ein Experiment, welches derzeit aufgebaut wird und mit dem am supraleitenden Fragmentseparator Super-FRS bei FAIR sogar noch exotischere, d.h. noch neutronenärmere bzw. sehr neutronenreiche Nuklide erzeugt und spektroskopiert werden können.

Die Experimente mit EXPERT basieren auf der wohlbekannten Methode der Zerfallsspektroskopie im Fluge [75], bei der die Spuren aller Zerfallsprodukte mit einer großflächigen Anordnung von Silizium-Mikrostreifen-Detektoren gemessen und dadurch Zerfallsdynamik und -eigenschaften der radioaktiven Ionen rekonstruiert werden können; ebenso kann die Lebensdauer der Nuklide sowie Strukturinformation ermittelt

werden. Zerfallsspektroskopie im Flug eignet sich besonders zur Untersuchung von sehr kurzlebigen Kernen, d.h. Nukliden mit Halbwertszeiten im Bereich von ns ... ps oder sogar noch kürzer.

In den vorliegenden Experimenten wurde die Methode auf die Protonen-Radioaktivität von leichten Chlor-, Argon- und Kalium-Isotopen angewendet, wobei die Emission von einem, zwei oder drei Protonen aus dem Grundzustand durch die rekonstruierten Teilchenspuren bzw. deren Winkel-Korrelation (z.B. durch koinzidenten Nachweis von projektil-ähnlichem Schwerion plus Proton oder projektil-ähnlichem Schwerion plus zwei Protonen etc.) untersucht wurde. Ein Sekundärstrahl von ^{31}Ar-Ionen wurde mittels Projektil-Fragmentation eines mit einer Intensität von 10^9 Ionen pro Sekunde und 885 MeV/u einfallenden ^{36}Ar Primärstrahls im Target am Eingang des FRS produziert. Die räumliche Separation der ^{31}Ar-Ionen wurde mittels einer speziellen ionenoptischen Einstellung des FRS erzielt, bei der ein Degrader an der ersten Fokalebene F1 verwendet wird, um eine achromatische Bedingung an der zentralen Fokalebene F2 zu erzielen, an welcher der EXPERT Detektor-Aufbau steht. Dieser besteht hauptsächlich aus einem 4.8 g/cm^2 Be Sekundärtarget und einer Anordnung von mehreren Silizium-Mikrostreifen-Detektoren.

Im Rahmen der Analyse wurden die bis dahin unbekannten Isotope ^{28,30}Cl, die Protonen-ungebunden, also Protonen-radioaktiv sind, erstmalig nachgewiesen. Ihre 1p-Separationsenergie konnte mit $S_p = -1.60(8)$ MeV bzw. $S_p = -0.48(2)$ MeV angegeben werden. Mehrere Anregungszustände konnten erstmalig im 2p-Emitter ^{31}Ar bestimmt werden. Die stark ausgeprägte Isobaren-Symmetrie, die im Spiegelkern-Paar ^{31}Ar–^{31}Cl beobachtet wird, erlaubt die Bestimmung der 2p-Separationsenergie $S_{2p} = 6(34)$ keV von ^{31}Ar, was den bisher genauesten Wert überhaupt darstellt, und den bisher bekannten Schätzwert dreifach verbessert. Weiterhin wurde der 2p-radioaktive Kern ^{29}Ar entdeckt. Sein erster angeregter Zustand konnte identifiziert werden, er ist durch eine Zwei-Protonen Separationsenergie von $S_{2p} = -5.50(18)$ MeV ausgezeichnet. Weitere Ergebnisse zu den Argon-Isotopen finden sich in den Publikationen [79, 2], die als Ergebnis der vorliegenden Arbeit entstanden sind.

Ein weiteres Glanzlicht der vorliegenden Arbeit ist die Entdeckung und erste experimentelle Untersuchung von ^{31}K [78]. Sein Nachweis markiert in der Erforschung exotischer Nuklide jenseits der Abbruchkanten das Nuklid, welches am weitesten jenseits liegt, nämlich vier Masseeinheiten. Darüber hinaus gelang durch die Spurenrekonstruktion des Tochternuklids ^{28}S in Koinzidenz mit drei Protonen der Nachweis, daß es 3p-radioaktiv ist. Die 3p-Separationsenergie des Grundzustands von ^{31}K konnte zu $S_{3p} = -4.6(2)$ MeV bestimmt und für seine Halbwertszeit eine Obergrenze von 10 ps angegeben werden.

Insgesamt liefern die vorliegenden Ergebnisse wichtige Beiträge zu einem genaueren Verständnis der Struktur exotischer Kerne jenseits der Abbruchkanten; sie liefern einerseits wichtige, neue Daten zu Kerneigenschaften und Kernstruktur sowie andererseits zur Weiterentwicklung von grundlegenden Theorien und zu einem besseren Verständnis der starken Kraft. Resonanzzustände und Nuklide mit Lebensdauern, die kürzer sind als eine einzige Schwingungsperiode der Nukleonen im Kernpotentialtopf, markieren möglicherweise einen ersten Schritt zur Beobachtung des Übergangs von geordneten und im Kernverbund fest gebundenen Nukleonen hin zu ungeordneter, strukturloser und amorpher Nukleonen-Materie.

Weiterführende Zerfallsspektroskopie-Untersuchungen im Fluge sind mit dem vollständigen EXPERT-Experimentaufbau am Super-FRS geplant. Im Rahmen dieser

Dissertation wurden dorthin wegweisende Arbeiten durchgeführt. So wurden z.B. neue Entwicklungen für Festkörper-Detektoren ausgeführt und dargestellt, die für die Spurverfolgung von Zerfällen im Fluge verwendet werden, insbesondere zum Nachweis von Neutronen und für Flugzeitmessungen zur weiteren Verbesserung der Identifikation von Sekundärstrahlen am SuperFRS. Ferner wurde eine konzeptionelle Weiterentwicklung und Verbesserung der Zerfallsspektroskopie im Fluge untersucht, nämlich durch koinzidente und alternativ durch die unabhängige Impulsmessung der Projektil-ähnlichen Ionen mittels der hochauflösenden Spektrometer-Eigenschaften der nachfolgenden Sektionen des Super-FRS. Dieses Verfahren kann ergänzend zur reinen Spurverfolgung angewendet werden und ist besonders wertvoll, denn es liefert komplementäre, unabhängige Ergebnisse. Schließlich wurden einige weiterführende physikalische Fragestellungen und experimentelle Zielsetzungen entworfen und diskutiert, ebenso wie zukünftige EXPERT Detektor-Entwicklungen, die der weiteren, detaillierten Erforschung der einfachen bzw. multiplen Protonen-Radioaktivität mittels der Zerfallsspektroskopie von exotischen Kernen im Fluge dienen können.

Bibliography

[1] G.R. Satchler. Direct nuclear reactions. *Claredon Press*, 1983.

[2] L. V. Grigorenko, I. Mukha, D. Kostyleva, C. Scheidenberger, L. Acosta, E. Casarejos, V. Chudoba, A. A. Ciemny, W. Dominik, J. A. Dueñas, V. Dunin, J. M. Espino, A. Estradé, F. Farinon, A. Fomichev, H. Geissel, A. Gorshkov, Z. Janas, G. Kamiński, O. Kiselev, R. Knöbel, S. Krupko, M. Kuich, Yu. A. Litvinov, G. Marquinez-Durán, I. Martel, C. Mazzocchi, E. Yu. Nikolskii, C. Nociforo, A. K. Ordúz, M. Pfützner, S. Pietri, M. Pomorski, A. Prochazka, S. Rymzhanova, A. M. Sánchez-Benítez, P. Sharov, H. Simon, B. Sitar, R. Slepnev, M. Stanoiu, P. Strmen, I. Szarka, M. Takechi, Y. K. Tanaka, H. Weick, M. Winkler, J. S. Winfield, X. Xu, and M. V. Zhukov. Deep excursion beyond the proton dripline. II. Toward the limits of existence of nuclear structure. *Physical Review C*, 98:064309, 2018.

[3] H. Geissel, P. Armbruster, K. H. Behr, A. Brünle, K. Burkard, M. Chen, H. Folger, B. Franczak, H. Keller, O. Klepper, B. Langenbeck, F. Nickel, E. Pfeng, M. Pfützner, E. Roeckl, K. Rykaczewski, I. Schall, D. Schardt, C. Scheidenberger, K.-H. Schmidt, A. Schröter, T. Schwab, K. Sümmerer, M. Weber, G. Münzenberg, T. Brohm, H.-G. Clerc, M. Fauerbach, J.-J. Gaimard, A. Grewe, E. Hanelt, B. Knödler, M. Steiner, B. Voss, J. Weckenmann, C. Ziegler, A. Magel, H. Wollnik, J. P. Dufour, Y. Fujita, D. J. Vieira, and B. Sherrill. The GSI projectile fragment separator (FRS): a versatile magnetic system for relativistic heavy ions. *Nuclear Instruments and Methods in Physics Research Section B: Beam Interactions with Materials and Atoms*, 70(1):286 – 297, 1992.

[4] Technical Design Report of the EXPERT setup for the Super-FRS experiment collaboration. *https://edms.cern.ch/ui/file/1865700/2/TDR_SuperFRSExp_EXPERT.pdf*, 2017.

[5] H. Geissel, H. Weick, M. Winkler, G. Münzenberg, V. Chichkine, M. Yavor, T. Aumann, K.H. Behr, M. Böhmer, A. Brünle, K. Burkard, J. Benlliuer, D. Cortina-Gil, L. Chulkov, A. Dael, J.-E. Ducret, H. Emling, B. Franczak, J. Friese, B. Gastineau, J. Gerl, R. Gernhäuser, M. Hellström, B. Jonson, J. Kojouharova, R. Kulessa, B. Kindler, N. Kurz, B. Lommel, W. Mittig, G. Moritz, C. Mühle, J. A. Nolen, G. Nyman, P. Roussel-Chomaz, C. Scheidenberger, K.-H. Schmidt, G. Schrieder, B. M. Sherrill, H. Simon, K. Sümmerer, N. A. Tahir, V. Vysotsky, H. Wollnik, and A. F. Zeller. The Super-FRS project at GSI. *Nuclear Instruments and Methods in Physics Research Section B*, 204:71 – 85, 2003.

[6] J. Äystö, K.-H. Behr, J. Benlliure, A. Bracco, P. Egelhof, A. Fomichev, S. Galés, H. Geissel, T. Grahn, L. V. Grigorenko, M. N. Harakeh, R. Hayano, S. Heinz, K. Itahashi, A. Jokinen, N. Kalantar-Nayestanaki, R. Kanungo, H. Lenske, I. Mukha, G. Münzenberg, C. Nociforo, H. J. Ong, S. Pietri, M. Pfützner, W. Plaß, A. Prochazka, S. Purushothaman, T. Saito, C. Scheidenberger, H. Simon, I. Tanihata, S. Terashima, H. Toki, L. Trache, H. Weick, J. S. Winfield, M. Winkler, and V. Zamfir. Experimental program of the Super-FRS Collaboration at FAIR and developments of related instrumentation. *Nuclear Instruments and Methods in Physics Research Section B: Beam Interactions with Materials and Atoms*, 376:111 – 115, 2016.

[7] I. Mukha, A. Fomichev, V. Dunin, S. Krupko, C. Nociforo, S. Baraeva, H. Geissel, C. Scheidenberger, H. Simon, A. Gorshkov, R. Slepnev, and the S388 Collaboration. First operation of the GADAST, GAmma-ray Detector around a Secondary Target at the middle FRS: Measurements of inelastic scattering of ^{17}Ne*. *GSI Scientific Report 2012*, page 175, 2013.

[8] K. Miernik, W. Dominik, H. Czyrkowski, R. Dabrowski, A. Fomitchev, M. Golovkov, Z. Janas, W. Kuśmierz, M. Pfützner, A. Rodin, S. Stepantsov, R. Slepniev, G. M. Ter-Akopian, and R. Wolski. Optical Time Projection Chamber for imaging nuclear decays. *Nuclear Instruments and Methods in Physics Research A*, 581:194 – 197, 2007.

[9] L. V. Grigorenko, I. G. Mukha, C. Scheidenberger, and M. V. Zhukov. On two-neutron radioactivity and four-nucleon emission of exotic nuclei. *Physical Review C*, 84:021303(R), 2011.

[10] Z. Kohley, T. Baumann, D. Bazin, G. Christian, P. A. DeYoung, J. E. Finck, N. Frank, M. Jones, E. Lunderberg, B. Luther, S. Mosby, T. Nagi, J. K. Smith, J. Snyder, A. Spyrou, and M. Thoennessen. Study of two-neutron radioactivity in the decay of ^{26}O. *Physical Review Letters*, 110:152501, 2013.

[11] L. V. Grigorenko, I. G. Mukha, and M. V. Zhukov. Lifetime and fragment correlations for the two-neutron decay of ^{26}O ground state. *Physical Review Letters*, 111:042501, 2013.

[12] I. Mukha. Neutron Radioactivity. *Acta Physica Polonica B*, 45:321, 2014.

[13] P. Spiller, U. Blell, L. Bozyk, T. Eisel, E. Fischer, J. Henschel, P. Hülsmann, P. Kowina, H. Klingbeil, H. Kollmus, H.G. König, J. P. Meier, A. Mierau, C. Mühle, C. Omet, D. Ondreka, I. Pongrac, V. Plyusnin, N. Pyka, P. Rottländer, C. Roux, J. Stadlmann, B. Streicher, and S. Wilfert. FAIR SIS100 - features and status of realization. *Proceedings of IPAC2017*, pages 3320 – 3322, 2017.

[14] Ya. B. Zeldovich. The existence of new isotopes of light nuclei and the equation of state of neutrons. *Journal of Experimental and Theoretical Physics*, 38:1123, 1960.

[15] V. I. Goldansky. On neutron-deficient isotopes of light nuclei and the phenomena of proton and two-proton radioactivity. *Nuclear Physics*, 19:482 – 495, 1960.

[16] M. Pfützner, E. Badura, C. Bingham, B. Blank, M. Chartier, H. Geissel, J. Giovinazzo, L. V. Grigorenko, R. Grzywacz, M. Hellström, Z. Janas, J. Kurcewicz, A. S. Lalleman, C. Mazzocchi, I. Mukha, G. Münzenberg, C. Plettner, E. Roeckl, K. P. Rykaczewski, K. Schmidt, R. S. Simon, M. Stanoiu, and J. C. Thomas. First evidence for the two-proton decay of ^{45}Fe. *European Physics Journal A*, 14:279, 2002.

[17] J. Giovinazzo, B. Blank, M. Chartier, S. Czajkowski, A. Fleury, M. J. Lopez Jimenez, M. S. Pravikoff, J. C. Thomas, F. de Oliveira Santos, M. Lewitowicz, V. Maslov, M. Stanoiu, R. Grzywacz, M. Pfützner, C. Borcea, and B. A. Brown. Two-proton radioactivity of ^{45}Fe. *Physical Review Letters*, 89(10):102501, 2002.

[18] L. V. Grigorenko, R. C. Johnson, I. G. Mukha, I. J. Thompson, and M. V. Zhukov. Theory of two-proton radioactivity with application to ^{19}Mg and ^{48}Ni. *Physical Review Letters*, 85:22 – 25, 2000.

[19] L. V. Grigorenko, R. C. Johnson, I. G. Mukha, I. J. Thompson, and M. V. Zhukov. Two-proton radioactivity and three-body decay: General problems and theoretical approach. *Physical Review C*, 64:054002, 2001.

[20] M. Pfützner, M. Karny, L. V. Grigorenko, and K. Riisager. Radioactive decays at limits of nuclear stability. *Reviews of Modern Physics*, 84:567 – 619, 2012.

[21] M. Wang, G. Audi, F. G. Kondev, W. J. Huang, S. Naimi, and Xing Xu. The AME2016 atomic mass evaluation (II). Tables, graphs and references. *Chinese Physics C*, 41(3):030003, 2017.

[22] E. Olsen, M. Pfützner, N. Birge, M. Brown, W. Nazarewicz, and A. Perhac. Landscape of two-proton radioactivity. *Physical Review Letters*, 110:222501, 2013.

[23] B. Blank and M. J. G. Borge. Nuclear structure at the proton drip line: Advances with nuclear decay studies. *Progress in Particle and Nuclear Physics*, 4560:403 – 483, 2008.

[24] B. A. Brown. Diproton decay of nuclei on the proton drip line. *Physical Review C*, 43:R1513, 1991.

[25] W. Nazarewicz, J. Dobaczewski, T. R. Werner, J. A. Maruhn, P.-G. Reinhard, K. Rutz, C. R. Chinn, A. S. Umar, and M. R. Strayer. Structure of proton drip-line nuclei around doubly magic ^{48}Ni. *Physical Review C*, 53:740, 1996.

[26] O. V. Bochkarev, A. A. Korsheninnikov, E. A. Kuz'min, I. G. Mukha, A. A. Ogloblin, L. V. Chulkov, and G. B. Yan'kov. Two-proton decay of ^{6}Be. *JETP Letters*, 40:969 – 972, 1984. [Pis'ma Zh. Eksp. Teor. Fiz., 40:204-207, 1984].

[27] O. V. Bochkarev, A. A. Korsheninnikov, E. A. Kuz'min, I. G. Mukha, L. V. Chulkov, and G. B. Yan'kov. Exotic decay modes of ^{6}Be in a kinematically complete experiment. *JETP Letters*, 48:133 – 136, 1988. [Pis'ma Zh. Eksp. Teor. Fiz., 48:124-127, 1988].

[28] G. J. KeKelis, M. S. Zisman, D. K. Scott, R. Jahn, D. J. Vieira, Joseph Cerny, and F. Ajzenberg-Selove. Masses of the unbound nuclei ^{16}Ne, ^{15}F, and ^{12}O. *Physical Review C*, 17:1929 – 1938, 1978.

[29] R. A. Kryger, A. Azhari, M. Hellström, J. H. Kelley, T. Kubo, R. Pfaff, E. Ramakrishnan, B. M. Sherrill, M. Thoennessen, S. Yokoyama, R. J. Charity, J. Dempsey, A. Kirov, N. Robertson, D. G. Sarantites, L. G. Sobotka, and J. A. Winger. Two-proton emission from the ground state of ^{12}O. *Physical Review Letters*, 74:860, 1995.

[30] I. Mukha, L. Grigorenko, K. Sümmerer, L. Acosta, M. A. G. Alvarez, E. Casarejos, A. Chatillon, D. Cortina-Gil, J. M. Espino, A. Fomichev, J. E. García-Ramos, H. Geissel, J. Gómez-Camacho, J. Hofmann, O. Kiselev, A. Korsheninnikov, N. Kurz, Yu. Litvinov, I. Martel, C. Nociforo, W. Ott, M. Pfützner, C. Rodríguez-Tajes, E. Roeckl, M. Stanoiu, H. Weick, and P. J. Woods. Proton-proton correlations observed in two-proton decay of ^{19}Mg and ^{16}Ne. *Physical Review C*, 77:061303(R), 2008.

[31] O. V. Bochkarev, L. V. Chulkov, A. A. Korsheninnikov, E. A. Kuz'min, I. G. Mukha, and G. B. Yankov. Democratic decay of ^{6}Be states. *Nuclear Physics A*, 505:215, 1989.

[32] I. A. Egorova, R. J. Charity, L. V. Grigorenko, Z. Chajecki, D. Coupland, J. M. Elson, T. K. Ghosh, M. E. Howard, H. Iwasaki, M. Kilburn, Jenny Lee, W. G. Lynch, J. Manfredi, S. T. Marley, A. Sanetullaev, R. Shane, D. V. Shetty, L. G. Sobotka, M. B. Tsang, J. Winkelbauer, A. H. Wuosmaa, M. Youngs, and M. V. Zhukov. Democratic decay of ^{6}Be exposed by correlations. *Physical Review Letters*, 109:202502, 2012.

[33] L. V. Grigorenko. Theoretical study of two-proton radioactivity. Status and predictions and applications. *Physics of Particles and Nuclei*, 40:674 – 714, 2009.

[34] T. B. Webb, S. M. Wang, K. W. Brown, R. J. Charity, J. M. Elson, J. Barney, G. Cerizza, Z. Chajecki, J. Estee, D. E. M. Hoff, S. A. Kuvin, W. G. Lynch, J. Manfredi, D. McNeel, P. Morfouace, W. Nazarewicz, C. D. Pruitt, C. Santamaria, J. Smith, L. G. Sobotka, S. Sweany, C. Y. Tsang, M. B. Tsang, A. H. Wuosmaa, Y. Zhang, and K. Zhu. First observation of unbound ^{11}O, the mirror of the halo nucleus ^{11}Li. *Physical Review Letters*, 122:122501, 2019.

[35] S. M. Wang, N. Michel, W. Nazarewicz, and F. R. Xu. Structure and decays of nuclear three-body systems: The Gamow coupled-channel method in Jacobi coordinates. *Physical Review C*, 96:044307, 2017.

[36] M. F. Jager, R. J. Charity, J. M. Elson, J. Manfredi, M. H. Mahzoon, L. G. Sobotka, M. McCleskey, R. G. Pizzone, B. T. Roeder, A. Spiridon, E. Simmons, L. Trache, and M. Kurokawa. Two-proton decay of ^{12}O and its isobaric analog state in ^{12}N. *Physical Review C*, 86:011304, 2012.

[37] L. V. Grigorenko, I. G. Mukha, I. J. Thompson, and M. V. Zhukov. Two-proton widths of ^{12}O, ^{16}Ne, and three-body mechanism of Thomas-Ehrman shift. *Physical Review Letters*, 88:042502, 2002.

[38] K. W. Brown, R. J. Charity, L. G. Sobotka, Z. Chajecki, L. V. Grigorenko, I. A. Egorova, Yu. L. Parfenova, M. V. Zhukov, S. Bedoor, W. W. Buhro, J. M. Elson, W. G. Lynch, J. Manfredi, D. G. McNeel, W. Reviol, R. Shane, R. H. Showalter,

M. B. Tsang, J. R. Winkelbauer, and A. H. Wuosmaa. Observation of long-range three-body coulomb effects in the decay of ^{16}Ne. *Physical Review Letters*, 113:232501, 2014.

[39] L. V. Grigorenko, I. G. Mukha, and M. V. Zhukov. Prospective candidates for the two-proton decay studies I: structure and coulomb energies of ^{17}Ne and ^{19}Mg. *Nuclear Physics A*, 713(3):372 – 389, 2003.

[40] L. V. Grigorenko, R. C. Johnson, I. G. Mukha, I. J. Thompson, and M. V. Zhukov. Three-body decays of light nuclei: ^{6}Be, ^{8}Li, ^{9}Be, ^{12}O, ^{16}Ne and ^{17}Ne. *European Physical Journal A*, 15:125, 2002.

[41] M. J. Chromik, B. A. Brown, M. Fauerbach, T. Glasmacher, R. Ibbotson, H. Scheit, M. Thoennessen, and P. G. Thirolf. Excitation and decay of the first excited state of ^{17}Ne. *Physical Review C*, 55:1676, 1997.

[42] M. J. Chromik, P. G. Thirolf, M. Thoennessen, B. A. Brown, T. Davinson, D. Gassmann, P. Heckman, J. Prisciandaro, P. Reiter, E. Tryggestad, and P. J. Woods. Two-proton spectroscopy of low-lying states in ^{17}Ne. *Physical Review C*, 66:024313, 2002.

[43] P. G. Sharov, A. S. Fomichev, A. A. Bezbakh, V. Chudoba, I. A. Egorova, M. S. Golovkov, T. A. Golubkova, A. V. Gorshkov, L. V. Grigorenko, G. Kaminski, A. G. Knyazev, S. A. Krupko, M. Mentel, E. Yu. Nikolskii, Yu. L. Parfenova dn P. Pluchinski, S. A. Rymzhanova, S. I. Sidorchuk, R. S. Slepnev, S. V. Stepantsov, G. M. Ter-Akopian, and R. Wolski. Search of $2p$ decay of the first excited state of ^{17}Ne. *Physical Review C*, 96:025807, 2017.

[44] E. Garrido, D. V. Fedorov, and A. S. Jensen. Three-body structure of the low-lying ^{17}Ne-states. *Nuclear Physics A*, 733:85, 2004.

[45] I. Mukha, K. Sümmerer, L. Acosta, M. A. G. Alvarez, E. Casarejos, A. Chatillon, D. Cortina-Gil, J. Espino, A. Fomichev, J. E. Garcia-Ramos, H. Geissel, J. Gomez-Camacho, L. Grigorenko, J. Hofmann, O. Kiselev, A. Korsheninnikov, N. Kurz, Yu. Litvinov, I. Martel, C. Nociforo, W. Ott, M. Pfützner, C. Rodriguez-Tajes, E. Roeckl, M. Stanoiu, H. Weick, and P. J. Woods. Observation of two-proton radioactivity of ^{19}Mg by tracking the decay products. *Physical Review Letters*, 99:182501, 2007.

[46] I. Mukha, L. V. Grigorenko, X. Xu, L. Acosta, E. Casarejos, A. A. Ciemny, W. Dominik, J. Duénas-Díaz, V. Dunin, J. M. Espino, A. Estradé, F. Farinon, A. Fomichev, H. Geissel, T. A. Golubkova, A. Gorshkov, Z. Janas, G. Kamiński, O. Kiselev, R. Knöbel, S. Krupko, M. Kuich, Yu. A. Litvinov, G. Marquinez-Durán, I. Martel, C. Mazzocchi, C. Nociforo, A. K. Ordúz, M. Pfützner, S. Pietri, M. Pomorski, A. Prochazka, S. Rymzhanova, A. M. Sánchez-Benítez, C. Scheidenberger, P. Sharov, H. Simon, B. Sitar, R. Slepnev, M. Stanoiu, P. Strmen, I. Szarka, M. Takechi, Y. K. Tanaka, H. Weick, M. Winkler, J. S. Winfield, and M. V. Zhukov. Observation and spectroscopy of new proton-unbound isotopes ^{30}Ar and ^{29}Cl: An interplay of prompt two-proton and sequential decay. *Physical Review Letters*, 115:202501, 2015.

[47] L. V. Grigorenko, I. G. Mukha, and M. V. Zhukov. Prospective candidates for the two-proton decay studies. II: exploratory studies of ^{30}Ar and ^{34}Ca and ^{45}Fe. *Nuclear Physics A*, 714:425, 2003.

[48] C. Dossat, A. Bey, B. Blank, G. Canchel, A. Fleury, J. Giovinazzo, I. Matea, F. de Oliveira Santos, G. Georgiev, S. Grevy, I. Stefan, J. C. Thomas, N. Adimi, C. Borcea, D. Cortina, M. Caamano, M. Stanoiu, F. Aksouh, B. A. Brown, and L. V. Grigorenko. Two-proton radioactivity studies with ^{45}Fe and ^{48}Ni. *Physical Review C*, 72:054315, 2005.

[49] M. Pomorski, M. Pfützner, W. Dominik, R. Grzywacz, T. Baumann, J. S. Berryman, H. Czyrkowski, R. Dabrowski, T. Ginter, J. Johnson, G. Kamiński, A. Kuźniak, N. Larson, S. N. Liddick, M. Madurga, C. Mazzocchi, S. Mianowski, K. Miernik, D. Miller, S. Paulauskas, J. Pereira, K. P. Rykaczewski, A. Stolz, and S. Suchyta. First observation of two-proton radioactivity in ^{48}Ni. *Physical Review C*, 83:061303, 2011.

[50] M. Pomorski, M. Pfützner, W. Dominik, R. Grzywacz, A. Stolz, T. Baumann, J. S. Berryman, H. Czyrkowski, R. Dąbrowski, A. Fijałkowska, T. Ginter, J. Johnson, G. Kamiński, N. Larson, S. N. Liddick, M. Madurga, C. Mazzocchi, S. Mianowski, K. Miernik, D. Miller, S. Paulauskas, J. Pereira, K. P. Rykaczewski, and S. Suchyta. Proton spectroscopy of ^{48}Ni, ^{46}Fe, and ^{44}Cr. *Physical Review C*, 90:014311, 2014.

[51] B. Blank, A. Bey, G. Canchel, C. Dossat, A. Fleury, J. Giovinazzo, I. Matea, N. Adimi, F. De Oliveira, I. Stefan, G. Georgiev, S. Grevy, J. C. Thomas, C. Borcea, D. Cortina, M. Caamano, M. Stanoiu, F. Aksouh, B. A. Brown, F. C. Barker, and W. A. Richter. First observation of ^{54}Zn and its decay by two-proton emission. *Physical Review Letters*, 94:232501, 2005.

[52] P. Ascher, L. Audirac, N. Adimi, B. Blank, C. Borcea, B. A. Brown, I. Companis, F. Delalee, C. E. Demonchy, F. de Oliveira Santos, J. Giovinazzo, S. Grévy, L. V. Grigorenko, T. Kurtukian-Nieto, S. Leblanc, J.-L. Pedroza, L. Perrot, J. Pibernat, L. Serani, P. C. Srivastava, and J.-C. Thomas. Direct observation of two protons in the decay of ^{54}Zn. *Physical Review Letters*, 107:102502, 2011.

[53] L. V. Grigorenko and M. V. Zhukov. Two-proton radioactivity and three-body decay. II. Exploratory studies of lifetimes and correlations. *Physical Review C*, 68:054005, 2003.

[54] T. Goigoux, P. Ascher, B. Blank, M. Gerbaux, J. Giovinazzo, S. Grévy, T. Kurtukian Nieto, C. Magron, P. Doornenbal, G. G. Kiss, S. Nishimura, P.-A. Söderström, V. H. Phong, J. Wu, D. S. Ahn, N. Fukuda, N. Inabe, T. Kubo, S. Kubono, H. Sakurai, Y. Shimizu, T. Sumikama, H. Suzuki, H. Takeda, J. Agramunt, A. Algora, V. Guadilla, A. Montaner-Piza, A. I. Morales, S. E. A. Orrigo, B. Rubio, Y. Fujita, M. Tanaka, W. Gelletly, P. Aguilera, F. Molina, F. Diel, D. Lubos, G. de Angelis, D. Napoli, C. Borcea, A. Boso, R. B. Cakirli, E. Ganioglu, J. Chiba, D. Nishimura, H. Oikawa, Y. Takei, S. Yagi, K. Wimmer, G. de France, S. Go, and B. A. Brown. Two-proton radioactivity of ^{67}Kr. *Physical Review Letters*, 117:162501, 2016.

[55] L. V. Grigorenko, T. A. Golubkova, J. S. Vaagen, and M. V. Zhukov. Decay mechanism and lifetime of ^{67}Kr. *Physical Review C*, 95:021601, 2017.

[56] A. Azhari, R. A. Kryger, and M. Thoennessen. Decay of the ^{12}O ground state. *Physical Review C*, 58:2568 – 2570, 1998.

[57] C. Détraz. The branching ratio of β-delayed two-proton emission. *Zeitschrift für Physik A - Hadrons and Nuclei*, 340:227 – 230, 1991.

[58] D. M. Moltz, J. C. Batchelder, T. F. Lang, T. J. Ognibene, Joseph Cerny, P. E. Haustein, and P. L. Reeder. Beta-delayed two-proton decay of ^{39}Ti. *Zeitschrift für Physik A - Hadrons and Nuclei*, 342:273 – 276, 1991.

[59] H. O. U. Fynbo, M. J. G.Borge, L. Axelsson, J. Äystö, U. C. Bergmann, L. M. Fraile, A. Honkanen, P. Hornshøj, Y. Jading, A. Jokinen, B. Jonson, I. Martel, I. Mukha, T. Nilsson, G. Nyman, M. Oinonen, I. Piqueras, K. Riisager, T. Siiskonen, M. H. Smedberg, O. Tengblad, J. Thaysen, F. Wenander, and ISOLDE Collaboration. The β2p decay mechanism of ^{31}Ar. *Nuclear Physics A*, 677:38 – 60, 2000.

[60] C. R. Bain, P. J. Woods, R. Coszach, T. Davinson, P. Decrock, M. Gaelens, W. Galster, M. Huyse, R. J. Irvine, P. Leleux, E. Lienard, M. Loiselet, C. Michotte, R. Neal, A. Ninane, G. Ryckewaert, A. C. Shotter, G. Vancraeynest, J. Vervier, and J. Wauters. Two Proton Emission Induced via a Resonance Reaction. *Physics Letter B*, 373:35, 1996.

[61] F. de Oliveira Santos, P. Himpe, M. Lewitowicz, I. Stefan, N. Smirnova, N. L. Achouri, J. C. Angélique, C. Angulo, L. Axelsson, D. Baiborodin, F. Becker, M. Bellegui, E. Berthoumieux, B. Blank, C. Borcea, A. Cassimi, J. M. Daugas, G. de France, F. Dembinski, C. E. Demonchy, Z. Dlouhy, P. Dolégiéviez, C. Donzaud, G. Georgiev, L. Giot, S. Grévy, D. Guillemaud Mueller, V. Lapoux, E. Liénard, M. J. Lopez Jimenez, K. Markenroth, I. Matea, W. Mittig, F. Negoita, G. Neyens, N. Orr, F. Pougheon, P. Roussel Chomaz, M. G. Saint Laurent, F. Sarazin, H. Savajols, M. Sawicka, O. Sorlin, M. Stanoiu, C. Stodel, G. Thiamova, D. Verney, and A. C. C. Villari. Study of ^{19}Na at SPIRAL. *The European Physical Journal A - Hadrons and Nuclei*, 24:237 – 247, 2005.

[62] L. V. Grigorenko and M. V. Zhukov. Three-body resonant radioactive capture reactions in astrophysics. *Physical Review C*, 72:015803, 2005.

[63] L. V. Grigorenko, Yu. L. Parfenova, and M. V. Zhukov. Possibility to study a two-proton halo in ^{17}Ne. *Physical Review C*, 71:051604, 2005.

[64] L. V. Grigorenko, K. Langanke, N. B. Shul'gina, and M. V. Zhukov. Soft dipole mode in ^{17}Ne and the astrophysical $2p$ capture on ^{15}O. *Physics Letters B*, 641:254, 2006.

[65] O. M. Sukhareva, L. V. Grigorenko, D. A. Kostyleva, and M. V. Zhukov. Studying the validity of the quasi-classical approach to three-body decays. *Bulletin of Russian Academy of Sciences: Physics*, 84:461 – 464, 2019.

[66] I. Mukha, E. Roeckl, L. Batist, A. Blazhev, J. Döring, H. Grawe, L. Grigorenko, M. Huyse, Z. Janas, R. Kirchner, M. La Commara, C. Mazzocchi, S.L. Tabor, and P. Van Duppen. Proton-proton correlations observed in two-proton radioactivity of ^{94}Ag. *Nature*, 439:298 – 302, 2006.

[67] A. Kankainen, V.-V. Elomaa, L. Batist, S. Eliseev, T. Eronen, U. Hager, J. Hakala, A. Jokinen, I. D. Moore, Yu. N. Novikov, H. Penttila, A. Popov, S. Rahaman, S. Rinta-Antila, J. Rissanen, A. Saastamoinen, D. M. Seliverstov, T. Sonoda, G. Vorobjev, C. Weber, and J. Aysto. Mass measurements and implications for the energy of the high-spin isomer in ^{94}Ag. *Physical Review Letters*, 101:142503, 2008.

[68] J. Cerny, D. M. Moltz, D. W. Lee, K. Perajarvi, B. R. Barquest, L. E. Grossman, W. Jeong, and C. C. Jewett. Reinvestigation of the direct two-proton decay of the long-lived isomer ^{94}Ag^{m} [0.4 s, 6.7 MeV, (21^{+})]. *Physical Review Letters*, 103:152502, 2009.

[69] O. L. Pechenaya, C. J. Chiara, D. G. Sarantites, W. Reviol, R. J. Charity, M. P. Carpenter, R. V. F. Janssens, T. Lauritsen, C. J. Lister, D. Seweryniak, S. Zhu, L.-L. Andersson, E. K. Johansson, and D. Rudolph. Level structure of ^{92}Rh: Implications for the two-proton decay of ^{94}Ag^{m}. *Physical Review C*, 76:011304(R), 2007.

[70] I. Mukha, H. Grawe, E. Roeckl, and S. Tabor. Comment on "Level structure of ^{92}Rh: Implications for the two-proton decay of ^{94}Ag^{m}". *Physical Review C*, 78:039803, 2008.

[71] J. Giovinazzo, B. Blank, C. Borcea, G. Canchel, J. C. Dalouzy, C. E. Demonchy, F. de Oliveira Santos, C. Dossat, S. Grevy, L. Hay, J. Huikari, S. Leblanc, I. Matea, J. L. Pedroza, L. Perrot, J. Pibernat, L. Serani, C. Stodel, and J.-C. Thomas. First direct observation of two protons in the decay of ^{45}Fe with a time-projection chamber. *Physical Review Letters*, 99:102501, 2007.

[72] K. Miernik, W. Dominik, Z. Janas, M. Pfützner, L. Grigorenko, C. Bingham, H. Czyrkowski, M. Cwiok, I. Darby, R. Dabrowski, T. Ginter, R. Grzywacz, M. Karny, A. Korgul, W. Kusmierz, S. Liddick, M. Rajabali, K. Rykaczewski, and A. Stolz. Studies of charged particle emission in the decay of ^{45}Fe. *Acta Physica Polonica B*, 39:477, 2008.

[73] K. Miernik, W. Dominik, Z. Janas, M. Pfützner, L. Grigorenko, C. R. Bingham, H. Czyrkowski, M. Cwiok, I. G. Darby, R. Dabrowski, T. Ginter, R. Grzywacz, M. Karny, A. Korgul, W. Kusmierz, S. N. Liddick, M. Rajabali, K. Rykaczewski, and A. Stolz. Two-proton correlations in the decay of ^{45}Fe. *Physical Review Letters*, 99:192501, 2007.

[74] L. V. Grigorenko and M. V. Zhukov. Two-proton radioactivity and three-body decay. III. Integral formulas for decay widths in a simplified semianalytical approach. *Physical Review C*, 76:014008, 2007.

[75] I. Mukha and G. Schrieder. Two-proton radioactivity as a genuine three-body decay: the ^{19}Mg probe. *Nuclear Physics A*, 690:280 – 283, 2001.

[76] International Conference on Proton-Emitting Nuclei 2019 (PROCON-2019). *https://people.nscl.msu.edu/~brown/procon-2019/procon-talks/*, 2019.

[77] I. Mukha, L. Grigorenko, L. Acosta, M. A. G. Alvarez, E. Casarejos, A. Chatillon, D. Cortina-Gil, J. M. Espino, A. Fomichev, J. E. García-Ramos, H. Geissel, J. Gómez-Camacho, J. Hofmann, O. Kiselev, A. Korsheninnikov, N. Kurz, Yu. A. Litvinov, I. Martel, C. Nociforo, W. Ott, M. Pfützner, C. Rodríguez-Tajes, E. Roeckl, C. Scheidenberger, M. Stanoiu, K. Sümmerer, H. Weick, and P. J. Woods. New states in ^{18}Na and ^{19}Mg observed in the two-proton decay of ^{19}Mg. *Physical Review C*, 85:044325, 2012.

[78] D. Kostyleva, D. Mukha, L. Acosta, E. Casarejos, V. Chudoba, A. A. Ciemny, W. Dominik, J. A. Dueñas, V. Dunin, J. M. Espino, A. Estradé, F. Farinon, A. Fomichev, H. Geissel, A. Gorshkov, L. V. Grigorenko, Z. Janas, G. Kamiński, O. Kiselev, R. Knöbel, S. Krupko, M. Kuich, Yu. A. Litvinov, G. Marquinez-Durán, I. Martel, C. Mazzocchi, E. Yu. Nikolskii, C. Nociforo, A. K. Ordúz, M. Pfützner, S. Pietri, M. Pomorski, A. Prochazka, S. Rymzhanova, A. M. Sánchez-Benítez, C. Scheidenberger, H. Simon, B. Sitar, R. Slepnev, M. Stanoiu, P. Strmen, I. Szarka, M. Takechi, Y. K. Tanaka, H. Weick, M. Winkler, J. S. Winfield, X. Xu, and M. V. Zhukov. Towards the Limits of Existence of Nuclear Structure: Observation and First Spectroscopy of the Isotope ^{31}K by Measuring Its Three-Proton decay. *Physical Review Letters*, 123:092502, 2019.

[79] I. Mukha, L. V. Grigorenko, D. Kostyleva, L. Acosta, E. Casarejos, A. A. Ciemny, W. Dominik, J. A. Dueñas, V. Dunin, J. M. Espino, A. Estradé, F. Farinon, A. Fomichev, H. Geissel, A. Gorshkov, Z. Janas, G. Kamiński, O. Kiselev, R. Knöbel, S. Krupko, M. Kuich, Yu. A. Litvinov, G. Marquinez-Durán, I. Martel, C. Mazzocchi, C. Nociforo, A. K. Ordúz, M. Pfützner, S. Pietri, M. Pomorski, A. Prochazka, S. Rymzhanova, A. M. Sánchez-Benítez, C. Scheidenberger, P. Sharov, H. Simon, B. Sitar, R. Slepnev, M. Stanoiu, P. Strmen, I. Szarka, M. Takechi, Y. K. Tanaka, H. Weick, M. Winkler, J. S. Winfield, X. Xu, and M. V. Zhukov. Deep excursion beyond the proton dripline. I. Argon and Chlorine isotope chains. *Physical Review C*, 98:064308, 2018.

[80] R. J. Charity, J. M. Elson, J. Manfredi, R. Shane, L. G. Sobotka, Z. Chajecki, D. Coupland, H. Iwasaki, M. Kilburn, J. Lee, W. G. Lynch, A. Sanetullaev, M. B. Tsang, J. Winkelbauer, M. Youngs, S. T. Marley, D. V. Shetty, A. H. Wuosmaa, T. K. Ghosh, and M. E. Howard. $2p$-$2p$ decay of ^{8}C and isospin-allowed $2p$ decay of the isobaric-analog state in ^{8}B. *Physical Review C*, 82:041304(R), 2010.

[81] G. I. Kopylov. Foundations of kinematics of resonances. *Publishing house "Nauka", Moscow*, 1970.

[82] A. M. Baldin, V. I. Goldanskii, and I. L. Rozenthal. Kinematics of nuclear reactions. *Pergamon Press, Oxford*, 1961.

[83] T. B. Webb, R. J. Charity, J. M. Elson, D. E. M. Hoff, C. D. Pruitt, L. G. Sobotka, K. W. Brown, J. Barney, G. Cerizza, J. Estee, G. Jhang, W. G. Lynch, J. Manfredi, P. Morfouace, C. Santamaria, S. Sweany, M. B. Tsang, T. Tsang,

S. M. Wang, Y. Zhang, K. Zhu, S. A. Kuvin, D. McNeel, J. Smith, A. H. Wuosmaa, and Z. Chajecki. Particle decays of levels in ^{11,12}N and ^{12}O investigated with the invariant-mass method. *Physical Review C*, 100:024306, 2019.

[84] I. G. Mukha. Two-Proton Radioactivity Search. *Physics of Atomic Nuclei*, 66:1519 – 1522, 2003.

[85] I. Mukha, K. Sümmerer, L. Acosta, M. A. G. Alvarez, E. Casarejos, A. Chatillon, D. Cortina-Gil, I. A. Egorova, J. M. Espino, A. Fomichev, J. E. García-Ramos, H. Geissel, J. Gómez-Camacho, L. Grigorenko, J. Hofmann, O. Kiselev, A. Korsheninnikov, N. Kurz, Yu. A. Litvinov, E. Litvinova, I. Martel, C. Nociforo, W. Ott, M. Pfützner, C. Rodríguez-Tajes, E. Roeckl, M. Stanoiu, N. K. Timofeyuk, H. Weick, and P. J. Woods. Spectroscopy of proton-unbound nuclei by tracking their decay products in-flight: One- and two- proton decays of ^{15}F, ^{16}Ne and ^{19}Na. *Physical Review C*, 82:054315, 2010.

[86] X.-D. Xu, I. Mukha, L. V. Grigorenko, C. Scheidenberger, L. Acosta, E. Casarejos, V. Chudoba, A. A. Ciemny, W. Dominik, J. Duénas-Díaz, V. Dunin, J. M. Espino, A. Estradé, F. Farinon, A. Fomichev, H. Geissel, T. A. Golubkova, A. Gorshkov, Z. Janas, G. Kamiński, O. Kiselev, R. Knöbel, S. Krupko, M. Kuich, Yu. A. Litvinov, G. Marquinez-Durán, I. Martel, C. Mazzocchi, C. Nociforo, A. K. Ordúz, M. Pfützner, S. Pietri, M. Pomorski, A. Prochazka, S. Rymzhanova, A. M. Sánchez-Benítez, P. Sharov, H. Simon, B. Sitar, R. Slepnev, M. Stanoiu, P. Strmen, I. Szarka, M. Takechi, Y. K. Tanaka, H. Weick, M. Winkler, and J. S. Winfield. Spectroscopy of excited states of unbound nuclei ^{30}Ar and ^{29}Cl. *Physical Review C*, 97:034305, 2018.

[87] N. Angert and C. Schmelzer. The UNILAC, a variable energy linear accelerator for atomic ions of any mass. *Kerntech*, 11:690 – 695, 1969.

[88] M. Steiner, K. Blasche, H.-G. Clerc, H. Eickhoff, B. Franczak, H. Geissel, G. Münzenberg, K.-H. Schmidt, H. Stelzer, and K. Sümmerer. Preliminary measurements of SIS-18 beam parameters. *Nuclear Instruments and Methods in Physics Research Section A: Accelerators, Spectrometers, Detectors and Associated Equipment*, 312(3):420 – 424, 1992.

[89] W. R. Plass, T. Dickel, S. Purushothaman, P. Dendooven, H. Geissel, J. Ebert, E. Haettner, C. Jesch, M. Ranjan, M. P. Reiter, H. Weick, F. Amjad, S. Ayet, M. Diwisch, A. Estrade, F. Farinon, F. Greiner, N. Kalantar-Nayestanaki, R. Knöbel, J. Kurcewicz, J. Lang, I. Moore, I. Mukha, C. Nociforo, M. Petrick, M. Pfützner, S. Pietri, A. Prochazka, A.-K. Rink, S. Rinta-Antila, D. Schäfer, C. Scheidenberger, M. Takechi, Y. K. Tanaka, J. S. Winfield, and M. I. Yavor. The FRS Ion Catcher - a facility for high-precision experiments with stopped projectile and fission fragments. *Nuclear Instruments and Methods in Physics Research Section B: Beam Interactions with Materials and Atoms*, 317:457 – 462, 2013.

[90] B. Franzke. The heavy ion storage and cooler ring project ESR at GSI. *Nuclear Instruments and Methods in Physics Research Section B: Beam Interactions with Materials and Atoms*, 24 - 25:18 – 25, 1987.

[91] H. Geissel, G. Münzenberg, and C. Scheidenberger. 25 years of FRS experiments and new horizons. *FIAS Interdisciplinary Science Series*, 2:55 – 79, 2017.

[92] M. Berz, B. Hartmann, K. Lindemann, A. Magel, and H. Weick. GICOSY ion optics program. *http://web-docs.gsi.de/~weick/gicosy/*.

[93] B. Franczak. Simulation programme MIRKO, GSI Darmstadt. *http://www-linux.gsi.de/~redelbac/MIRKO/*.

[94] O. B. Tarasov and D. Bazin. LISE++: radioactive beam production with in-flight separators. *Nuclear Instruments and Methods in Physics Research B*, 266:4657 – 4664, 2008.

[95] The GSI fragment separator website. *https://www-win.gsi.de/frs/technical/FRSsetup/detectors-new.asp*.

[96] R. Janik, A. Prochazka, B. Sitar, P. Strmen, I. Szarka, H. Geissel, K.-H. Behr, C. Karagiannis, C. Nociforo, H. Weick, and M. Winkler. Time Projection Chambers with C-pads for heavy ion tracking. *Nuclear Instruments and Methods in Physics Research A*, 640:54 – 57, 2011.

[97] R. Schneider and A. Stolz. Technical Manual Ionization Chamber MUSIC80. *https://www-win.gsi.de/frs/technical/FRSsetup/detectors/music80*, 2000.

[98] J. Adamczewski-Musch, N. Kurz, and S. Linev. Status and developments for DAQ system, MBS v6.3. *GSI Scientific Report 2014*, 2015.

[99] Aplha Magnetic Spectormeter AMS-02. *https://www.nasa.gov/mission_pages/station/research/alpha-magnetic-spectrometer.html*.

[100] B. Alpat, G. Ambrosi, C. Balboni, R. Battiston, A. Biland, M. Bourquin, W. J. Burger, Y. H. Chang, A. E. Chen, N. Dinu, P. Extermann, E. Fiandrini, S. R. Hou, M. Ionica, R. Ionica, W. T. Lin, W. Lustermann, G. Maehlum, M. Menichelli, M. Pauluzzi, N. Produit, D. Rapin, D. Ren, M. Ribordy, H. Sann, D. Schardt, K. Sümmerer, G. Viertel, D. Vité, W. Wallra, and S. X. Wu. High-precision tracking and charge selection with silicon strip detectors for relativistic ions. *Nuclear Instruments and Methods in Physics Research A*, 446:522 – 535, 2000.

[101] B. Alpat, G. Ambrosi, Ph. Azzarello, R. Battiston, P. Bene, B. Bertucci, S. Bizzaglia, M. Bizzarri, S. Blasko, M. Bourquin, Ph. Bouvier, W. J. Burger, M. Capell, C. Cecchi, Y. H. Chang, E. Cortina, N. Dinu, G. Esposito, E. Fiandrini, D. Haas, H. Hakobyan, M. Ionica, R. Ionica, A. Kounine, V. Koutsenko, A. Lebedev, C. Lechanoine-Leluc, C. H. Lin, F. Masciocchi, M. Menichelli, S. Natale, M. Paniccia, A. Papi, M. Pauluzzi, E. Perrin, M. Pohl, D. Rapin, J. P. Richeux, W. Wallraff, M. Willenbrock, and P. Zuccon. Charge determination of nuclei with the AMS-02 silicon tracker. *Nuclear Instruments and Methods in Physics Research A*, 540:121 – 130, 2005.

[102] P. Azzarello. Tests and production of the AMS-02 silicon tracker detectors. *PhD thesis, Geneve University*, 2004.

[103] O. Toker, S. Masciocchi, E. Nygard, A. Ritdge, and P. Weilhammer. VIKING, a CMOS low noise monolithic 128 channel frontend for Si-strip detector readout. *Nuclear Instruments and Methods in Physics Research A*, 340:572 – 579, 1994.

[104] J. Hoffmann, N. Kurz, and W. Ott. SIlicon Strip DEtector REadout Module. *https://www.gsi.de/fileadmin/EE/Module/Dokumente/SIDEREM2.pdf*, 2007.

[105] J. Hoffmann. SAM5 module. *https://www.gsi.de/fileadmin/EE/Module/Dokumente/SAM5_03.pdf*, 2006.

[106] X. Xu. Observation and Investigation of the New Proton-Unbound Nuclei ^{30}Ar and ^{29}Cl with In-Flight Decay Spectroscopy. *PhD thesis, Justus-Liebig-Universität Giessen*, 2016.

[107] I. Mukha for the S271 Collaboration. Experimental studies of nuclei beyond the proton drip line by tracking technique. *European Physical Journal A*, 42:421 – 429, 2009.

[108] I. Mukha, N. K. Timofeyuk, K. Sümmerer, L. Acosta, M. A. G. Alvarez, E. Casarejos, A. Chatillon, D. Cortina-Gil, J. M. Espino, A. Fomichev, J. E. García-Ramos, H. Geissel, J. Gómez-Camacho, L. Grigorenko, J. Hofmann, O. Kiselev, A. Korsheninnikov, N. Kurz, Yu. Litvinov, I. Martel, C. Nociforo, W. Ott, M. Pfützner, C. Rodríguez-Tajes, E. Roeckl, M. Stanoiu, H. Weick, and P. J. Woods. Observation of narrow states in nuclei beyond the proton drip line: ^{15}F and ^{16}Ne. *Physical Review C*, 79:061301, 2009.

[109] Geant 4 - simulation tool. *https://geant4.web.cern.ch/*.

[110] I. M. Chakravarti, R. G. Laha, and J. Roy. *Handbook of Methods of Applied Statistics*, I:392 – 394, 1967.

[111] C. Ouellet and B. Singh. Nuclear data sheets for A = 31. *Nuclear Data Sheets*, 114(2):209 – 396, 2013.

[112] L. Axelsson, J. Aysto, U. C. Bergmann, M. J. G. Borge, L. M. Fraile, H. O. U. Fynbo, A. Honkanen, P. Hornshoj, A. Jokinen, B. Jonson, I. Martel, I. Mukha, T. Nilsson, G. Nyman, B. Petersen, K. Riisager, M. H. Smedberg, and O. Tengblad. Two-proton emission in the decay of ^{31}Ar. *Nuclear Physics A*, 628(3):345 – 362, 1998.

[113] V. Borrel, J. C. Jacmart, F. Pougheon, R. Anne, C. Detraz, D. Guillemaud-Mueller, A. C. Mueller, D. Bazin, R. Del Moral]and J. P. Dufour, F. Hubert, M. S. Pravikoff, and E. Roeckl. ^{31}Ar and ^{27}S: Beta-delayed two-proton emission and mass excess. *Nuclear Physics A*, 531(2):353 – 369, 1991.

[114] A. A. Lis, C. Mazzocchi, W. Dominik, Z. Janas, M. Pfützner, M. Pomorski, L. Acosta, S. Baraeva, E. Casarejos, J. Duénas-Díaz, V. Dunin, J. M. Espino, A. Estrade, F. Farinon, A. Fomichev, H. Geissel, A. Gorshkov, G. Kamiński, O. Kiselev, R. Knöbel, S. Krupko, M. Kuich, Yu. A. Litvinov, G. Marquinez-Durán, I. Martel, I. Mukha, C. Nociforo, A. K. Ordúz, S. Pietri, A. Prochazka, A. M. Sánchez-Benítez, H. Simon, B. Sitar, R. Slepnev, M. Stanoiu, P. Strmen,

I. Szarka, M. Takechi, Y. Tanaka, H. Weick, and J. S. Winfield. β-delayed three-proton decay of ^{31}Ar. *Physical Review C*, 91:064309, 2015.

[115] D. Bazin, R. Del Moral, J. P. Dufour, A. Fleury, F. Hubert, M. S. Pravikoff, R. Anne, P. Bricault, C. Détraz, M. Lewitowicz, Y. Zheng, D. Guillemaud-Mueller, J. C. Jacmart, A. C. Mueller, F. Pougheon, and A. Richard. Decay modes of ^{31}Ar and first observation of β-delayed three-proton radioactivity. *Physical Review C*, 45:69 – 79, 1992.

[116] R. G. Thomas. An analysis of the energy levels of the mirror nuclei, ^{13}C and ^{13}N. *Physical Review*, 88:1109 – 1125, 1952.

[117] J. B. Ehrman. On the displacement of corresponding energy levels of ^{13}C and ^{13}N. *Physical Review*, 81:412 – 416, 1951.

[118] A. Magilligan and B. A. Brown. New isospin-breaking "USD" Hamiltonians for the *sd* shell. *Physical Review C*, 101:064312, 2020.

[119] D. Kostyleva for the EXPERT/Super-FRS Experiment Collaboration of FAIR. Exploration of nuclear structure along the proton-unbound Argon and Chlorine isotopes. *Acta Physica Polonica B*, 50(3):405, 2019.

[120] D. Hove, E. Garrido, P. Sarriguren, D. V. Fedorov, H. O. U. Fynbo, A. S. Jensen, and N. T. Zinner. Emergence of clusters: Halos, Efimov states, and experimental signals. *Physical Review Letters*, 120:052502, 2018.

[121] L. V. Grigorenko, T. A. Golubkova, and M. V. Zhukov. Thomas-Ehrman effect in a three-body model: The ^{16}Ne case. *Physical Review C*, 91:024325, 2015.

[122] J. Tian, N. Wang, C. Li, and J. Li. Improved Kelson-Garvey mass relations for proton-rich nuclei. *Physical Review C*, 87:014313, 2013.

[123] H. T. Fortune. Mirror energy differences of $2s_{1/2}$, $1d_{5/2}$, and $1f_{7/2}$ states. *Physical Review C*, 97:034301, 2018.

[124] H. Nishibata, T. Shimoda, A. Odahara, S. Morimoto, S. Kanaya, A. Yagi, H. Kanaoka, M. R. Pearson, C. D. P. Levy, and M. Kimura. Shape coexistence in the $N = 19$ neutron-rich nucleus ^{31}Mg explored by β-γ spectroscopy of spin-polarized ^{31}Na. *Physics Letters B*, 767:81 – 85, 2017.

[125] P. Baumann, Ph. Dessagne, A. Huck, G. Klotz, A. Knipper, Ch. Miehé, M. Ramdane, G. Walter, G. Marguier, H. Gabelmann, C. Richard-Serre, K. Schlösser, and A. Poves. Beta decay of ^{30}Na: Experiment and theory. *Physical Review C*, 39:626 – 635, 1989.

[126] V. Z. Goldberg, B. T. Roeder, G. V. Rogachev, G. G. Chubarian, E. D. Johnson, C. Fu, A. A. Alharbi, M. L. Avila, A. Banu, M. McCleskey, J. P. Mitchell, E. Simmons, G. Tabacaru, L. Trache, and R. E. Tribble. First observation of ^{14}F. *Physics Letters B*, 692(5):307 – 311, 2010.

[127] K. W. Brown, R. J. Charity, J. M. Elson, W. Reviol, L. G. Sobotka, W. W. Buhro, Z. Chajecki, W. G. Lynch, J. Manfredi, R. Shane, R. H. Showalter, M. B.

Tsang, D. Weisshaar, J. R. Winkelbauer, S. Bedoor, and A. H. Wuosmaa. Proton-decaying states in light nuclei and the first observation of ^{17}Na. *Physical Review C*, 95:044326, 2017.

[128] R3BRoot - simulation and analysis tool. *https://www.r3broot.gsi.de/*.

[129] C. Scheidenberger, S. Gales, H. Geissel, H. Simon, I. Tanihata, and M. Winkler for the Super-FRS Collaboration. Unique separator-spectrometer experiments at the frontiers of nuclear physics: the Super-FRS scientific program. *EPJ Web of Conferences*, 66:11034, 2014.

[130] Technical Design Report on the Super-FRS.

[131] H. Geissel, J. S. Winfield, G. P. A. Berg, B. Franczak, N. Iwasa, G. Münzenberg, C. Nociforo, W. R. Plass, C. Scheidenberger, H. Weick, M. Winkler, and M. Yavor. Dispersion-matched spectrometer in the low-energy branch of the Super-FRS for high-resolution measurements with large-emittance relativistic fragment beams. *Nuclear Instruments and Methods in Physics Research B*, 317:277 – 283, 2013.

[132] H. Suzuki, L. Sinclair, P.-A. Söderström, G. Lorusso, P. Davies, L. S. Ferreira, E. Maglione, R. Wadsworth, J. Wu, Z. Y. Xu, S. Nishimura, P. Doornenbal, D. S. Ahn, F. Browne, N. Fukuda, N. Inabe, T. Kubo, D. Lubos, Z. Patel, S. Rice, Y. Shimizu, H. Takeda, H. Baba, A. Estrade, Y. Fang, J. Henderson, T. Isobe, D. Jenkins, S. Kubono, Z. Li, I. Nishizuka, H. Sakurai, P. Schury, T. Sumikama, H. Watanabe, and V. Werner. Discovery of ^{72}Rb: A nuclear sandbank beyond the proton drip line. *Physical Review Letters*, 119:192503, 2017.

[133] Flerov Laboratory of Nuclear Reactions of Joint Institute for Nuclear Research. *http://flerovlab.jinr.ru/flnr/index.html*.

[134] Saint-Gobain scintillating fiber. *https://www.crystals.saint-gobain.com/products/scintillating-fiber*.

[135] Hamamatsu multianode photomltiplier tube. *https://www.hamamatsu.com/resources/pdf/etd/H9500_H9500-03_TPMH1309E.pdf*.

[136] PETsys Electronics. *http://www.petsyselectronics.com/web/*.

[137] S. Ritt. DRS4 Evaluation Board Users Manual. *https://www.psi.ch/sites/default/files/import/drs/DocumentationEN/manual_rev50.pdf*, 2016.

[138] ExpertRoot framework for simulation of the detectors responce, event reconstruction and analysis in the EXPERT project at Super-FRS at FAIR and ACCULINNA-2 fragment-separator in JINR. *http://er.jinr.ru*.

[139] I. Muzalevsky, V. Chudoba, S. Belogurov, O. Kiselev, A. Bezbakh, A. Fomichev, S. Krupko, R. Slepnev, D. Kostyleva, A. Gorshkov, and E. Ovcharenko. NeuRad detector prototype pulse shape study. *EPJ Web of Conferences*, 177:03003, 2018.

[140] W. R. Leo. Techniques for Nuclear and Particle Physics Experiments. *Springer-Verlag Berlin Heidelberg*, 1987.

[141] L. Heilbronn, Y. Iwata, and H. Iwase. Off-line correction for excessive Constant-Fraction-Dsiscriminator walk in neutron Time-of-Flight experiments. *Nuclear Instruments and Methods in Physics Research A*, 522:495 – 503, 2004.

[142] D. Kostyleva, A. A. Bezbakh, V. Chudoba, A. S. Fomichev, A. V. Gorshkov, O. Kiselev, S. A. Krupko, I. Mukha, I. A. Muzalevskii, and C. Scheidenberger for the Super-FRS Experiment collaboration. Tracking cosmic radiation by the NeuRad neutron detector prototype with multi-channel readout electronics. *GSI-FAIR Scientific Report 2017*, page 125, 2018.

[143] TOFPET2: a high-performance ASIC for time and amplitude measurements of SiPM signals in time-of-flight applications. *https://www.petsyselectronics.com/web/website/docs/products/product1/TOFPET2_Overview.pdf*.

[144] O. Kiselev, A. Bezbakh, N. Egorov, I. Eremin, V. Eremin, N. Fadeeva, A. Fomichev, M. Golovkov, S. Golubkov, A. Gorshkov, A. Knyazev, C. Konkov, D. Kostyleva, S. Krupko, D. Mitina, I. Mukha, C. Nociforo, A. Prochazka, F. Schirru, R. Slepnev, A. Shepelev, Y. Tuboltsev, and E. Verbitskaya. Radiation hardness tests of Si detectors for Time of Flight measurements at the Super-FRS. *GSI Scientific Report 2014*, pages 137 – 139, 2015.

[145] D. Kostyleva, O. Kiselev, A. Bezbakh, V. Chudoba, V. Eremin, A. Fomichev, A. Gorshkov, S. Krupko, I. Mukha, I. Muzalevskii, C. Scheidenberger, and P. Sharov. Study of the silicon detectors for Time-of-Flight measurements at the Super-FRS facility and EXPERT experiments at FAIR. *Acta Physica Polonica B*, 49(3):503, 2018.

[146] M. Ciobanu, N. Herrmann, K. D. Hildenbrand, M. Kiš, A. Schüttauf, H. Flemming, H. Deppe, S. Löchner, J. Frühauf, I. Deppner, P. A. Loizeau, and M. Träger. PADI, an Ultrafast Preamplifier - Discriminator ASIC for Time-of-Flight Measurements. *IEEE Transactions on Nuclear Science*, 61:1015, 2014.

[147] E. Bayer and M. Traxler. A High-Resolution (< 10 ps RMS) 48-Channel Time-to-Digital Converter (TDC) Implemented in a Field Programmable Gate Array (FPGA). *IEEE Transactions on Nuclear Science*, 54:1547, 2011.

[148] V. Eremin, A. Bezbakh, I. Eremin, N. Egorov, A. Fomichev, M. Golovkov, A. Gorshkov, A. Galkin, O. Kiselev, A. Knyazev, D. Kostyleva, S. Krupko, D. Mitina, R. Slepnev, P. Sharov, and E. Verbitskaya. Beam tests of full-size prototypes of silicon detectors for TOF heavy-ions diagnostics in Super-FRS. *Journal of Instrumentation*, 12, 2017.

[149] R. Pfaff, D. J. Morrissey, W. Benenson, M. Fauerbach, M. Hellström, C. F. Powell, B. M. Sherrill, M. Steiner, and J. A. Winger. Fragmentation of ^{78}Kr projectiles. *Physical Review C*, 53:1753 – 1758, 1996.

[150] M. Del Santo, Z. Meisel, D. Bazin, A. Becerril, B. A. Brown, H. Crawford, R. Cyburt, S. George, G. F. Grinyer, G. Lorusso, P. F. Mantica, F. Montes, J. Pereira, H. Schatz, K. Smith, and M. Wiescher. β-delayed proton emission of ^{69}Kr and the ^{68}Se *rp*-process waiting point. *Physics Letters B*, 738:453 – 456, 2014.

[151] A. M. Rogers, M. A. Famiano, W. G. Lynch, M. S. Wallace, F. Amorini, D. Bazin, R. J. Charity, F. Delaunay, R. T. de Souza, J. Elson, A. Gade, D. Galaviz, M.-J. van Goethem, S. Hudan, J. Lee, S. Lobastov, S. Lukyanov, M. Matoš, M. Mocko, H. Schatz, D. Shapira, L. G. Sobotka, M. B. Tsang, and G. Verde. Ground-state proton decay of ^{69}Br and implications for the ^{68}Se astrophysical rapid proton-capture process waiting point. *Physical Review Letters*, 106:252503, 2011.

[152] W. R. Plass, Timo Dickel, I. Mardor, S. Pietri, H. Geissel, C. Scheidenberger, D. Amanbayev, S. Ayet San Andrés, J. Äystö, D. L. Balabanski, S. Beck, J. Bergmann, V. Charviakova, P. Constantin, T. Eronen, T. Grahn, F. Greiner, E. Haettner, C. Hornung, J.-P. Hucka, A. Jokinen, A. Kankainen, I. Miskun, I. D. Moore, A. Pikthtelev, I. Pohjalainen, S. Purushothman, Z. Patyk, M. P. Reiter, A.-K. Rink, S. Rinta-Antila, A. Spataru, H. Weick, J. S. Winfield, and M. I. Yavor for the Super-FRS Experiment Collaboration. The science case of the FRS Ion Catcher for FAIR Phase-0. *Hyperfine Interactions*, 240:73, 2019.

[153] T. Kubo, K. Kusaka, K. Yoshida, A. Yoshida, T. Ohnishi, M. Ohtake, Y. Yanagisawa, N. Fukuda, T. Haseyama, Y. Yano, N. Kakutani, T. Tsuchihashi, and K. Sato. Status and overview of superconducting radioactive isotope beam separator BigRIPS at RIKEN. *IEEE Transactions on Applied Superconductivity*, 17(2):1069 – 1077, 2006.

[154] B. Pritychenko, E. Beták, M.A. Kellett, B. Singh, and J. Totans. The Nuclear Science References (NSR) database and web retrieval system. *Nuclear Instruments and Methods in Physics Research Section A: Accelerators, Spectrometers, Detectors and Associated Equipment*, 640(1):213 – 218, 2011.

[155] T. Kubo, D. Kameda, H. Suzuki, N. Fukuda, H. Takeda, Y. Yanagisawa, M. Ohtake, K. Kusaka, K. Yoshida, N. Inabe, T. Ohnishi, A. Yoshida, K. Tanaka, and Y. Mizoi. BigRIPS separator and ZeroDegree spectrometer at RIKEN RI Beam Factory. *Progress of Theoretical and Experimental Physics*, 2012(1):03C003, 2012.

[156] G. Saxena, M. Kumawat, M. Kaushik, S.K. Jain, and Mamta Aggarwal. Bubble structure in magic nuclei. *Physics Letters B*, 788:1 – 6, 2019.

[157] G. Saxena, M. Kumawat, B.K. Agrawal, and Mamta Aggarwal. Anti-bubble effect of temperature and deformation: A systematic study for nuclei across all mass regions between A=20–300. *Physics Letters B*, 789:323 – 328, 2019.

[158] L. V. Grigorenko, E. V. Litvinova, and M. V. Zhukov. Recent advances in theoretical studies of $2p$ radioactivity: Nuclear many-body structure in three-body model. *Acta Physica Polonica B*, 42:555 – 558, 2011.

[159] A. S. Fomichev, I. G. Mukha, S. V. Stepantsov, L. V. Grigorenko, E. V. Litvinova, V. Chudoba, I. A. Egorova, M. S. Golovkov, A. V. Gorshkov, V. A. Gorshkov, G. Kaminski, S. A. Krupko, Yu. L. Parfenova, S. I. Sidorchuk, R. S. Slepnev, G. M. Ter-Akopian, R. Wolski, and M. V. Zhukov. Lifetime of ^{26}S and a limit for its $2p$ decay energy. *International Journal of Modern Physics E*, 20(06):1491 – 1508, 2011.

[160] G. Saxena, M. Kumawat, M. Kaushik, S.K. Jain, and Mamta Aggarwal. Two-proton radioactivity with $2p$ halo in light mass nuclei A = 18 – 34. *Physics Letters B*, 775:126 – 129, 2017.

[161] A. A. Bezbakh, V. Chudoba, S. A. Krupko, S. G. Belogurov, D. Biare, A. S. Fomichev, E. M. Gazeeva, A. V. Gorshkov, L. V. Grigorenko, G. Kaminski, O. A. Kiselev, D. A. Kostyleva, M. Yu. Kozlov, B. Mauyey, I. Mukha, I. A. Muzalevskii, E. Yu. Nikolskii, Yu. L. Parfenova, W. Piatek, A. M. Quynh, V. N. Schetinin, A. Serikov, S. I. Sidorchuk, P. G. Sharov, R. S. Slepnev, S. V. Stepantsov, A. Swiercz, P. Szymkiewicz, G. M. Ter-Akopian, R. Wolski, B. Zalewski, and M. V. Zhukov. Evidence for the first excited state of ^{7}H. *Physical Review Letters*, 124:022502, 2020.

[162] M. Mager. ALPIDE, the monolithic active pixel sensor for the ALICE ITS upgrade. *Nuclear Instruments and Methods in Physics Research Section A: Accelerators, Spectrometers, Detectors and Associated Equipment*, 824:434 – 438, 2016.

[163] Struck Innovative Systeme. SIS3305 5 gs/s, 2.5 gs/s, 1.25 gs/s 10-bit VME Digitizer. *https://www.struck.de/sis3305-M-0x1C0B_0x2C0B-1-v100-userdesign.pdf*.

[164] A. Jokinen, M. Oinonen, J. Äystö, P. Baumann, F. Didierjean, P. Hoff, A. Huck, A. Knipper, G. Marguier, Yu. N. Novikov, A. V. Popov, M. Ramdhane, D. M. Seliverstov, P. Van Duppen, G. Walter, and the ISOLDE-Collaboration. Proton instability of ^{73}Rb. *Zeitschrift für Physik A Hadrons and Nuclei*, 355:227 – 230, 1996.

[165] B. Blank, S. Czajkowski, F. Davi, R. Del Moral, J. P. Dufour, A. Fleury, C. Marchand, M. S. Pravikoff, J. Benlliure, F. Boué, R. Collatz, A. Heinz, M. Hellström, Z. Hu, E. Roeckl, M. Shibata, K. Sümmerer, Z. Janas, M. Karny, M. Pfützner, and M. Lewitowicz. First observation of the $t_z = -7/2$ nuclei ^{45}Fe and ^{49}Ni. *Physical Review Letters*, 77:2893 – 2896, 1996.

[166] V. Borrel, R. Anne, D. Bazin, C. Borcea, G. G. Chubarian, R. Del Moral, C. Detraz, S. Dogny, J. P. Dufour, L. Faux, A. Fleury, L. K. Fifield, D. Guillemaud-Mueller, F. Hubert, E. Kashy, M. Lewitowicz, C. Marchand, A. C. Mueller, F. Pougheon, M. S. Pravikoff, M. G. Saint-Laurent, and O. Sorlin. The decay modes of proton drip-line nuclei with A between 42 and 47. *Zeitschrift für Physik A - Hadrons and Nuclei*, A344:135, 1992.

Acknowledgements

In this short letter, I would like to thank everyone who introduced me to experimental nuclear physics and is leading me through my studies and research. I wish to thank those who made this work possible, inspired me in the most difficult days, who taught me to work independently and be brave to start exploring new things.

First of all, I would like to express my deepest gratitude to my doctor father Prof. Dr. Christoph Scheidenberger and my advisor Prof. Dr. Dr. h.c. Hans Geissel for recognizing my potential and for giving me an opportunity to work on the exciting scientific topic. I am deeply grateful for their supervision throughout my studies and help shaping my research into a scientific dissertation.

I am very thankful to my supervisor Dr. Ivan Mukha for the knowledge he passed me, the patience, and the endless time he invested in my education. I greatly appreciate his help and support, valuable scientific and personal advices, and a friendly terms between us.

I would also like to say a very big thank you to Dr. Oleg Kiselev for the knowledge in the field of detector technologies I gained, for the supervision of my work in the laboratory, and for involving me in different exciting scientific projects. It was under his supervision that I began my scientific work at the GSI as a summer student and became engaged in the research carried out by the institute.

I would like to express my gratitude to our theory guru, Prof. Dr. Leonid Grigorenko, for inspiring me with his passion for science, the supervision of my studies in Dubna, and the constant support of my experimental research here, at GSI. Furthermore, I am most thankful to the Dubna colleagues for the opportunity to work and perform experiments together. I would like to give special thanks to Dr. Andrey Fomichev, Prof. Dr. Mikhail Golovkov, Pavel Sharov, Irina Egorova, Ivan Muzalevskii and Dr. Vratislav Chudoba.

It is a big pleasure to thank here the scientific groups of the FRS and the Super-FRS for accepting me into the team, teaching me how to work on the fragment separator, and for the fruitful working atmosphere. Special thanks I would like to give to Dr. Helmut Weick, Dr. Emma Haettner, Dr. Yoshiki Tanaka, Dr. Stephane Pietri, and my office mates Dr. Christine Hornung, Dr. Andrej Prochazka, Sönke Beck, Dr. Soumya Bagchi, and Jan-Paul Hucka. I wish also to express my gratitude to the university group IONAS for their contributions to my scientific life, interesting seminars, and fruitful discussions. I would like to especially mention my dear colleagues and friends Dr. Sivaji Purushothaman, Dr. Ivan Miskun and Daler Amanbayev, and thank them for the support and numerous valuable advice concerning work and personal matters.

I would like to give here a huge thank you to my friends from GSI, especially to Dr. Premaditya Chhetri and Brankica Andelic for the encouragement during my studies and all the fun times we share. I would also like to thank my colleague and friend Dr. Hans Törnqvist for the vast amount of times he helped me at work with DAQ and for

all the nice off-work discussions.

Furthermore, I want to thank all of my friends from Dubna for staying by my side regardless of the distance between us. A big spasibo is for my friend Ksenia who has been sending me positive vibes all the way from Berlin. Very special thanks go to my home town to the two beloved friends of mine, dearest Katya and Lena.

Finally, I most grateful to my mother Irina and grandmother Evgeniya for all their endless love, tireless care and strong support. I would never manage to become what I am without their wise guidance. And I would like to finish this letter with a great thank you to my wonderful husband Max, who encouraged my ambition to continue a scientific career, enormously helped me throughout the work on the thesis, and whose support keeps me going. Thank you!

Selbstständigkeitserklärung

Ich erkläre: Ich habe die vorgelegte Dissertation selbständig und ohne unerlaubte fremde Hilfe und nur mit den Hilfen angefertigt, die ich in der Dissertation angegeben habe. Alle Textstellen, die wörtlich oder sinngemäß aus veröffentlichten Schriften entnommen sind, und alle Angaben, die auf mündlichen Auskünften beruhen, sind als solche kenntlich gemacht. Ich stimme einer evtl. Überprüfung meiner Dissertation durch eine Antiplagiat-Software zu. Bei den von mir durchgeführten und in der Dissertation erwähnten Untersuchungen habe ich die Grundsätze guter wissenschaftlicher Praxis, wie sie in der „Satzung der Justus-Liebig-Universität Gießen zur Sicherung guter wissenschaftlicher Praxis“ niedergelegt sind, eingehalten.

Datum	Daria Kostyleva